UNIVERSITY OF PADOVA

PADOVA NEUROSCIENCE CENTER

Ph.D. School in Neuroscience - Cycle: XXXIV

From microstructure imaging to structural connectivity: the use of diffusion mri to investigate the impact of gliomas on the human brain

---

Candidate:

Umberto Villani

Headmaster of the school:

Prof. Antonino Vallesi

Supervisor:

Prof. Alessandra Bertoldo

Cosupervisor:

Prof. Michel Thiebaut De Schotten

A Mamma, Papà e Francesco

A chi, su questa terra e non, veglia su di me, ed è esperto nel delicato gioco della mia bilancia personale

Contents

Abstract

Diffusion-based Magnetic Resonance Imaging (dMRI) is rapidly becoming the instrument of choice to probe the structure of the human brain in vivo. By modelling the properties of water diffusion inside cerebral tissues, it is indeed possible to extract surrogates of histological measures, such as fibre density, conformation and preferential direction, in a non-invasive manner. Furthermore, local orientational features can be used to reconstruct axonal pathways that link different brain regions, allowing the study of how they are structurally connected. Nevertheless, the quantification of dMRI measures must be cautious when the physiological environment of brain tissues is drastically altered. Such is the case of brain tumours. The microstructure of brain tumours is highly heterogeneous, being diverse between and inside specific types and malignancy grade. The wide spectrum of cellular environments they feature invalidates several hypotheses on which diffusion-based microstructure models are built and, contemporarily, poses difficulties in the process of tracking white matter in affected regions. Given these limitations, are these techniques worth using in this complex pathological environment? During the last three years I explored several state of the art diffusion-based methodologies in a cohort of patients suffering from a range of brain tumours. Hence, this thesis strives to be a summary of this work, laying the foundation for future studies aiming to integrate the use of advanced dMRI in the clinical neuro-oncological practice. The thesis is divided in three main parts, which are organized as follows:

In the first part, an assessment is made whether two widely known diffusion advanced models, Neurite Orientation Dispersion and Density Imaging (NODDI) and the Spherical Mean Technique (SMT) are properly fitted in the tumoral lesion in terms of goodness-of-fit and parameter precision. Several works, concentrating mainly on NODDI, used such techniques not as biophysical models but as signal representations, trying to find biomarkers that differentiate more and less isotropic environments which contribute to the totality of the diffusion signal in 'tumoral' voxels. These studies were performed without first checking whether

1

these diffusion metrics are mathematically reliable. This issue is here assessed from a technical point of view, without giving specific biophysical meaning to the models in exam inside the tumoral tissues

The second part features a comparison study between methods for the identification of structurally disconnected white matter (WM) in brain tumour patients. Here, two branches of methodologies were identified, namely direct and indirect approaches. The former branch use single-subject tractography to directly investigate which fibre bundles may be affected by the presence of the tumour. The latter branch, instead, embed the focal lesion on a normative atlas of white matter tracts, identifying the probability of a WM voxel being disconnected by the pathology. Employing known image analysis metrics, both approaches are discussed, highlighting points of convergence, but also of disagreement, in terms of the physio-pathological information they can convey.

In the third and last part of this thesis, tumour-related anomalies of diffusion-based structural connectivity (SC) matrices are put in relationship with metabolic measures from [18F]-FDG PET. A procedure for tractography algorithm selection was firstly performed, and after the SC quantification, a statistical method of detecting altered connections in the tumour-affected SC matrix is presented. Within such a framework, the amount of affected SC entries was eventually quantified in the available cohort of patients and put in relationship with standardized uptake values from PET. Finally, a discussion of the results of this association is provided, paying particular attention to the limitations of these imaging modalities in the brain oncological field.

Sommario

La Risonanza magnetica di diffusione (dMRI) sta diventando lo strumento più adatto per indagare la microstruttura del cervello umano in vivo. Modellando le proprietà della diffusione dell'acqua nei tessuti cerebrali, è infatti possibile ottenere delle misure simili a quelle derivate dall'istologia, come la densità di fibre, la loro conformazione e la loro direzione di propagazione, in maniera non invasiva. In più, misure locali di integrità e di orientazione della materia bianca possono essere usate da algoritmi di trattografia per ricostruire globalmente il percorso seguito dalle fibre in tutto il cervello, permettendo di studiare come le varie regioni corticali sono connesse. Nonostante ciò, l'utilizzo della dMRI deve essere condotto con attenzione in presenza di patologie che alterano drasticamente la fisiologia del cervello, come nel caso dei tumori cerebrali. La varietà di microambienti cellulari che caratterizza questo tipo di patologie invalida alcune ipotesi sul quale si fondano i modelli di microstruttura basati sulla dMRI. In più, il processo di ricostruzione della trattografia nel cervello presenta particolari difficoltà tecniche nelle regioni affette dalla patologia. Date queste limitazioni, vi è del valore nell'utilizzare tecniche basate sulla dMRI in questo complesso ambiente patologico? Negli ultimi tre anni, ho avuto modo di esplorare diverse di queste metodologie in una popolazione di pazienti con tumore cerebrale. La presente tesi vorrebbe quindi essere una sintesi di questo lavoro, che costituisce una base verso l'integrazione di tecniche di diffusione avanzate all'interno della pratica neuro-oncologica. Nella sua interità, la tesi presenta tre lavori, organizzati come segue:

La prima parte presenta uno studio analitico su due noti modelli di microstruttura, Neurite Orientation Dispersion and Density Imaging (NODDI) e la Spherical Mean Technique. Questo lavoro è volto alla quantificazione della bontà del fit e precisione parametrica delle due tecniche all'interno della lesione tumorale. Alcuni lavori, concentrati principalmente su NODDI, usano queste tecniche come modelli di segnale e non biofisici, cercando di trovare biomarker capaci di caratterizzare aspecificamente il tessuto patologico. L'analisi qui svolta supporta i

risultati di letteratura da un punto di vista tecnico, senza considerazioni sul significato biologico di questi modelli.

La seconda parte contiene uno studio di confronto tra due diversi metodi per la quantificazione di regioni di materia bianca sconnessa a causa del tumore. Due categorie di approcci qui sono stati studiati: approcci diretti, e approcci indiretti. I primi fanno uso della trattografia singolo-soggetto per investigare quali fasci di fibre siano affetti nel loro decorso dalla presenza del tumore. I secondi invece non hanno bisogno di acquisizioni dMRI, e utilizzano un atlante normativo di fasci di materia bianca per investigare, probabilisticamente, quali di questi potrebbero essere affetti data la locazione e l'estensione della zona tumorale. Utilizzando noti strumenti di analisi dell'immagine, i due approcci vengono qui confrontati, discutendo pregi e difetti di ciascun metodo.

Nella terza e ultima parte della tesi, viene studiata la relazione tra alterazioni di matrici di connettività strutturale (SC) di pazienti tumorali e variazioni regionali di metabolismo misurate usando la Tomografia ad Emissione di Positroni (PET) con tracciante [18F]-FDG. All'interno di questo studio, viene prima proposta una procedura per la selezione dell'algoritmo di trattografia ottimale per le analisi. A seguire, viene sviluppata una metodologia statistica per rilevare le loro connessioni della matrice SC alterate dalla presenza del tumore. La presenza di queste alterazioni viene infine correlata con la PET, e si discutono i risultati ottenuti, ponendo particolare attenzione alle limitazioni di entrambe queste modalità di imaging.

List of Figures

List of Tables

List of acronyms

Abbreviation	Full expression
ACT	Anatomicallly constrained tractography
ADC	Apparend diffusion coefficient
AMICO	Accelerated microstructure imaging via convex optimization
ANTs	Advanced normalization tools
CRLB	Cramer-Rao lower bound
CSD	Constrained spherical deconvolution
CSF	Cerebrospinal fluid
DEC	Direction encoded color
DKI	Diffusion kurtosis imaging
dMRI	Diffusion magnetic resonance imaging
dStrD	Direct structural disconnection
DTI	Diffusion tensor imaging
DWI	Diffusion weighted imaging
EC	External capsule
Emc	Extreme capsule
EPI	Echo-planar imaging
FA	Fractional anisotropy
FOD	Fiber orientation distribution
FSL	FMRIB software library
gbm	Glioblastoma
GM	Grey matter
GSFs	Generalized sensitivity functions
iStrD	Indirect Structural Disconnection
MAD	Mean absolute deviation
MRI	Magnetic resonance imaging
MRI	Magnetic resonance
NMR	Nuclear magnetic resonance

NODDI	Neurite orientation dispersion and density imaging
ODF	Orientation distribution function
PCA	Principal component analysis
PGSE	Pulsed gradient spin echo
QA	Quality assurance
RF	Radiofrequency
RSS	Residual sum of squares
SD	Spherical deconvolution
SIFT	Spherical deconvolution informed filtering of tractograms
SMT	Spherical mean technique
SNR	Signal to noise ratio
SP	Striato parietal
StrD	Structural disconnection
SUVR	Standardized uptake value ratio
WM	White matter

Chapter 1

Introduction

Globally, 250000 new cases of brain tumours are diagnosed every year (Ferlay et al., 2015). Among them, gliomas are the most prevalent and aggressive subtypes, infiltrating and disrupting the normal appearing parenchyma, and causing significant morbidity and mortality (Chen et al., 2017; Ostrom et al., 2014). Gliomas frequently develop from glial cells and, according to the World Health Organization (WHO), they are classified into different histological grades that reflect their malignancy and aggressiveness (Louis, Perry, Reifenberger, et al., 2016; Louis, Perry, Wesseling, et al., 2021). High-grade gliomas (HGG; grades III and IV) are considered malignant tumours and are treated more aggressively than low-grade gliomas (LGG; grades I and II).

Imaging plays a a pivotal role in assisting patients affected by brain tumours, providing useful information for surgical planning, diagnosis and follow-up. While Computed Tomography (CT) scans initially were the preferred diagnostic tool due to their ease of access, they were readily substituted by Magnetic Resonance Imaging (MRI) as its value became evident throughout the years. Clinical MRI protocols for brain tumours include several morphological images: T2-weighted (T2w) and fluid-attenuated inversion recovery (FLAIR) imaging provide clear outline of the tumoral lesion and oedema, while the gadolinium enhanced T1-weighted contrast is directly linked to blood-brain-barrier disruption (Dhermain et al., 2010). While these magnetic resonance (MR) sequences are the basis for the diagnosis of primary brain tumours, the detailed characterization of their structure along its clinical course is extremely challenging to be done by morphological imaging alone. Diffusion Magnetic Resonance imaging (dMRI) is a neuroimaging technique which allows to probe the human brain tissues by analyzing the diffusive motion of water molecules (Jacques-Donald Tournier et al., 2011). Given that the process of molecular diffusion is highly sensitive to the structural fea-

tures of the environment it occurs in, dMRI has a unique connection to biological features such as cell sizes, shapes, permeability and spatial arrangement. From its conception as a tool to measure the apparent diffusion coefficient (ADC) of water throughout the brain (Le Bihan, Eric Breton, et al., 1986), research into dMRI methodologies brought forward many hardware- and software-related improvement, giving birth to two broad categories of techniques: Microstructure models (Alexander et al., 2019; Dmitry S Novikov, Els Fieremans, et al., 2019) and Tractography (Mori, Crain, et al., 1999; Basser, Pajevic, et al., 2000; Jeurissen, Descoteaux, et al., 2019). While extensively used to investigate the healthy human brain, both these analysis approaches struggle to find consistent application in the clinical practice for brain tumours, due to a series of causes. Established microstructure models from the literature are usually targeted to healthy white matter (H. Zhang et al., 2012; Fieremans et al., 2013; Kaden, Kelm, et al., 2016), but in the tumoral area their parameter estimates lose their specific meaning. New formulations targeted at the tumour require extensive validation before their possible clinical translation (Nilsson et al., 2018). Furthermore they require specific acquisition protocols which are not commonly distributed through MR vendors, rendering their implementation non-trivial (Szczepankiewicz, Lasič, et al., 2015; T. A. Roberts et al., 2020). On the other side, tractography algorithms face the issue of false positive/false negative connections (Maier-Hein et al., 2017; Aydogan et al., 2018) and present overall difficulties in tracking through oedema and the tumoral region (F.-C. Yeh et al., 2021).

1.1 Aims

Employing microstructure models to extract meaningful information from tumoral tissue and characterizing the impact of the mass lesion on the axonal fibers in the whole brain offer two separate but complementary ways with which dMRI research can significantly contribute to advance the current state of glioma (and brain tumours in general) diagnosis, presurgical planning and monitoring. Paying careful attention to the limitations of the related state of the art techniques, the work featured in this thesis spans across both these branches of research. More specifically, the objectives of the thesis were the following

- The assessment of the mathematical reliability of parameter estimates from selected white matter microstructure models inside the tumoral lesion, without looking at their biophysical meaning.

- Quantifying patterns of white matter damage due to the presence of the tumour through the use of tractography algorithms, both at the *voxel level* and at the *connectome level*.

1.2   Outline of the thesis

The structure of the thesis is organized as follows:

- Chapter Two will give a basic introduction to the theoretical and practical concepts of dMRI. Advanced concepts of microstructure imaging and tractography will be briefly presented in order to better understand the context of the studies of the subsequent chapters.

- Chapter Three contains an analytical study of goodness of fit and parameter estimation precision inside the tumoral lesion for three advanced diffusion techniques: Neurite Orientation Dispersion and Density Imaging (NODDI), the Spherical Mean Technique (SMT), and the Diffusion Kurtosis Imaging (DKI).

- Chapter Four is a comparison study between two different approaches to quantifying patterns of white matter disconnections due to the presence of a tumour. A quantitative framework to evaluate their similarity is here proposed, and benefits and criticalities of both techniques are extensively discussed here.

- Chapter Five details a statistical procedure to define subject-specific alterations of the structural connectome based on the evaluation of structural connectivity matrices. Before the computation of said matrices, a thorough tractography algorithm selection is carried out, based on the physiological plausibility of the derived tractogram and its sensitivity to streamline cut-off criteria. Eventually, findings concerning subject-specific structural alterations are correlated with regional [18F]-FDG PET measures, establishing a link between the metabolism of normal appearing cortical regions and the state of their white matter connections.

- Chapter Six marks the conclusion of this thesis, recapping the results of the work and expressing some brief thoughts regarding their significance and contextualization in the current literature.

Chapter 2

Basics of diffusion MRI

2.1 The diffusion process

As the name implies, diffusion Magnetic Resonance Imaging revolves around acquiring magnetic resonance imaging signals which are in some manner impacted by the physical process of the diffusion of water molecules in the brain. Before describing this particular biophysical process, it important to note that it is not the only kind of movement water molecules undergo in physical bodies during an MRI scan. It is therefore beneficial to introduce the three separate motions to make a clear separation between these different contexts:

1. We define *bulk motion* as the motion which occurs when water molecules move for more for a distance which exceedes the dimensions of a voxels. Bulk motion usually happens due to subject movements during the scan, causing single MR images to feature blurring and ghosting, and to be misaligned between each other.

2. We define *flow* as the coherent water motion happening inside a single voxel of the MR images. This movement occurs due to perfusion in blood arteries, vessels and capillaries. In practice, flow can be multidirectional when in presence of convoluted capillary structures.

3. The third process, the one we are interested in, is the biophysical process of *diffusion*. If we place a drop of ink in a system where diffusion is present, the center of the drop will remain approximately in the same position, but particles will start to randomly scatter among the available volume (provided no obstacle or barriers are present in the medium).
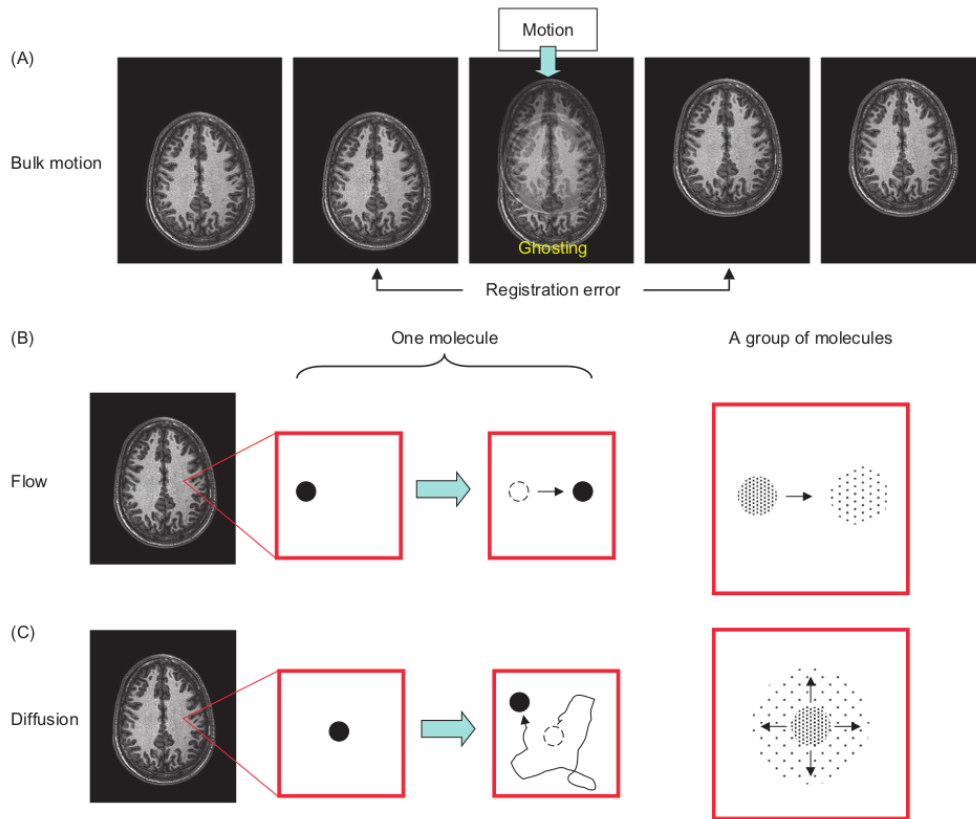
Figure 2.1: The three different types of water motion experienced by water molecules. (A) The effect of bulk motion on MR images. (B) Flow. Groups of molecules experience a displacement with similar intensity and directional features. (C) Diffusion. Water molecules scatter randomly and independently from each other, with no defined direction. Reproduced from (Mori and J-Donald Tournier, 2013).

Figure 2.1 provides a graphical overview of the three different processes. Having distinguished between them, the next few sections will solely be devoted to give a basic understanding of the process of diffusion

2.1.1 Statistical description of diffusion

Empirical evidence of diffusion (or Intra-Voxel Incoherent Motion, IVIM) dates back to 1828, when Robert Brown first described the incoherent motion of pollen grains suspended in water (Brown, 1828). Such motion was quantitatively described later by Adolf Fick, who theorized two mathematical laws to describe this process (Fick, 1855). The first one describes the phenomenon in stationary conditions, while the second does so in a time-variant system:

$$J = \frac{\partial}{\partial x}(D\rho) \tag{2.1}$$

$$\frac{\partial \rho}{\partial t} + \frac{\partial J}{\partial x} = 0 \tag{2.2}$$

where J is the net molecular flow, D is the diffusion coefficient, t is time, x is the position in space and ρ is the particle density. Assuming D is fixed, merging (2.1) and (2.2) yields:

$$\frac{\partial \rho}{\partial t} = D\frac{\partial^2 \rho}{\partial x^2} \tag{2.3}$$

The solution to (2.3) was proposed by Albert Einstein (Einstein, 1905), which has the following form:

$$\rho(x,t) = \frac{1}{\sqrt{4\pi Dt}}e^{-\frac{x^2}{4Dt}} \tag{2.4}$$

(2.4) reflects the fact that diffusion can be described as a gaussian process with zero mean and standard deviation (also called *diffusion length*), equal to:

$$\sigma = L(t) = \sqrt{2Dt} \tag{2.5}$$

(2.5) is of pivotal importance as it highlights that the statistical properties of the net displacement of particles are essentially dependent on the diffusion coefficient and the time t from which diffusion starts occurring. In absence of obstacles or barriers, the diffusion coefficient D is determined by the Stokes-Einstein equation:

$$\sigma = \mu k_b T \tag{2.6}$$

where μ is the mobility of spins, k_b is the-Stephan Boltzmann Constant and T is the temperature. (2.6) highlights how the temperature is an important parameter to account for in diffusion experiments, and needs to be accounted for when, for example, designing and comparing in-vivo and ex-vivo acquisitions. Why is the diffusion process of water molecules so relevant to us? The answer to this question lies in (2.5). In typical MRI experiments, the diffusion time is essentially controlled and fixed between the millisecond and second scales, depending on the specific acquisition sequence and performance of diffusion gradients. On the other hand, the diffusion coefficient, between 10° and body temperature, usually varies between 1 to 3 mm^2/ms. It follows that typical values for the diffusion length (again, the standard deviation of the gaussian process described above) are in the

range:

$$L(t) \sim 1 - 50 \mu m \tag{2.7}$$

Two brief but important considerations can be made at this point:

1. Modulating the diffusion time via experimental settings allows us to study a phenomenon occurring at scales which are far smaller that the nominal resolution of conventional MRI scanners

2. Furthermore, the diffusion lengths which we can study are similar to the dimensions of cells composing the tissues of the human body.

Thus, measuring and detecting anomalies in the diffusion process occurring in a particular region of the brain offers us a powerful tool to investigate the structural changes caused by potential physiological and pathological events.

2.2   Measuring diffusion with MRI

Given that analyzing the properties of diffusion offers us an invaluable chance to probe microstructural environments in the human brain, it is important to understand how this process can be related to the MRI signal. The possibility of measuring diffusion with Nuclear Magnetic Resonance (NMR) was long known before MRI was first proposed in early 1970s. The disruptive effect of brownian motion on NMR measurements was first described by Hahn in 1950 (Hahn, 1950). Shortly after, the basic formalism describing magnetic resonance, the Bloch Equations (Bloch, 1946) was extended by Torrey to account for the diffusion process (Torrey, 1956). Later in the years, Stejskall and Tanner proposed to add a pair of pulsed gradients in the basic spin echo sequence to enhance the sensitivity of the NMR signal to the diffusive motion of water molecules (Stejskal et al., 1965). This addition brought them to the the definition of the Pulsed-Gradient Spin-Echo (PGSE) scheme, which is the basis of a vast portion of the diffusion-weighted sequences used nowadays. The PGSE scheme is shown in Figure 2.2.

The two magnetic pulsed gradients featured in the PGSE sequence (denoted in purple in the figure) introduce dephasing in the precession of the nuclear spins of water molecules, causing the overall signal to be attenuated. The extent of this process is governed by the random motion of water molecules occuring between the application of the two pulsed gradients, following the formula (Emsell et al., 2016):
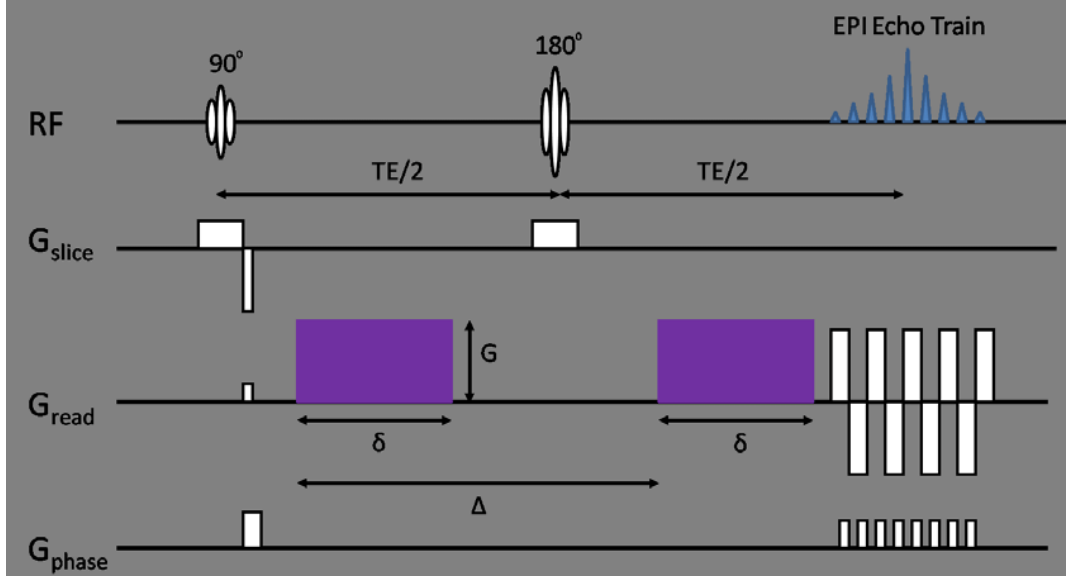
Figure 2.2: The scheme for the Stejskal-Tanner diffusion-weighted spin echo sequence with EPI readout. In purple are highlighted the pulsed gradients which allow the diffusion sensitization. Reproduced from (Avram, 2011). EPI = echoplanar imaging, RF = radiofrequency.

$$S = \int_x P(x, \Delta)\phi(x)\,dx = \int_x \frac{1}{\sqrt{4\pi D\Delta}} e^{-\frac{x^2}{4D\Delta}} e^{i\gamma G\delta x}\,dx \qquad (2.8)$$

where S is the total NMR signal, $P(x, \Delta)$ is the probability describing the diffusion process (see (2.4)), $\phi(x)$ is the dephasing caused by the diffusion pulsed gradients, γ is the gyromagnetic ratio and x is the net displacement spins undergo due to the diffusion process. G, Δ and δ are respectively the gradient strength, the diffusion time and the diffusion gradient pulse duration. The three of them characterize the diffusion gradients in the PGSE sequence.

(2.8) appears convoluted to understand at first. Thus a few considerations can be made to exemplify its understanding:

1. In cases where either $G = 0$ or/and $\delta = 0$, the second exponential term amounts to 1. Without dephasing, the signal subsequently becomes identical to 1, being the integral of a probability density function. Thus, in absence of the PGSE pulsed gradients, the signal remains theoretically unattenuated, *even* in presence of diffusion ($D > 0$).

2. In cases where both $G > 0$ and $\delta > 0$, but no diffusion is present ($D = 0$), the probability density function collapses to a Dirac's delta $\delta_0(x)$. Again, the integral is identically equal to 1. Thus, with active gradients and no

diffusion, we are in the case of no attenuation of the original signal ($S = 1$).

3. Whenever the gradients are active and the diffusion process is present in the system, nuclear spin populations will experience dephasing due to the action of the two pulsed gradients, resulting in a decrease of the NMR signal. ($S < 1$). The amount of dephasing introduced depends on the experimental settings G, Δ, δ (i.e. parameters for which values are known and can be set) and the diffusion coefficient D, which is an intrinsic property of the system.

(2.8) has a closed form solution, and after several passages of derivation, we obtain the well-known Stejskal-Tanner formula:

$$\frac{S}{S_0} = e^{-\gamma^2 G^2 \delta^2 (\Delta - \delta/3) D} \tag{2.9}$$

where S_0 is the signal acquired without diffusion gradient and identical echo time. In contemporary literature, it is customary to reorganize (2.9) in the following form:

$$\begin{cases} S = S_0 e^{-bD} \\ b = \gamma^2 G^2 \delta^2 (\Delta - \delta/3) \end{cases} \tag{2.10}$$

The term b is named b-value and has unit s/mm^2. (2.10) is a functional reorganization which clearly shows what was previously stated: we have a dependence on experimental settings (i.e. the b-value) and on a property of the system in exam (the diffusion coefficient). It is worth mentioning that (2.10) is valid under the hypothesis that D does not vary within each voxel. As it will be discussed further in this chapter, this assumption does not hold in practice, causing issues in the biological interpretation of the formula.

2.3 From the measurement to the quantification: DWI and DTI

The translation of the diffusion sequence from NMR to MRI begun with the pioneering work of Denis Le Bihan (Le Bihan and Breton, 1985; Le Bihan, Eric Breton, et al., 1986), who introduced the concept of diffusion-weighted images. Later in the years additional work combinining the PGSE scheme with 2D Echo-Planar Imaging (EPI) readout made the sequence feasible in clinical settings by
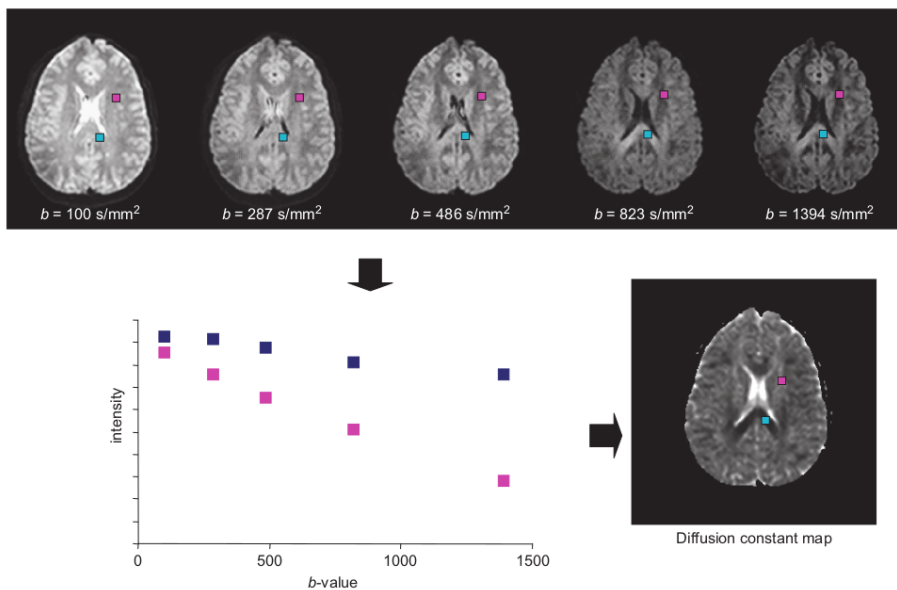
Figure 2.3: Schematic illustration of the computation of the diffusion coefficient map inside the brain. Having acquired a set of dMRI images, the diffusion signal can be used to quantify the voxel-wise ADC. Adapted from (Mori and J-Donald Tournier, 2013).

greatly reducing the time of acquisition and the presence of imaging artifacts (Schmitt et al., 2012; R. Turner et al., 1991). Acquiring diffusion MR images essentially translates to acquiring a multitude of diffusion-weighted signals, with precise and known spatial location. Looking back at the mono-exponential behaviour of (2.10), it is clear that it is possible to compute an approximation of the diffusion coefficient D for each location of the MR image defined by its voxels. The process of this computation, shown in Figure 2.3, can be explained as follows:

1. Several diffusion-weighted images of the brain are acquired. These image have significant differences in terms of contrast because the b-value was set differently for each one of them. It is common to say that these images have *different diffusion weightings*

2. From the entirety of these images, we extract the values relative to a specific position (see purple and blue dots in 2.3). It follows that we have a magnitude signal, whose independent variable is the b-value.

3. To each one of these signals, we can fit (2.10) using linear least squares (LLS) techniques to recover the diffusion coefficient term.
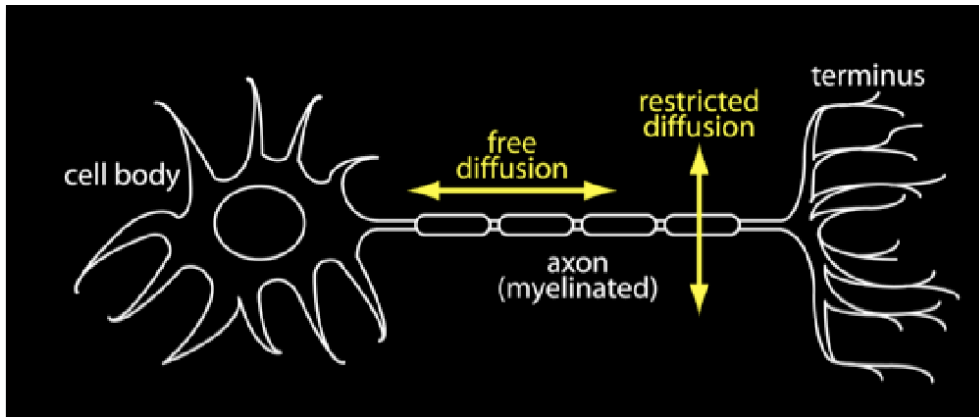
Figure 2.4: Peculiarities of the diffusive motion of water molecules in presence of axonal fibres. Particles are free to move in the direction parallel to axonal bodies, but present motion restriction due to their presence in the perpendicular direction.

4. Recovering all Ds from the voxels of the brain, we can finally reconstruct a parameter map which gives us a depiction of how the diffusion coefficient changes throughout the entirety of the brain.

This process is usually referred to as Diffusion-weighted Imaging (DWI). It is worth of note that the term D is also known as the *Apparent Diffusion Coefficient* (ADC) to highlight the fact that it is an averaged measure. A multitude of cellular environments, inside which diffusion may behave very differently, inhabit each voxel of the brain, and ADC is 'apparent' in the sense that it is an overall description of these behaviours across its volume. In its simplicity, DWI makes the strong assumption that the diffusive motion of water molecules is *isotropic*, which means that there is no preferential direction along which the water molecules move. This assumptions does not hold in white matter, where we have bundles of axons coherently oriented. In this situation, the cellular bodies act as a physical barrier to the process of diffusion, restricting molecular motion to take place mainly along the preferential direction of the fibres (see Figure 2.4 for a graphical representation of the concept).

Thus a single scalar D, representing the diffusion coefficient in a perfectly isotropic environment, is not adequate when describing a system where the diffusion does exhibit a dependence on the specific direction along which it is measured. Basser and colleagues (Basser, Mattiello, et al., 1994) released the constraint of isotropy in the following way, through the introduction of diffusion tensor imaging (DTI):

$$\begin{cases} S = S_0 e^{-b r^\top \mathbf{D} r} \\ b = \gamma^2 G^2 \delta^2 (\Delta - \delta/3) \end{cases} \tag{2.11}$$

where r is the specific direction along which the diffusion signal is sensitized and D is the diffusion tensor, described by:

$$D = \begin{pmatrix} d_{xx} & d_{xx} & d_{xx} \\ d_{yx} & d_{yy} & d_{yz} \\ d_{zx} & d_{zy} & d_{zz} \end{pmatrix} \tag{2.12}$$

Similarly to the procedure described for DWI, The diffusion tensor D can be recovered using LLS fitting routines. As the tensor can be described by a symmetric 3x3 matrix, it is completely characterized by six degrees of freedom (i.e. d_{xx}. d_{yy} ,d_{zz} d_{xy} d_{xz} d_{yz}). Thus, not counting the S_0 image, at least 6 non-collinear directions are needed to fit the DTI model. Once recovered, the voxel-wise diffusion tensor is usually processed through spectral decomposition, and its eigenvectors (ϵ_1, ϵ_2, ϵ_3) and its eigenvalues (λ_1, λ_2, λ_3) are recovered. Starting from this decomposition, several indexes are then quantified. Amongst them, the most commonly used are the following:

- **Fractional Anisotropy (FA)**: FA is a measure of directional selectivity of the diffusive process inside a voxel. It varies in $[0-1]$ and is mathematically defined as:

$$FA = \sqrt{\frac{(\lambda_1 - \lambda_2)^2 + (\lambda_2 - \lambda_3)^2 + (\lambda_1 - \lambda_3)^2}{2(\lambda_1^2 + \lambda_2^2 + \lambda_3^2)}} \tag{2.13}$$

  An elongated diffusion tensor is represented by high FA values ($FA \to 1$) while spherical tensors (i.e isotropic diffusion) are represented by FA values close to zero. Figure 2.5 represents these situations (displayed as a ellipsoid) at different values of FA.

- **Mean Diffusivity (MD)**: MD is a measure which represents the averaged diffusion coefficient based on the eigenvalues of the diffusion tensor. It is defined as:

$$MD = \frac{\lambda_1 + \lambda_2 + \lambda_3}{3} \tag{2.14}$$

Although not mathematically equivalent, it is conceptually similar to the
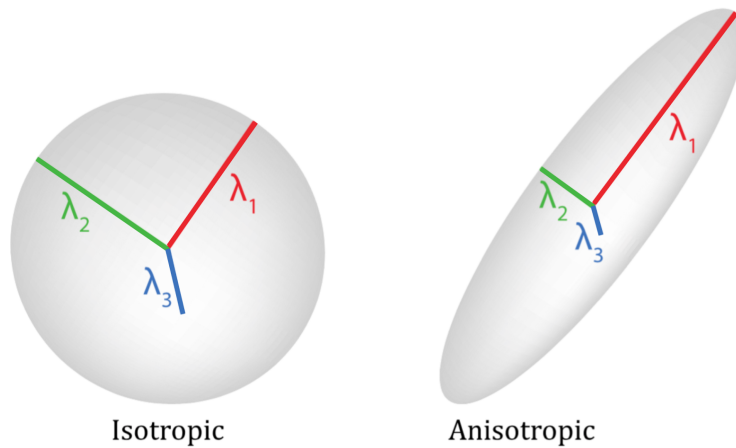
Figure 2.5: The shape of diffusion ellipsoids at different values of fractional anisotropy (FA). Elongated ellipsoids correspond to high values of FA while perfect spherical ellipsoids have FA=0. Reproduced from `http://www.diffusion-imaging.com/2015/10/what-is-diffusion-tensor.html`.

ADC quantified with the DWI technique.

- **The principal direction of diffusion**: the principal eigenvector of the tensor (ϵ_1) is a tridimensional vector representing the main direction along which water diffuses in a given voxel. Its spatial variation can be represented by direction-encoded color (DEC) maps.

Illustratory examples of FA, MD and DEC maps are shown in Figure 2.6

2.4 White-matter microstructure imaging: a brief introduction

DWI and DTI are the basic techniques with which properties of water diffusion inside brain tissues can be inferred to recover important information regarding the cellular architecture and its possible damage due to a number of pathologies. Although sensitive to structural alteration, metrics like FA and MD quantify diffusion characteristics which may be due a plethora of different causes. Cellular loss/proliferation, changes in the organization of axonal fibers, demyelination and the possible presence of oedema may all be causes of significant changes of DTI indexes. Thus, the real cause underlying their possible modifications are not properly known, limiting the usefulness of this technique. *Microstructure diffusion models*, on the other hand, aim to give a mechanistic description of the brain architecture by associating specific biophysical meaning to each of their
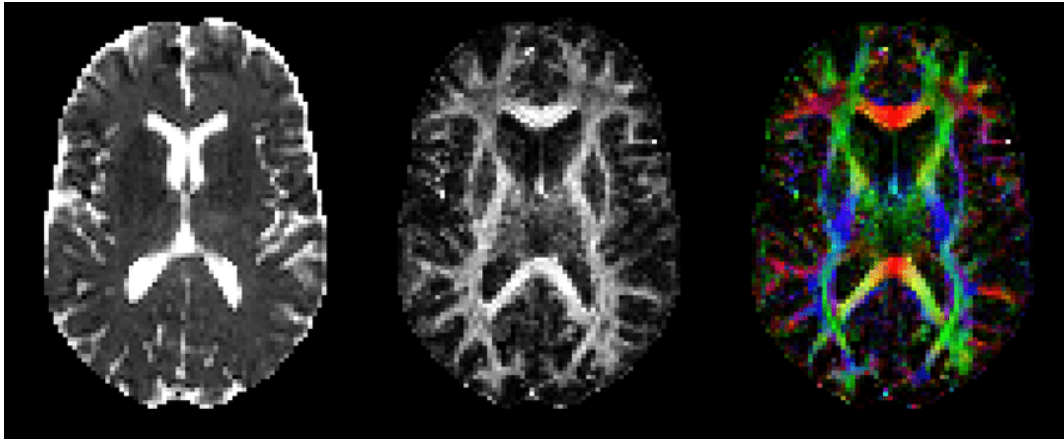
Figure 2.6: The main three parameter maps which are extracted with diffusion tensor imaging. To the left, the mean diffusivity map; in the middle the fractional anisotropy map; to the right, the direction-encoded color map showing the voxel-wise principal orientation of diffusion (red: left-right direction, green: anterior-posterior direction, blue: superior-inferior direction).

parameters. Given its close link with structural features, dMRI is one of the most suitable techniques on which such models can be built. The identification of diffusion-based microstructure models allows to recover a multitude of metrics which can be thought to be surrogates of histological measures. Figure 2.7 shows several characteristics which may be recovered from these techniques.

Amongst others, these include fractional volume densities occupied by axons and the extracellular space, the geometrical spreading of fibre bundles and cellular population sizes. In most cases, the modeling paradigm is relatively straightforward: a particular biophysical object is simplified to a geometry which captures its relevant features. A diffusion protocol designed to optimally characterize the parameters of the simplified geometry is studied, and its attenuation model is subsequently fitted to the acquired data. Figure 2.8 illustrates this process for axonal fibres.

The first diffusion-based microstructure model for white matter was proposed by Stanisz and colleagues (Stanisz et al., 1997). The technique featured in this study designated individual compartments for glial cells, axons and the extra-cellular space, aiming to estimate the volume fraction of each compartment and the spatial dimensions of the cellular populations. The structure of this model has 9 degrees of freedom and requires an extensive set of images acquired at multiple diffusion times and gradient strengths to be fit. The need for a demanding acquisition protocol rendered this approach difficult to transpose clinically. Building upon this work, a plethora of models have since then be presented
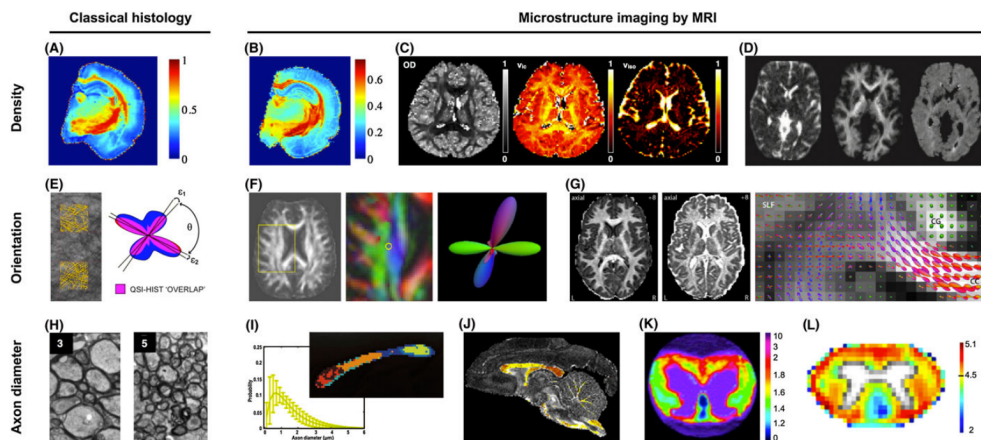
Figure 2.7: Examples of histological features which can be measured by biopsy/subsequent cellular microscopy and their surrogate retrieved with microstructure imaging MRI. A-D, Imaging indices of neurite (axon or dendrite) density with classical histology (A) and by model-based dMRI (B-D). E-G, Imaging fibre orientation distribution. Estimation of fibre directions from histology (E) and corresponding estimates from dMRI (F,G). H-L, Imaging indices of axon diameter. Histology-based high-resolution maps enabling measurements of individual axon diameters (H) and their dMRI-based estimation (I-L). Adapted from (Alexander et al., 2019).

(Alexander et al., 2019; Dmitry S Novikov, Els Fieremans, et al., 2019). As seen in Figure 2.8, they mostly focus on a two- or three-compartment (representing intra-axonal,extra-axonal and, if included, cerebrospinal fluid) structure without exchange to describe the diffusion signal from white matter. Water diffusion in myelin sheets surrounding axons would require an additional compartment, but its contribution to the overall dMRI signal is irrelevant due to its short T2 relaxation time (Jelescu and Budde, 2017).

2.5 Tractography: a brief introduction

As noted in a previous section, one of the key quantities which can be recovered by fitting the voxel-wise diffusion tensor is λ_1, the principal orientation of the diffusive motion of water molecules. The local directions recovered in each voxel may then be pieced together to obtain a picture of long and short pathways connecting different regions of the brain. This process is usually labelled as *tractography* or *fiber tracking*. Tractography algorithms reconstruct *streamlines* (Conturo et al., 1999; Mori, Crain, et al., 1999), which are curves in a defined 3D space with the property of being tangent in each of their points to the local
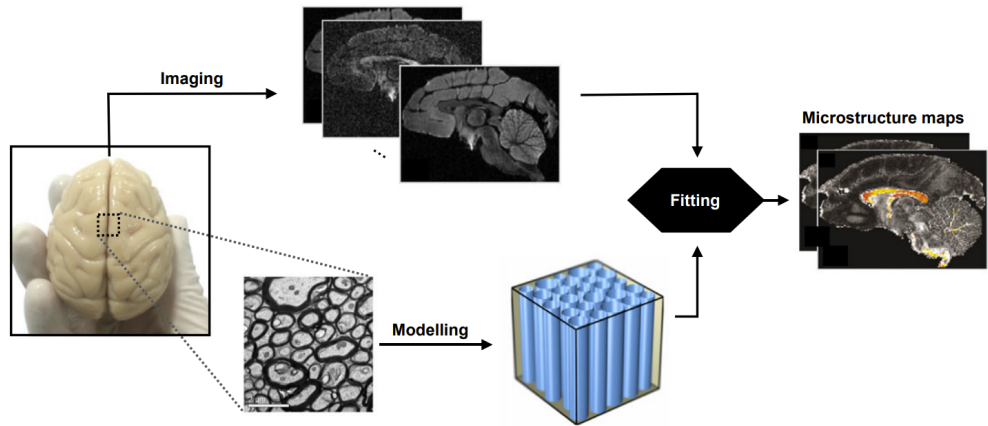
Figure 2.8: The modeling paradigm for axonal fibres in the brain. At first, the complex biological architecture is approximated to a standard geometry whose diffusion properties can be described in parametrical terms. Subsequently, dMRI images from a suitable protocol are acquired and parameter maps are computed. Reproduced from (Alexander et al., 2019).

direction of diffusion. In mathematical terms:

$$\frac{d\mathbf{r}(s)}{ds} = \mathbf{v}(\mathbf{r}(s)) \tag{2.15}$$

where s is the varying arc length, $\mathbf{r}$ is the 3D position along the streamline, and $\mathbf{v}$ is the local diffusion orientation at the position $\mathbf{r}$. Having at disposal the vector field containing all diffusion directions in the brain, the most basic way to reconstruct the streamlines is by performing Euler Integration (Mori, Crain, et al., 1999):

$$\mathbf{r}_{i+1} = \mathbf{r}_i + \mathbf{v}(\mathbf{r}_i)\Delta \tag{2.16}$$

which is equivalent to say that, given a starting point $\mathbf{r}_0$, the reconstruction of r_1 involves following the field direction $\mathbf{v}(\mathbf{r}_0)$ for a short distance Δ, also called *step size*. The new position will be called $\mathbf{r}_1$, and the process can begin anew until some termination criteria are met. The process of streamline reconstruction is visualized in Figure 2.10

Euler's method falls into the category of first-order integration methodologies, which assume that $\mathbf{v}$ is constant along the distance Δ. This assumption generally does not hold, especially in highly curved regions. While one simple solution is the reduction of the step size, it may be beneficial to use Runge-Kutta integration methodologies (Butcher, 1996), which are less biased by these integration errors (Basser, Pajevic, et al., 2000). In its simplest form, diffusion tractogra-
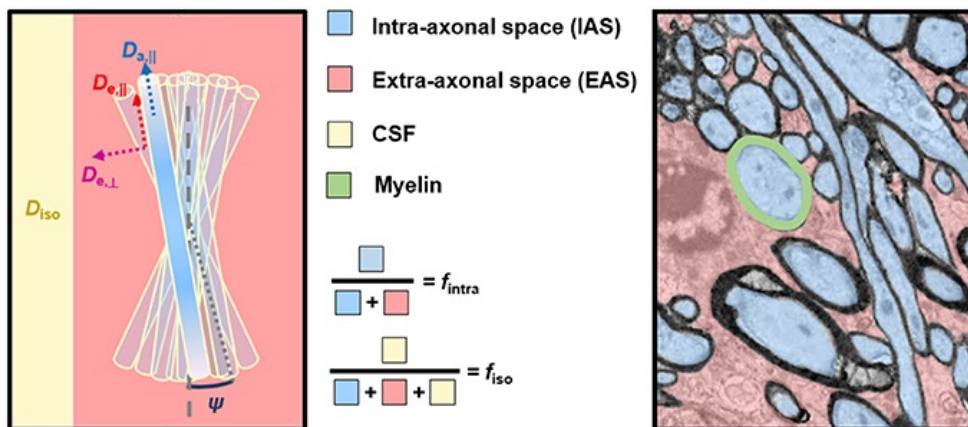
Figure 2.9: General modeling schematics (left) and white matter tissue components (right). The definition of the various compartmental diffusivities and volumetric fractions depend on each model specific formulation. Myelin sheats are not treated as a compartment due to their minimal contribution to the diffusion signal caused by their short T2 relaxation time. Reproduced from (Jelescu and Budde, 2017).

phy relies on DTI to extract the principal diffusion direction occurring inside a voxel. Such a diffusion description may be too simplistic in cases of complex architectural configurations such as crossing fibres (Savadjiev et al., 2008). Multiple solutions, usually labelled *higher order models*, have been proposed through the years to extract diffusion directions from multiple fibre populations in single voxels (Dell'Acqua et al., 2017). These approaches require richer dMRI protocols than ones used to fit DTI, but are demonstrated to produce fiber trajectories which are biologically more plausible in general (Jeurissen, Leemans, et al., 2011). Amongst them, spherical deconvolution (SD) is arguably the most notorious advanced approach (J-Donald Tournier, Calamante, Gadian, et al., 2004), estimating voxel-wise fiber orientations as a probability distribution function varying on the unit sphere (fiber orientation distribution, FOD). FODs are usually forced to yield non-negative values using constrained spherical deconvolution (CSD, J-Donald Tournier, Calamante, and Connelly, 2007), an improved version of SD which gives more physiologically plausible results, is robust to noise fluctuations and provides better angular contrast.

Another key feature of fiber tracking algorithms regards the nature of the sampling of the diffusion direction at each point of the streamline construction process. Such nature may be either deterministic or probabilistic, with the following differences:

- Deterministic algorithms assume there is a single diffusion orientation in
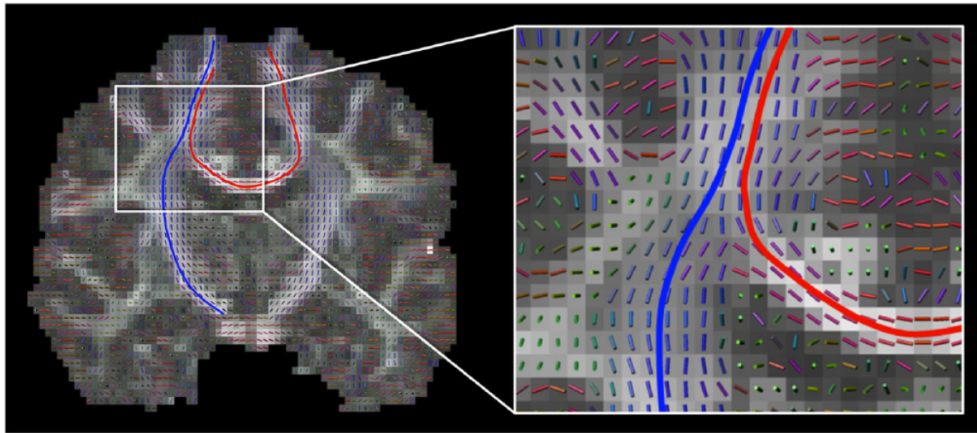
Figure 2.10: The vector field which contains the local predominant diffusion direction and two streamlines. The red one is part of the corpus callosum, while the blue one is part of the cortico-spinal tract. In each voxel, streamlines are tangent to local orientations. Reproduced from (Jeurissen, Descoteaux, et al., 2019).

each voxel of the brain. This direction is chosen with empirical criteria, such as selecting the principal eigenvector of the diffusion tensor (e.g. DTI-based tracking) or picking the maximum of an orientation distribution function (e.g. CSD-based tracking).

- Probabilistic algorithms, on the other hand, assume that multiple fiber populations with different directions may coexists in a single voxel. As such, at each streamline point, the direction to follow is sampled from a continuous probability function (i.e., the orientation distribution function, ODF). Probabilistic approaches are preferred by some authors because they think they better approximate the biological variability of white matter tracts in the human brain (J-Donald Tournier, Calamante, and Connelly, 2012).

Example of different tractography approaches to reconstruct the cortico-spinal tract are shown in Figure 2.11. As it can be noted from the figure, deterministic DTI approaches (left) provide the most essential description of the axonal pathways of the brain. Indeed, DTI-based probabilistic algorithms (center) may allow for a more extensive delineation of main fiber bundles. However, it is by combining probabilistic sampling with higher order diffusion models such as CSD (right), that one achieves the maximum sensitivity in tracking the most peripheral fibers. While certainly appearing more capable in describing the intricate nature of the connection of the human brain, probabilistic CSD-based tractography algorithms are far from being perfect. The more complex the reconstruction process is, the

more susceptible it becomes to errors, giving birth to streamlines which depict nonexistent connections in the brain. This is the problem of the so called 'false positive connections' (Maier-Hein et al., 2017). The opposite problem, 'false negative connections' (i.e. the failure to reconstruct truly existent connections) is also present, and tends to affect DTI-based algorithms more than the advanced alternatives (Knösche et al., 2015).

| DTI (deterministic) | DTI (probabilistic) | CSD (probabilistic) |
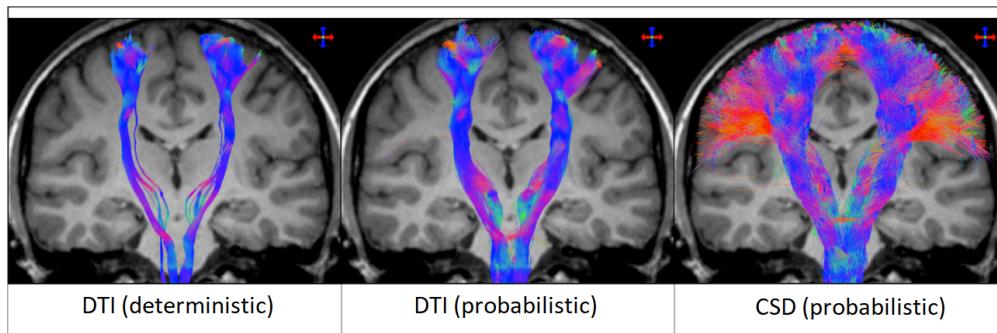
Figure 2.11: The corticospinal tract of a single subject reconstructed with three different tractography approaches. To the left, DTI-based computation of the principal orientation and deterministic direction sampling. In the middle DTI-based computation of the principal orientation and probabilistic direction sampling. To the right CSD-based computation of the principal orientation and probabilistic direction sampling. Adapted from (Calamante, 2019). DTI = diffusion tensor imaging, CSD = constrained spherical deconvolution.

.

Chapter 3

Diffusion-based microstructure models in brain tumours: fitting in presence of a model-microstructure mismatch

3.1 Introduction

Since its introduction as a tool of outstanding sensitivity to detect early cerebral ischemic changes in acute stroke patients (Van Everdingen et al., 1998), diffusion magnetic resonance imaging has proven its invaluable usefulness in probing tissues' microstructure. Notoriously, the involvement of invasive techniques such as biopsy and subsequent pathological studies are required to retrieve detailed information concerning the anatomy of the brain.

   With the advent of dMRI, some of these important features became non-invasively accessible. In this field, Diffusion Tensor Imaging (Basser, Mattiello, et al., 1994) stands out as the most prominent and widely known approach to measure the anisotropic nature of water motion inside biological tissues, both in vivo and ex vivo.

   Although sensitive to microstructural variations, DTI metrics suffers from poor specificity, as they may be affected by both neurite density and geometrical alterations (Jacques-Donald Tournier et al., 2011). To overcome this issue, the joint use of high angular resolution diffusion and the multi-compartment modelling of the dMRI signal gave birth to techniques labelled as 'microstructure imaging' (Alexander et al., 2019), whose aim is that of virtual histology. These

35

models hypothesize that the voxel-wise diffusion signal arises from the composition of several microenvironment of the brain (e.g., cerebrospinal fluid, intra/extra axonal spaces) and try to recover their relative contributions to it in a data-driven fashion.

Although it is possible to fit microstructure models to detect structural changes caused by different pathologies, whenever the normal appearing tissues are disrupted, the generalized use of these techniques requires some additional cares. Such is the case of brain tumours.

In this context, several hypotheses of these techniques, concerning cell shapes and water diffusivities, no longer hold. This divergence between the biophysical model and the underlying microarchitectural truth causes the impossibility to have a clear physiological interpretation of the diffusion signal (Wen et al., 2015).

Despite the presence of these issues, current state-of-the-art literature is no stranger to the employment of these techniques in gliomas, with a major focus on the use of the Neurite Orientation Dispersion and Density Imaging (H. Zhang et al., 2012) (NODDI) model. Listing some examples, Masjoodi et al. (Masjoodi et al., 2018) found good separation between oedema, tumour and normal-appearing tissues; Maximov et al. (Maximov et al., 2017) and Li et al. (S.-H. Li et al., 2019) showed significant differentiation between different glioma grades, while Kadota et al. (Kadota et al., 2020) found good discrimination between gliomas and solitary brain metastases. Additionally, Caverzasi et al. (Caverzasi et al., 2016) proposed colour encoded maps of NODDI volumetric fractions which enable fine visual characterization of neoplastic pathologies.

Successful applications like these open the interesting question whether a microstructure model (a mathematical expression which gives specific biophysical meaning to its parameter estimates) outside of its physiological assumptions may be used as a signal representation (an approximate mathematical description of the data, not based on any theory on the composition of the signal it describes) (Dmitry S Novikov, Kiselev, et al., 2018). For example, the entire scientific field of radiomics (Timmeren et al., 2020) relies on the data-driven analysis of texture features, whose link to specific physio-pathological properties is questionable. Radiomics-based models succeed in explaining tumour phenotypes, giving precious information to decision-support techniques for personalized treatment (Aerts et al., 2014). With the increasing use of machine learning techniques in the dMRI field (Ravi et al., 2019), parameter maps coming from NODDI or similar alternatives may prove as useful biomarkers to use in conjunction with other imaging modalities to support tumour classification and disease progression

monitoring. The current state of the art literature, however, lacks a thorough examination whether proper parameter estimation of these techniques is feasible in tumoral tissues. Indeed, without this assessment, no further consideration regarding the value a parameter may have in this different environment can be made.

Given these premises, in this work we deal with this first-level question. We here aim to investigate whether diffusion-based microstructure models can be properly identified in an environment far from that of their conception. Without making any inference about the physiological meaning and specificity of these techniques in tumours, the assessment we propose here has a main focus on two specific topics: 1) Are there significant model biases in fitting these techniques in the tumoral lesion? 2) Is the accuracy of the parameter estimates completely disrupted by the physiological implausibility of the employed diffusion model?

We tackle these questions by fitting two microstructure models from the literature on a cohort of 11 brain tumour patients and comparing their performance both in the normal-appearing brain and in the tumoral lesion. We are not interested here in comparing performance between models, but between tissues using the same technique. In particular, because of the growing number of studies using NODDI and the possibility of estimating the compartmental diffusivities (which are not estimated in NODDI) with the direction-averaged approach proposed by the Spherical Mean Technique (Kaden, Kruggel, et al., 2016; Kaden, Kelm, et al., 2016) (SMT), we mostly focus on these two mathematical structures. Additionally, we include in our analysis the Diffusion Kurtosis Imaging (DKI) signal representation (Jens H Jensen et al., 2005; Steven et al., 2014). Due to not making any hypothesis on the underlying microstructure geometry, DKI does not suffer from the above-mentioned mismatch and may be used as reference for intra-model comparison of quality of fit measures in different tissues (Dmitry S Novikov, Kiselev, et al., 2018). We here performed an analysis of model fitting results using the following statistical tools:

- The Model's Residual Sum of Squares (RSS): The RSS will be computed to evaluate the average goodness of fit for all tissues.

- The Uncertainty of parameter estimates: standard deviations of parameter estimates were computed as their Cramer-Rao Lower bound (CRLB) and statistical bootstrapping of the model.

- The generalized sensitivity functions (GSFs): in this work, GSFs introduced to investigate the sensitivity of parameter estimates to the employed diffu-

sion protocols. In other words, can a single diffusion protocol yield reliable parameter estimates in both normal appearing and pathological tissues? We look for an answer to this question using this tool.

The rest of the text is organized as follows. In the "Methods" section, the investigated models/signal representations are briefly introduced, along with the dMRI acquisition details and the framework we use to evaluate model performance. In the "Results" section we report the outcomes separately for each analysis and, lastly, the "Discussion and Conclusion" section provides contextualization of our findings. Here, we highlight the contribution of this work to the literature and discuss its limitations.

3.2 Methods

Firstly, this section gives a brief overview of the models used in this work. As a second point, we explain the metrics we use to evaluate their performance.

3.2.1 Models and signal representations

The two techniques we fitted to oncological data were the original NODDI implementation and the bi-compartment SMT. These models, while providing different physiological information, share modest protocol requirements in terms of gradient performance. Indeed, one hundred diffusion directions distributed following the static repulsion of charges, taken across two b-shells, are not only sufficient, but also reported as optimal (H. Zhang et al., 2012). Whole brain quantification is relatively fast, taking 4 hours for NODDI (an acceleration down to 5/10 minutes is possible by employing the AMICO framework (Daducci et al., 2015)) and 5 minutes for the SMT on standard machines. Moreover, by employing solely tensor-like components for the construction of their compartments, they allow the use of the b-value quantity to define the overall diffusion weighting, thus bypassing the need for the separate introduction of its 'microparameters' such as gradient strength and diffusion time. These qualities mark the reason why they are preferentially selected by clinical studies investigating brain microstructure. The DKI technique can be fitted on a similar protocol to the one described above, as the higher b-shell (provided it has $b > 1500 s/mm^2$) disentangles the non-Gaussian effects of water diffusion in the brain.

NODDI

Arguably the most widely known diffusion-based microstructure model, NODDI, adopts a three-compartment formulation aimed to describe the overall signal as a composition of diffusive behaviours in three different environments. As such, the general equation of the model has the following form:

$$A = (1 - V_{iso})(V_{ic}A_{ic} + (1 - V_{ic})A_{ec}) + V_{iso}A_{iso} \tag{3.1}$$

where A is the acquired normalized dMRI signal, V_{iso} is the isotropic volume fraction and V_{ic} is the intracellular volume fraction. Representing the normalized signal of three compartments, A_{ic} A_{iso} and A_{ec} respectively model the intracellular space by using Watson distributed sticks, the extracellular space with an anisotropic tensor and the free water content with a perfectly isotropic tensor. Figure 3.1 contains a graphical depiction of the structure described by (3.1). The diffusion signal arising from each compartment (i.e A_{ic} A_{iso} and A_{ec}) has its own mathematical formulation, which can be found in the original article presenting the model (H. Zhang et al., 2012). Accounting for NODDI in its entirety, the complete set of model parameters to be estimated is:

1. V_{ic} [unitless], the intracellular volume fraction.

2. κ [unitless], concentration parameter of the Watson distribution (present in the mathematical formulation of A_{ic}) .

3. V_{iso} [unitless], the isotropic volume fraction.

4. Θ [rad], first Euler angle to describe the mean orientation of the Watson distribution in spherical coordinates (present in the mathematical formulation of A_{ic})

5. ϕ [rad], second Euler angle to describe the mean orientation of the Watson distribution in spherical coordinates (present in the mathematical formulation of A_{ic}).

It is worth mentioning that, while technically κ is the model parameter, the original authors propose to visualize and evaluate the so-called Orientation Dispersion Index, which ranges between 0 and 1 and, more intuitively than κ, maps higher axonal dispersion into higher values. The fitting routine for NODDI determines the maximum likelihood of parameter estimates with the assumption of additive Rician noise in two steps. Firstly, a brute force search is performed
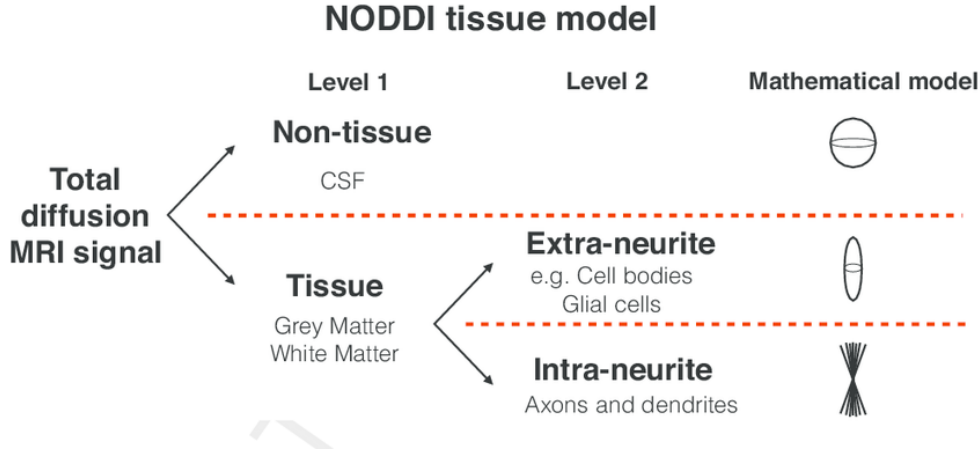
Figure 3.1: Breakdown of the total normalised diffusion MRI signal as modelled by Neurite orientation dispersion and density imaging. reproduced from (Tariq et al., 2016).

over a coarse and regular grid of possible parameter combinations to provide a preliminary, rough estimate. As nonlinear estimators can be highly sensitive to the initial choice of the parameters, this preliminary step offers reasonable initialization conditions. Consequently, results from the previous phase are carried over to be used as a starting point for the non-linear optimization procedure involving the Gauss-Newton technique. In both steps, the cost function to minimize is the rician log-likelihood function L_{ric} (Alexander, 2008), described as:

$$L_{ric} = \sum_{n=1}^{M} (log(S_n(b, \mathbf{G})) - 2log(\sigma) + log(I_0(\widetilde{D}_n) - \widetilde{A}_n) \qquad (3.2)$$

where $\tilde{D}_n$ and $\tilde{A}_n$ are respectively defined as:

$$\tilde{A}_n = \frac{S_n(b, \boldsymbol{G})^2 + \tilde{S}_n(b, \boldsymbol{G})^2}{2\sigma^2} \qquad (3.3)$$

$$\tilde{D}_n = \frac{\tilde{S}_n(b, \boldsymbol{G})S_n(b, \boldsymbol{G})}{\sigma^2} \qquad (3.4)$$

With σ being the standard deviation of the gaussian distribution underlying the Rician distribution, S_n the n-th measurement, $\tilde{S}_n$ the n-th model prediction, b the b-value, G the diffusion gradient direction, M the total number of acquired q-space points and I_0 the Bessel function of the first kind. During the optimization, the volumetric fractions are constrained to belong to the [0-1] interval, while the

free water diffusion coefficient (present in the mathematical formulation of A_{iso}) and the intrinsic free diffusivity (present in the mathematical formulation of A_{ic}) are respectively fixed to $d_{iso} = 3 \cdot 10^{-3} mm^2/s$ and $d_{in} = 1.7 \cdot mm^2/s$.

SMT

The Spherical Mean Technique model exploit the powder averaging (Kroenke et al., 2004; Callaghan et al., 1979) of the angularly varying diffusion MR signal to obtain a measurement which is independent from the orientation distribution function (ODF) of fibers. As such, SMT does not explicitly model the diffusion signal but rather its b-value dependent mean. Following this rationale, Kaden and colleagues (Kaden, Kelm, et al., 2016) proposed a bi-compartment model, separating intracellular and extracellular environments, in the following form:

$$\bar{e}_b = v_{int}\bar{e}_b^{int} + (1 - v_{int})\bar{e}_b^{ext} \tag{3.5}$$

where $\bar{e}_b$ is the averaged spherical mean of the dMRI signal, v_{int} is the intracellular volume fraction and the two compartments have the following formulations:

$$\bar{e}_b^{int} = \frac{\sqrt{\pi}erf(\sqrt{bd_{||}})}{2\sqrt{bd_{||}}} \tag{3.6}$$

$$\bar{e}_b^{ext} = e^{-bd_{ext}}\frac{\sqrt{\pi}erf(\sqrt{b(d_{||} - d_{ext})})}{2\sqrt{b(d_{||} - d_{ext})}} \tag{3.7}$$

where erf is the error function, $d_{||}$ is the intrinsic diffusivity and d_{ext} follows the tortuosity model $d_{ext} = (1 - v_{int})d_{||}$ (Stanisz et al., 1997). Unlike NODDI, no compartment is devoted to account for cerebrospinal fluid presence, and diffusivity values are central in the estimation process instead of being fixed quantities. In this case, the complete set of parameters to be estimated is:

1. v_{int}, the intracellular volume fraction.

2. $d_{||}$, the intrinsic diffusivity inside axons.

Another remarkable difference from the NODDI model is the choice of the estimator: the SMT bi-compartment model employs a constrained unweighted nonlinear least square approach with the following cost function:

$$C = \sum_{i=1}^{N}(\bar{e}_{b_i} - \hat{e}_{b_i}(v_{int}, d_{||}))^2 \tag{3.8}$$

where N is the number of spherical mean images, $\bar{e}_{b_i}$ is the spherical mean of the diffusion signal taken at the i-th shell and $\hat{e}_{b_i}$ is the prediction of the SMT bi-compartment model. (3.7) is subject to the constraints $v_{int} \in [0-1]$ and $0 < d_{\parallel} < d_{free}$, which take place to ensure both diffusivities lie in a physically meaningful range. The bulk water diffusivity constitutes the upper bound, with a body-temperature approximate value of $d_{free} = 3.05 \mu m^2/ms$.

DKI

The DKI is the straightforward extension of the DTI model which adds a quadratic term in the b-value series expansion of the dMRI signal to quantify the degree of non-gaussian diffusion happening inside the different tissues. Like DTI, DKI does not make any physiological assumptions about possible diffusion behaviours inside/outside cellular object and is therefore referred to a signal representation. The formula for the DKI is given by the second-order approximation of the Taylor expansion of the noiseless diffusion-weighted signal around b=0:

$$ln[S(\mathbf{b}, \mathbf{g})] = ln[S(0)] - b\sum_{i,j=1}^{3} g_i g_j D_{i,j} + \frac{b^2}{6}(\sum_{i=1}^{3} \frac{D_{ii}}{3})^2 \sum_{i,j,k,l=1}^{3} g_i g_j g_k g_l W_{ijkl} \quad (3.9)$$

where S is the diffusion signal, g_i are the diffusion gradient directions, D_{ij} are the components of the diffusion tensor and W_{ijkl} are the components of the diffusion kurtosis tensor. As the fitting of the DKI model can be formulated as a linear regression problem, we used the readily available MATLAB toolbox implementing the weighted linear least-square estimator (Veraart, Sijbers, et al., 2013) described by the equation:

$$p = (\mathbf{X^T W X})^{-1} \mathbf{X W y} \quad (3.10)$$

where $\mathbf{p}$ is vector containing the parameters of the model, $\mathbf{X}$ is the design matrix of the regression problem, $\mathbf{y}$ is the vector of the observed diffusion signal, and $\mathbf{W}$ is the diagonal weight matrix containing the square of the observed signal.

3.2.2 Assessment Metrics

Residual Analysis

One of the most practical ways to assess whether a model can accurately represent the diffusion signal is to look at the behaviour of its residuals, which are defined

as:

$$r(b_i, \mathbf{G}_i) = S(b_i, \mathbf{G}_i) - \hat{S}(b_i, \mathbf{G}_i) \qquad (3.11)$$

where S is the measured signal, $\hat{S}$ is the model prediction, b_i is the b-value and $\mathbf{G}_i$ is the diffusion gradient direction. To explain their usefulness, let the diffusion signal be represented as:

$$S(b_i, \mathbf{G}_i) = S_{true}(b_i, \mathbf{G}_i) + n(b_i, \mathbf{G}_i) \qquad (3.12)$$

where S_{true} is the physiological source of the signal and n is the additive noise. Under the hypothesis that our microstructure model is a good approximation of noiseless source, i.e. $\hat{S} \cong S_{true}$, the model residuals are an estimation of a random realization of n:

$$r(b_i, \mathbf{G}_i) = n(b_i, \mathbf{G}_i) \qquad (3.13)$$

From (3.13), we essentially assess whether model residuals are centred around zero and whether their variances are comparable to that of the additive noise. Such a qualitative analysis, valid in the case of gaussian noise, is extended to the rician case, as for SNR > 2 the two probability distributions have similar properties [24]. When looking at MR images composed by several hundred thousand voxels, the inspection of all generated residuals is often performed by simply computing the Residual Sum of Squares to recover a voxel-wise scalar measure of model fit quality. The RSS is mathematically defined as:

$$RSS = \sum_{i=1}^{N} r(b_i, \mathbf{G}_i)^2 \qquad (3.14)$$

where N is the number of the acquired q-space points. Under the hypothesis noise is invariant to the gradient direction and b-value changes, one can also derive a voxel-wise estimation of the standard deviation of the measurement noise. For each voxel, this was done by approximating σ as the standard deviation computed across the multiple b0 measurements (Jacques-Donald Tournier et al., 2011). Subsequently, we computed the expected RSS (i.e, the RSS a model should approximately have if it is in accordance with the underlying noise hypotheses) as:

$$E[RSS] = \sigma^2 N \qquad (3.15)$$

Uncertainty of estimated microstructure parameters

To assess whether the estimation process of the given model yields robust and reproducible results in vivo, it is necessary to understand how the intrinsic variance of the measurement error affects the final parameter estimate. One way to tackle these problems relies on the use of statistical bootstrapping (Efron et al., 1994) to extract variability from the dataset. Statistical bootstrapping in the modelling context can be summarized by the following steps:

1. Fit the MR signal with the employed diffusion model and compute the model prediction and residuals.

2. Obtain a unique permutation of the extracted residuals and add it the model prediction.

3. Fit the newly synthetized diffusion signal with the model again, obtaining a new vector of parameter estimates.

4. Given all the iterations, compute the standard deviation of parameter estimates.

This technique requires extensive computational power, as multiple model fitting steps are required to achieve statistical significance. A second, less time-demanding, strategy can be pursued by exploiting a theoretical result from the mathematical statistics frame known as the Cramer-Rao Lower Bound (CRLB). Briefly, let the Fisher information matrix be:

$$J_{i,j} = E[\frac{\partial^2 L}{\partial w_i \partial w_j}] \tag{3.16}$$

where L is the log likelihood of the measurement with the appropriate noise model and $w_{i,j}$ are the model parameters. If the partial derivatives $\partial L/\partial w_i$ exist, the used estimator is unbiased and matrix J is invertible, then:

$$\Sigma_p \succeq J^{-1} \tag{3.17}$$

where Σ_p is the covariance matrix of the parameter estimates. (3.17) effectively means, for the single model parameters that:

$$\sigma^2 \geq (J^{-1})_{i,j} \tag{3.18}$$

The Fisher information matrix J has a closed form solution when the additive noise model is gaussian. However, when this assumption becomes Rician, which

is valid in general for MR magnitude images (Gudbjartsson et al., 1995), the formulation becomes less trivial and, borrowing the results from (Alexander, 2008), the information matrix becomes:

$$J_{i,j} = \sum_{k=1}^{K} \frac{1}{\sigma^4} \frac{\partial \hat{S}_k}{\partial w_i} \frac{\partial \hat{S}_k}{\partial w_j} (Z_k - \hat{S}_k^2) \tag{3.19}$$

where K is the number of measurements and Z_k has the following form:

$$Z_k = \int_0^\infty \hat{S}_k^2 I_1^2(\frac{\hat{S}_k S}{\sigma^2}) I_0^2(\frac{\hat{S}_k S}{\sigma^2}) P_{ric}(S) dS \tag{3.20}$$

where $I_{0,1,\ldots,n}$ are the modified Bessel functions of the first kind and P_{ric} denotes the Rician distribution. As presented in the original article (Alexander, 2008), the integral in (3.20) requires numerical approximation and computing its exact values for Z_k is computationally intensive. Thus, we precompute a grid of possible fixed values and rely on linear interpolation to recover pointwise estimates. The evaluation of CRLB derived variance metrics and the model residuals are common practice in modelling in medicine and as such they mark the basis of the analysis in this work.

Sensitivity analysis of the model equations

Sensitivity equations are often used in simulation studies of physiological systems to understand how a variation of model parameters affect model outputs (Frank et al., 1980). They are generally used for optimal experiment design purposes, but we here used them to the test whether the employed protocol was suitable for parameter estimation in all different tissues. More specifically, we adopted the GSFs formulation proposed by Tomaseth and Cobelli (Thomaseth et al., 1999). Briefly, GSFs recover, in a context where time is the independent variable, which temporal sub-intervals are informative for a particular model parameter. This is done by evaluating the Fisher Information conveyed on a model parameter by a hypothetical observation and normalizing it by the total information provided by the entire set of the evaluated observations. Thus, for each model we compute the Generalized Sensitivity matrix as:

$$\mathbf{GS}(b_J) = \sum_{j=1}^{J} [\sum_{m=1}^{M} \mathbf{I}_\theta(b_m)]^{-1} \mathbf{I}_\theta(b_j) \tag{3.21}$$

where GS is the Generalized Sensitivity matrix computed on a subset of the b-values b_J, M is the length of the b-value vector $\mathbf{b} = [b_1, b_2, \ldots, b_M]$, and $I_\theta(\beta)$

is the Fisher Information matrix computed from observations coming from a diffusion shell at b-value equal to β, according to Equation (3.16). GSFs for all separated parameters are then extracted as:

$$\mathbf{gsf}_{\theta}(b_J) = diag(\mathbf{GS}(b_J)) \qquad (3.22)$$

Operatively, we evaluate GSFs for both NODDI and the SMT bi-compartment model on increasingly higher diffusion shells in the range $b \in [0 - 4000]s/mm^2$ with 30 uniformly distributed gradient directions. Model parameter values for the generation of GSFs of a specific tissue were chosen as their median across that tissue for a representative subject of the dataset.

3.2.3 In vivo acquisition

Eleven patients suffering from de novo brain tumours have been scanned at the University Hospital of Padova. All procedures were in accordance with the ethical standards of the institutional research committee and with the 1964 Helsinki declaration plus later amendments. All participants provided informed, written consent in accordance with the local University Hospital Institutional Review Board. DWIs have been acquired on a Siemens Biograph mMR-PET/MR scanner at 3T equipped with the PET compatible 16-channels Siemens head and neck coil (TR/TE 5355/104ms; 2.0x2.0x2.0 mm3). Each volume was composed of 68 slices, acquired in interleaved mode with a multiband accelerator factor of 2 (CMRR, R014) and no in-plane acceleration. The multi-shell diffusion protocol was composed by a total of 100 diffusion weighted images, subdivided in the following way:

- 10 b0 images, with zero diffusion weighting;

- 30 diffusion weighted images at b-value=710 s/mm^2 (Shell 1);

- 60 diffusion weighted images at b-value=2855 s/mm^2 (Shell 2);

In varying the b-value, diffusion time and impulse duration have been kept fixed to values $\Delta = 50.05ms$ and $\delta = 27.77ms$, while gradient strength G was altered. This diffusion HARDI protocol is the optimized two shell NODDI protocol as described in (H. Zhang et al., 2012). Each diffusion volume has been acquired in both Anterior-Posterior (AP) and Posterior-Anterior (PA) phase encoding direction for pre-processing needs, as explained in a subsequent section. In the

same MR session, a reference 3D T2-weighted Fluid Attenuated Inversion Recovery (FLAIR) image (TR/TE $5000/395ms$; $1.0x1.0x1.0mm^3$; FOV 250mm), two T1w structural images (TR/TE $2400/3.2ms$, $1.0x1.0x1.0mm^3$, FOV $256mm$, 160 slices) acquired both before and after contrast agent injection, and a T2w structural image (TR/TE $3200/536ms$, $1.0x1.0x1.0mm^3$, FOV 256mm, $160slices$) were acquired.

3.2.4 Preprocessing of images and tumour segmentation

The acquired diffusion weighted volumes were visually inspected to identify and remove those images affected by interslice instabilities (Bastiani et al., 2019) which were deemed excessively corrupted for subsequent pre-processing techniques to correct. The rest of the pre-processing was executed in its entirety within the MRtrix Software (J-Donald Tournier, R. Smith, et al., 2019) and features an initial denoising step based on random matrix theory (Veraart, Dmitry S Novikov, et al., 2016), and a subsequent call to the tools topup (Andersson, Skare, et al., 2003) and eddy (Andersson and Sotiropoulos, 2016) from the FMRIB Software library (FSL) for B0 inhomogeneity, eddy current and motion joint correction. Tumour masks to separate the tumour core and the oedema from healthy tissue were manually drawn by an expert radiologist on the acquired T1w, T2w and FLAIR images and were subsequently coregistered to the mean b0 volume with the Advanced Normalization Tools (ANTs) (Avants et al., 2011) toolbox. Structural pre-processing was applied to the T1w image of each patient and consisted in bias field correction (N4BiasFieldCorrection, (Tustison et al., 2010)), skull-stripping (Multi-Atlas Skull Stripping, (Doshi et al., 2013)), tissue segmentation (into GM, WM and cortico-spinal fluid, with the unified segmentation tool (Ashburner et al., 2005) of SPM12 v. 7771) and diffeomorphic non-linear registration (as implemented in the SyN algorithm of ANTs) to the symmetric MNI152 atlas. Segmentation results were further registered to the native b0 volume using ANTs by applying an affine transformation previously estimated on the T1w image.

3.2.5 Model Fitting softwares and Statistical Analysis

We fitted NODDI, SMT and DKI to the acquired oncological dataset using off-the-shelf toolboxes which are publicly available (`http://mig.cs.ucl.ac.uk/index.php?n=Tutorial.NODDImatlab` for NODDI, `https://github.com/ekaden/smt` for SMT and `https://github.com/jelleveraart/RobustDKIFittingforDKI`)

and integrated some in-house MATLAB scripts to compute the RSS, the voxel-wise approximation of parameter standard deviations (σ) through the Cramer-Rao inequality (for SMT and NODDI) and statistical bootstrapping (for DKI). Subsequently, by computing the GSFs, we evaluated the general sensitivity of model parameters to investigate whether the different microstructural environments (i.e., WM, GM, tumour core and oedema) affect the optimality of the employed diffusion protocol. Lastly, we briefly discuss the orthogonality of information these diffusion parameters may convey in differentiating the studied tissues. Correlation matrices between voxel-wise values of each pair of diffusion metrics were computed for every subject and tissue along with their across-subject median. Lastly, from these median tissue-specific matrices, we eventually compute the parameter Redundancy Matrix (RM) by thresholding the four matrices at $\rho = 0.5$ and computing their intersection. The RM matrix highlights strong correlations between diffusion metrics which are common to GM, WM, Oedema and the tumour core.

3.3 Results

3.3.1 Signal considerations, model fitting and parameter precisions

Figure 3.2 shows an example of the voxel-wise model fit for NODDI/SMT/DKI and highlights how the three techniques quantify microstructure information in very different ways.While NODDI and DKI capitalize on the entirety of the acquired diffusion signal, the SMT is a model for its spherical mean, thus reducing the number of independent points to the number of the acquired diffusion shells. This has repercussions in terms of the feasibility of residual analyses of the model in case of widely spread two shells HARDI acquisitions such as the one we utilize here: as the model features two degrees of freedom, the fit results in a perfect interpolation of the available data, rendering the computation of residuals trivial and noninformative in terms of goodness-of-fit. In the other two cases, model residuals have definite meaning, and their derived metrics can be reliably quantified. In the representative voxel in the figure, the average of NODDI and DKI residuals are respectively $\mu_{NODDI} = 0.0748$ [A.U.] and $\mu_{DKI} = 0.127$ [A.U.], denoting the absence of model biases in terms of fitting. Standard deviations for this example fit are $\sigma_{NODDI} = 16.61$ [A.U.] and $\sigma_{DKI} = 5.61$ [A.U.], σ_{NODDI} higher than σ_{DKI} but both comparable with the estimation of the noise standard
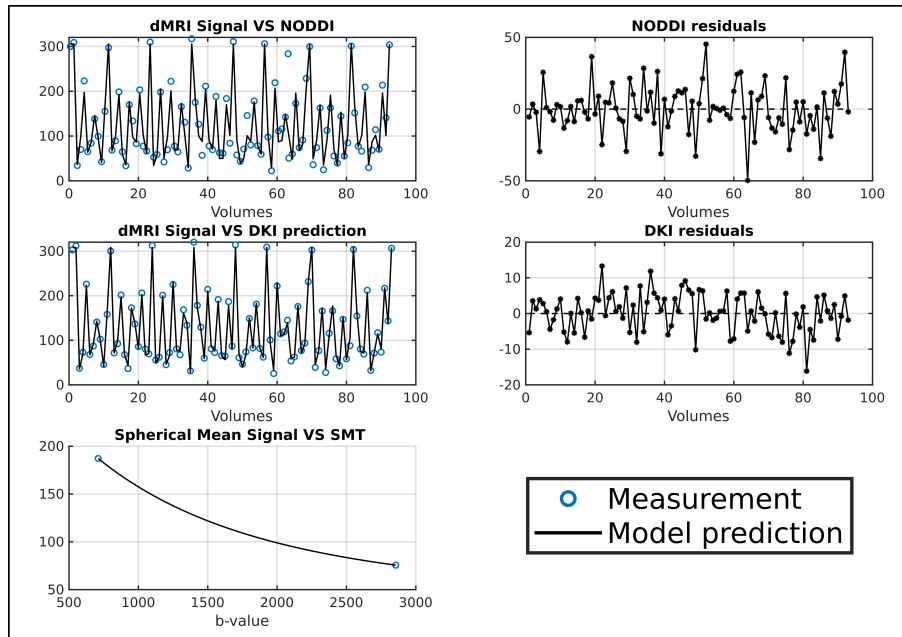
Figure 3.2: On the top row, visualization of the diffusion signal along with NODDI model prediction and its residuals. On the mid row, the DKI model prediction of the diffusion signal and its residuals. On the bottom row, the spherical mean of the signal and the SMT bi-compartment model prediction. NODDI = neurite orientation dispersion and density imaging, SMT = spherical mean technique, DKI = diffusion kurtosis imaging.

deviation through the b0 images $\sigma_{noise} = 6.26$ [A.U.].

Figure 3.3 shows both the maps of microstructure parameters of the three diffusion techniques and those of their relative standard deviation for an axial slice of a representative patient. Although the modelling choices for the various compartments may be physiologically questionable in tumours, the employed parameter estimators are able to react to the different features of the diffusion signal and output spatially coherent metrics, both in terms of their value and uncertainty. NODDI and SMT parameter maps appear to have a good degree of spatial continuity in the pathological area, revealing unique contrasts which are not seen in structural images and in the DKI model. The standard deviation images show a varying degree of spatial smoothness both in normal appearing tissues and in the tumoral lesion. Although standard deviations are very close in numerical values, some slight trends can be observed, where the tumoral lesion appears to have higher precision with respect to normal appearing tissues for all parameters except for NODDI's ODI.

These representative single-slice observations are generalized in Figure 3.4, which shows the boxplot of the voxel-wise parameter values and the standard
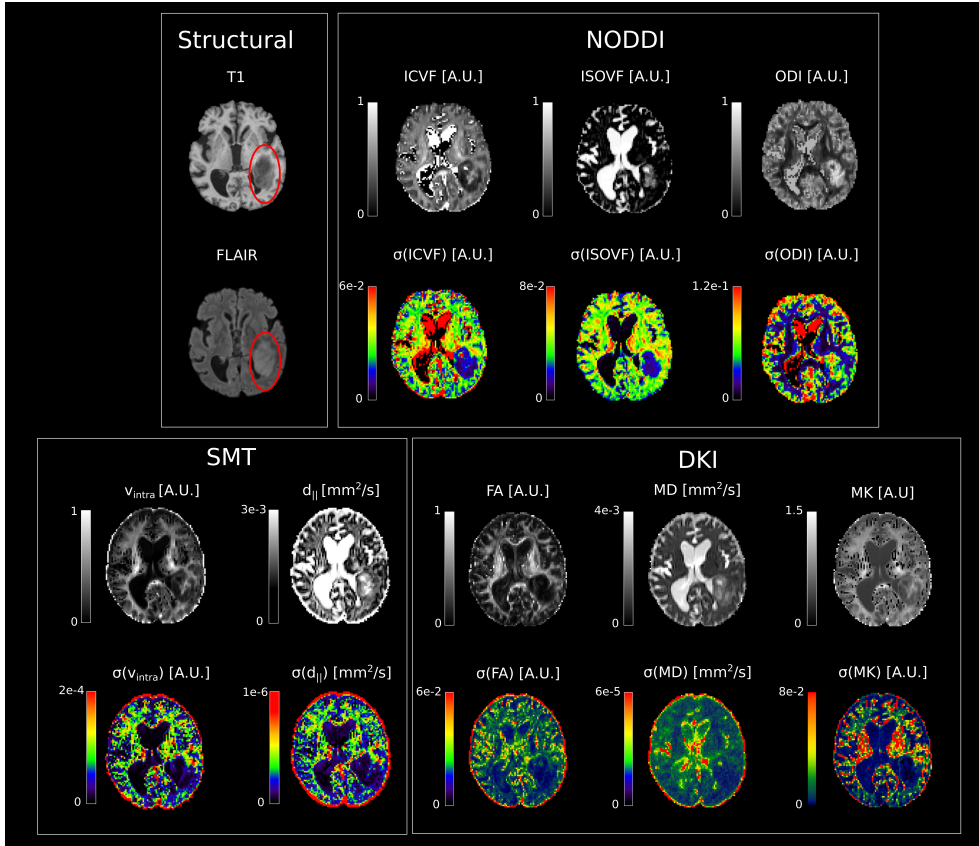
Figure 3.3: An axial slice from a representative patient showing its T1w and FLAIR structural images as well as both NODDI/SMT/DKI metrics (first row of each box, grey scale) along with their standard deviation map (second row, jet scale). NODDI = neurite orientation dispersion and density imaging, SMT = spherical mean technique, DKI = diffusion kurtosis imaging, ICVF = intracellular volume fraction, ISOVF = isotropic volume fraction, ODI = orientation dispersion index, FA = fractional anistropy, MD = mean diffusivity, MK = mean kurtosis.

deviations for all subjects in the dataset. While the single parameters show heterogeneous patterns between healthy and tumoral tissues and appear to have different discrimination power, their standard deviation does not dramatically differ. As seen in the previous figures, slight differences between tissues are still present, with a tendency of σ to be lower for oedema and tumours for most parameters. Overall, the general trend highlights however that estimation precision is stable both in healthy and pathological tissues. As this behaviour is common both to DKI and to the two microstructural models, it suggests the model-microstructure-mismatch does not significantly impair parameter estimation precision when fitting NODDI and SMT inside tumoral tissues.

Figure 3.1 shows the table with both the tissue specific mean RSS across
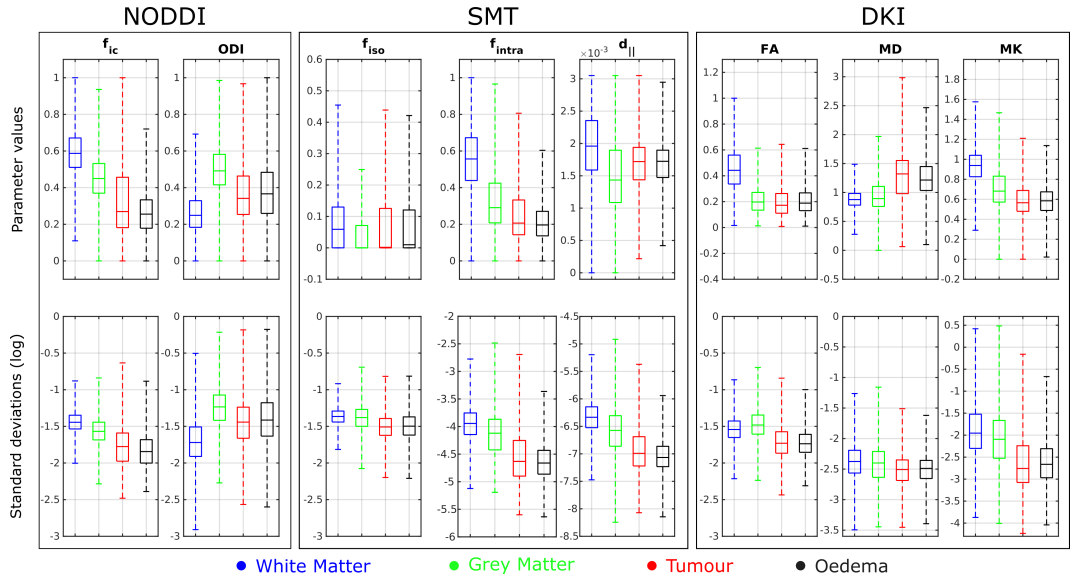
Figure 3.4: Boxplots for tissue-specific mean and standard deviations (logscale) of NODDI, SMT and DKI metrics coming from normal-appearing white matter in blue, grey matter in green, tumoral tissues in red and from the oedema region in black. NODDI = neurite orientation dispersion and density imaging, SMT = spherical mean technique, DKI = diffusion kurtosis imaging, ICVF = intracellular volume fraction, ISOVF = isotropic volume fraction, ODI = orientation dispersion index, FA = fractional anistropy, MD = mean diffusivity, MK = mean kurtosis.

all subjects for NODDI and the DKI, and its expected value given the appropriate noise model. As it was observed in the case of parameter precisions, it appears that the residuals from both techniques are not particularly affected by the pathological environment of the tumour and the oedema. The fitting performance seems unaltered in the general picture, with both techniques being fairly in agreement with the expected RSS given the estimation of the standard deviation of the noise. It is worth mentioning that, as the used estimators are different, it is difficult to draw any conclusions about an inter-model comparison of goodness-of-fit. Moreover, as the residuals of SMT model are uninformative due to the aforementioned reasons, the RSS was not computed.

3.3.2 Generalized sensitivity of the models

Figure 3.5 shows the GSF plots for the model parameters of NODDI, DKI and SMT, generated as explained in Section 3.2.2. Concerning the behaviour of single diffusion parameters, we can identify three different trends: A first set of parameters (f_{iso}, $d_{||}$ and the diffusion tensor components) gain their informational con-

	DKI log(RSS)				NODDI log(RSS)				Expected log(RSS)			
Subj	WM	GM	Tum	Oed	WM	GM	Tum	Oed	WM	GM	Tum	Oed
#01	3.678	3.792	3.718	3.869	4.129	4.037	3.858	4.139	4.063	4.328	4.272	4.411
#02	3.651	3.768	3.764	3.789	4.106	4.079	4.065	4.160	3.886	4.157	4.394	4.098
#03	3.615	3.061	3.769	3.688	4.061	3.987	4.356	4.168	3.887	4.096	4.139	4.044
#04	3.544	3.734	3.496	x	4.035	4.013	3.722	x	3.844	4.204	4.144	x
#05	3.713	3.875	3.775	3.842	4.185	4.104	4.046	4.222	4.043	4.412	4.347	4.515
#06	3.701	3.895	3.634	3.548	4.146	4.097	4.026	3.997	4.027	4.373	3.959	4.092
#07	3.577	3.405	3.632	x	4.096	3.914	4.063	x	3.830	3.985	3.901	x
#08	3.618	3.666	3.646	3.752	4.062	3.974	4.089	4.067	3.978	4.102	4.126	4.389
#09	3.571	3.754	3.649	3.818	4.021	4.010	4.115	4.182	3.914	4.304	4.028	4.523
#10	3.679	2.686	3.762	3.721	4.166	4.062	3.981	4.143	4.052	4.375	4.191	4.199
#11	3.538	3.172	3.752	3.625	4.119	4.020	4.132	4.198	3.753	3.940	4.328	4.057

Table 3.1: Mean residual sum of squares for each subject and tissue in the dataset. The set of columns to the right represents the expectations of the RSS, given the standard deviation of the noise affecting the diffusion signal. Results are reported in logarithmic scale (log10). Cells marked with "x" denote subjects for which no oedematous tissue was found in the lesion segmentation procedure. NODDI = neurite orientation dispersion and density imaging, SMT = spherical mean technique, DKI = diffusion kurtosis imaging, RSS = residual sum of squares.

tent in the b-values approaching $b = 1000s/mm^2$; a second set of parameters (f_{ic}, f_{intra} and the diffusion kurtosis tensor components) benefit from b-values starting from $b = 2500s/mm^2$ and a single parameter (Watson's distribution concentration parameter κ) steadily gains information across the entire studied b-value range, with no clear optimal interval. The general behaviour of the curves for every parameter does not significantly vary between tissues, identifying 0-1 rises which are relatively similar in WM, GM, oedema, and the tumour. This lack of difference in the sensitivity functions for the two microstructural models suggests the acquisition protocol employed in this study (designed for the healthy brain) features similar estimation precision in all tissues, and is therefore suitable inside the pathological region. As a last remark, significant over/undershoot from the 0-1 range for the GSFs reveals substantial correlations during the estimation process of same-model parameters, which in this case tends to be tissue dependent, as it will be discussed in the following section.

3.3.3 Investigating parameter correlations

Lastly, Figure 3.6 (a-d) shows the median correlation matrix across all subjects of the voxel-wise parameters from all models, computed for the four studied tissues. These matrices present significantly different features, supporting the hypothesis that the relationship between diffusion parameters change in dependence to the microstructure environment. However, we find some strong correlations, both positive and negative, which tend to be common in all four matrices. Figure 3.6
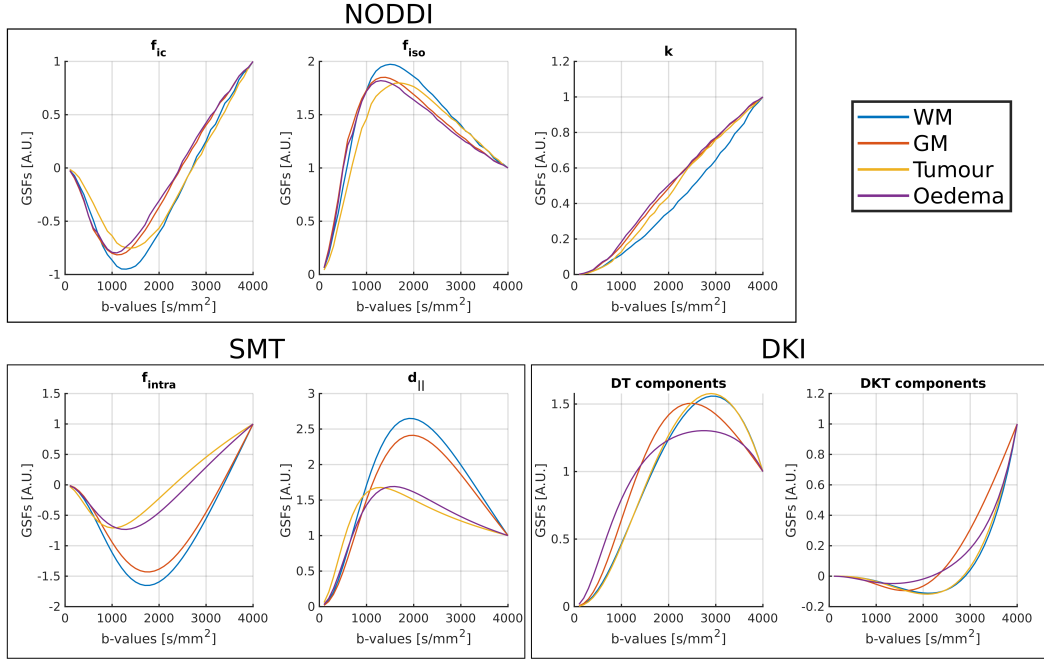
Figure 3.5: Generalized sensitivity equations for the NODDI, SMT and DKI generated with parameter values corresponding to voxels from white matter, grey matter and the tumoral tissues (tumour core and oedema). The DKI section contains the mean GSF for the parameters of the kurtosis-corrected diffusion tensor(DT components) and the mean GSFs across the parameters of the kurtosis tensor (DKT components). The interval for which we have the 0-1 transition marks the b-value range which is most informative for each of the model parameters. NODDI = neurite orientation dispersion and density imaging, SMT = spherical mean technique, DKI = diffusion kurtosis imaging, GSFs = generalized sensitivity functions, DT = diffusion tensor, DKT = diffusion kurtosis tensor.

(e) shows the redundancy matrix (RM). The occurrences in the RM reveal those couples of metrics which both feature high correlation (non-orthogonality of information) and are common to all tissue-specific matrices (poor tissue discrimination power). In particular, the AD, MD, and RD diffusivity metrics from DKI, ODI from NODDI and $d_{||}$ from the SMT appear to be strongly related, suggesting the entire inclusion of this subset of diffusion metrics in any data-driven procedure to be redundant. Similar considerations can be made about the MK-RK pair, for which the combined use is discouraged. All relationships highlighted by the RM were statistically significant in all subjects ($p < 10^{-28}$).
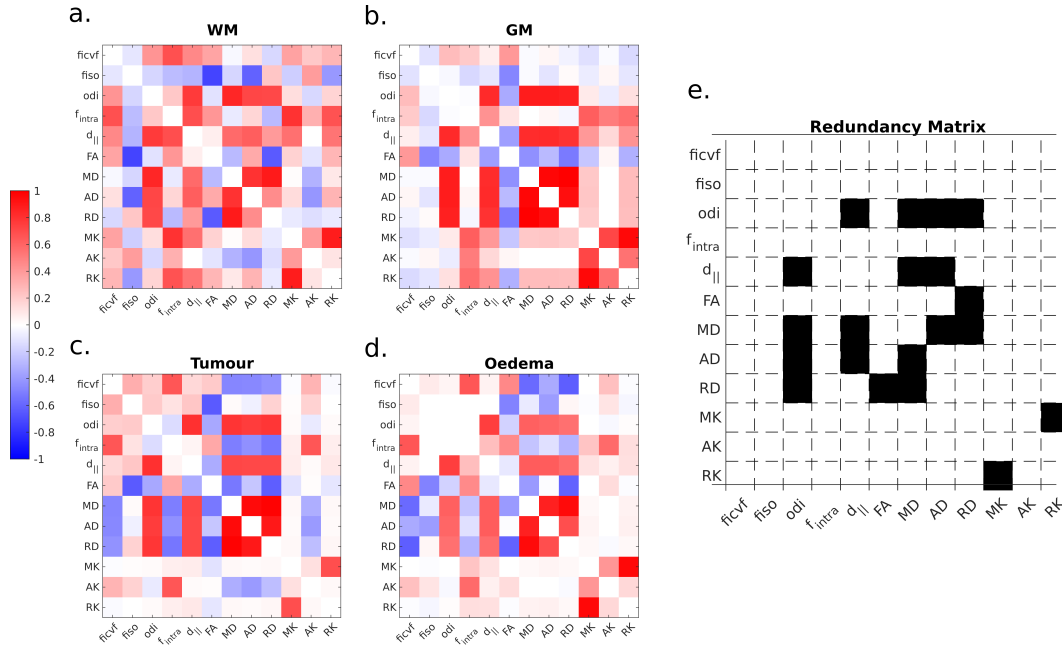
Figure 3.6: Figure 5: (a-d) Median voxel-wise correlation matrices for the computed diffusion metrics for all subjects in the dataset; (e) Metrics Redundancy Matrix, highlighting strong parameter correlations common to the structure of matrices a-d. For clarity of view, main diagonal values (trivially equal to 1) were identically put to zero. ficvf = intracellular volume fraction, fiso = isotropic volume fraction, ODI = orientation dispersion index, FA = fractional anisotropy, MD = mean diffusivity, MK = mean kurtosis, AK = axial kurtosis, RK = radial kurtosis.

3.4 Discussion and Conclusions

In this work, we explore the use of advanced diffusion models in tumours from the standpoint of goodness of fit and precision of their estimates. We refrained from giving explicit biophysical meaning to their parameters, due to the microstructure-model mismatch such choice features and concentrate on investigating their stability in the pathological tissues as signal representations. In doing so, we separately assessed their mathematical reliability in the tumoral lesion and in the normal appearing tissues. We questioned whether we would consistently find worse model residuals and less precise parameter estimates, as we thought the discrepancy between the tumour architecture and the biophysical formulation of the compartments would result in the inability to properly identify the model. We noticed, however, how the parameter estimation procedure is minimally impacted by the tissue-model mismatch, resulting for some cases in light trends of higher precision inside the tumoral tissues with respect to the normal-appearing brain.

This is most surprising when it comes to the intra-axonal compartments of both NODDI and SMT, where we feel the structural mismatch is most present. Highly anisotropic, 'stick-like', neuronal structures are mostly absent in tumours, yet the corresponding parameters are identified precisely and with a certain degree of spatial coherence. To our knowledge, the use of the stick diffusion model is known in tumour diffusion modelling. In fact, the Vascular, Extracellular, and Restricted Diffusion for Cytometry in Tumours (VERDICT-MRI) model for colorectal and prostate cancer (Eleftheria Panagiotaki et al., 2015; Eletheria Panagiotaki et al., 2014) employs isotropically dispersed sticks to describe pseudo-diffusion inside blood vessels. Nevertheless, this information comes from diffusion volumes at very low b-values ($b < 300s/mm^2$) (similarly to Intravoxel Incoherent Motion (IVIM) MRI (Le Bihan, Eric Breton, et al., 1986)), which are not acquired in typical HARDI datasets such as ours. It should be noted that, while the methodology used in this work is sound for comparing fitting results of the same model in healthy and pathological conditions, it is not appropriate for the comparison of different models. Indeed, DKI features consistently lower residuals than NODDI across tissues. However, as different estimators are used for the two techniques, lower RSS does not necessarily indicate that DKI performs better in the tumoral tissue. Moreover, the standard deviation of the measurement noise was estimated from the multiple b0 images acquired, thus disregarding possible contributions from varying b-value and gradient direction. Thus, we cannot establish if DKI is underestimating or NODDI is overestimating the noise level. It is interesting to notice how the SMT estimation leads to dramatically higher relative precision for the intracellular volume fraction with respect to NODDI (up to 3-4 orders of magnitude smaller values of σ). This observation however does not come completely unexpected, as the spherical mean signal is produced with a significant direction averaging procedure which comes with the benefit of suppressing the additive gaussian-like noise. Overall, we found significant evidence that the model-microstructure mismatch does not substantially affect the fitting performance of NODDI and the SMT in the tumoral lesion, as similar trends in the studied metrics are witnessed for the DKI signal representation. The information and novel contrast these parameter maps produce appears to be stable and may potentially be exploited by data driven approaches to analyse different microstructural environments. In this work, we give useful indications about which of the studied metrics provide information about tissues (pathological and healthy) which is non-collinear and investigate ways to discriminate those which are non-informative, in relation to their collective use. While model

identification appears to be optimal, we still advise to use additional caution to give a patho-physiological interpretation to single parameters when applying 'biophysical' models in tumours. Indeed, the comprehension of their mathematical structure, assumptions and limitations, is vital to make any biological inference. If proper validation in this pathological environment is not provided, NODDI and SMT remain geometrical models of diffusion, or signal representation, not specifically linked to any biological meaning. Probing the microstructural environment of brain tumours through diffusion imaging may yield useful biomarkers to monitor progression and treatment response, but there is still room for various improvements (Nilsson et al., 2018). Apart from the use of advanced models, the use of peculiar acquisition schemes may enrich the diffusion signal enough to move past the model identification degeneracies reported in recent literature (Jelescu, Veraart, et al., 2016; Dmitry S Novikov, Els Fieremans, et al., 2019), and more unconventional datasets acquired with multiple diffusion times (Eleftheria Panagiotaki et al., 2015) or 'B-tensor encoding' (Szczepankiewicz, Sjölund, et al., 2019) are recent signs that the research framework of dMRI pulse sequence design still has a lot to offer. While some interesting works about specifically modelling the diffusion in gliomas are recently starting to appear (T. Roberts et al., 2018; Zaccagna et al., 2019), this is an environment which is still largely unexplored. Until these novel methodologies gain trust and recognition, we hope our efforts here provided support to the cautious use of existing advanced diffusion techniques to investigate this pathological environment.

Chapter 4

Assessment of structural disconnections in gliomas: a comparison of indirect and direct approaches

4.1 Introduction

A richer depiction of the topological alterations caused by brain tumours on the structural connectome may lead to a better understanding of the complex network dysfunctions the pathology causes, (Sporns, 2011; Castellano et al., 2017) and could identify cortical regions and WM bundles to be carefully navigated during surgery (Duffau, 2019). Techniques which identify and quantify the extent of WM damage beyond the location of a focal lesion have recently been gaining popularity in the field of stroke, as they tend to explain functional alterations better than damage to specific grey matter regions (Griffis et al., 2019; Salvalaggio et al., 2020; Schotten et al., 2020; Di Vita et al., 2019). Translating the use of such techniques in the oncological field requires, however, additional cares as the neoplastic nature of tumours poses some difficult challenges to the investigation of the alteration of WM tracts. Indeed, gliomas do not represent a focal and acute lesion but rather a slowly evolving infiltrative process. When studying the course of WM pathways through imaging, diffusion MRI is the instrument of choice, as it allows to extract the state and directional information of WM fibres through modelling the random motion of water molecules occurring in the different brain regions. Through dMRI, patterns of WM structural disconnections can be derived

exploiting so-called indirect or direct approaches:

- Indirect approaches bypass the need of a subject specific dMRI dataset by projecting the tumoral lesion of a given patient onto a tract-based atlas to detect which WM pathways are most likely to be affected by the pathology (Foulon et al., 2018). Although indirect methods may be more readily accessible, they currently generalize the glioma to be one lesioned region causing homogeneous effects on WM pathways. In this way, the high heterogeneity of the underlying pathological tissues (i.e., oedema, necrosis, tumoral core comprising different cell dimensions and cellularity) and their specific effects on axonal bundles is completely disregarded.

- Direct approaches involve the quantification of the brain connectome through tractography algorithms applied on dMRI data. Such methodologies are known to have their own limitations and pitfalls (Jeurissen, Descoteaux, et al., 2019) but, contrary to indirect approaches, have the undisputed advantage of providing subject-specific quantification of WM bundles.

Given the intrinsic difference between direct and indirect approaches, the aim of this study is to propose a quantitative comparison between them. We apply simple but effective image analyses to evaluate benefits and criticalities of both, highlighting points of agreement and divergence in terms of WM disconnection information that can be derived. Moreover, as the oedematous tissue appears to play a crucial role in defining tissutal regions which are subject to inflammation, favourable pathways for tumour spreading, we additionally investigate how patterns of structural disconnections are quantified when the oedematous tissue is included in the definition of pathological lesions.

4.2 Material and methods

Forty-four patients suffering from de novo brain tumours have been recruited and acquired at the University Hospital of Padova from July 2017 to March 2021. All procedures were in accordance with the ethical standards of the institutional research committee and with the 1964 Helsinki declaration plus later amendments. All participants provided informed, written consent in accordance with the local University Hospital Institutional Review Board. Figure 4.1 shows a comprehensive overview of the analyses introduced in this section.
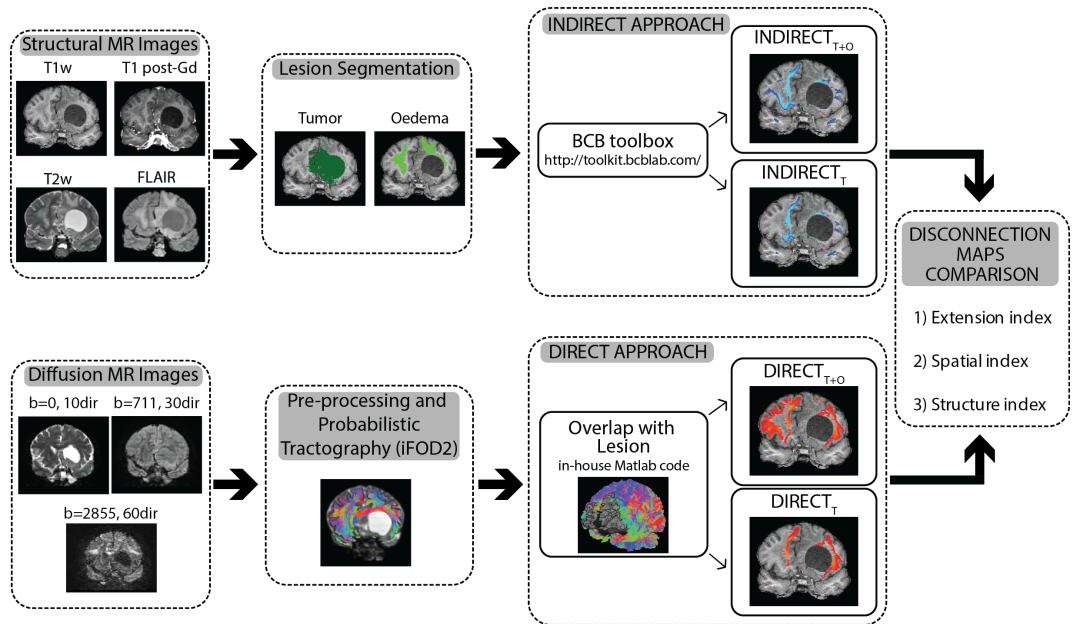
Figure 4.1: Visualisation of the processing pipeline which led to the computation of the four structural disconnection maps (upper row: indirect approach; lower row: direct approach) which were eventually compared. b-values are shown in s/mm^2. T = Tumour, T+O = Tumour+Oedema, iFOD2 = Second-order Integration over Fiber Orientation Distributions, Gd = Gadolinium, FLAIR = Fluid Attenuated Inversion Recovery

4.2.1 MRI acquisition

44 patients suffering from de novo brain tumours have been scanned at the University Hospital of Padova. The acquisition details were identical to those written in Chapter 3.

4.2.2 Tumour segmentation and structural pre-processing

Structural pre-processing of T1w, T2w and FLAIR scans and tissue segmentation details are given in Chapter 2. Employing structural images, two masks were manually delineated through the ITK-SNAP software (http://www.itksnap.org/) by an expert neuroradiologist with more than five years of experience. The first mask, labelled T, included the tumour core (contrast agent enhancing and non-enhancing regions) and the necrosis, where present. The second mask, labelled $T+O$, was created by adding the oedema area to the T mask. In addition, each tumour was labelled by the same neuroradiologist as left, right or bilateral according to the location of its core and to the mainly involved hemisphere. For each patient, the T and $T+O$ masks were mapped into the MNI152 space exploiting

the estimated diffeomorphic non-linear transformations. Finally, since direct and indirect disconnection mapping methods differ in the tracking of potential disconnections within subcortical areas, for each patient, we used the AAL3 atlas (Rolls et al., 2020) to segment the following regions: thalamus, caudates, putamen, pallidum, and hippocampus. Such areas were eventually discarded (i.e. masked out of all StrD maps) not to bias the subsequent methods' comparison.

4.2.3   Disconnection maps computation

Direct disconnection maps computation

Diffusion MRI Pre-processing   The acquired diffusion weighted volumes were visually inspected to identify and remove those images affected by interslice instabilities (Jacques-Donald Tournier et al., 2011) which were deemed excessively corrupted for subsequent pre-processing techniques to correct. Among all patients, 5 were discarded due to severely motion corrupted structural images, which prevented us to reliably perform structural pre-processing and tumour segmentation. 2 patients were additionally excluded from the study as their diffusion images presented within-volume motion artefacts on more than 10% of the total number of DWI volumes. Finally, for the remaining 44 patients, on average 3.3 volumes were discarded and in 20 out 44 patients no volume was removed. The rest of the pre-processing was executed in its entirety within the MRtrix3 Software (J-Donald Tournier, R. Smith, et al., 2019) and featured an initial denoising step based on random matrix theory (Veraart, Dmitry S Novikov, et al., 2016), with a subsequent call to the tools *topup* and *EDDY* (Andersson, Skare, et al., 2003; Andersson and Sotiropoulos, 2016) from FSL for B0 inhomogeneity, eddy current and motion joint correction. T1w segmentation results (including GM, subcortical parcellation, lesion and tumour masks) were registered to the naïve b0 volume using ANTs, by applying an affine transformation previously estimated on the patient's naïve T1w image.

Diffusion tractography specifications   The patient structural connectome reconstruction was performed in its entirety within the MRtrix3 software. We firstly performed multi-shell multi-tissue spherical deconvolution (Jeurissen, Jacques-Donald Tournier, et al., 2014) to recover the orientation distribution functions for each voxel. Subsequently, we computed the structural connectome by employing Anatomically Constrained Tractography (R. E. Smith et al., 2012), tracking individual fibres with a second-order Integration over Fiber Orientation Distributions

algorithm (J. D. Tournier et al., 2010). Standard streamline termination criteria values were used. The number of generated streamlines for each patient initially amounted to 100 millions, which were quantitatively reduced to 10 millions via the Spherical-deconvolution Informed Filtering of Tractograms (SIFT) framework (R. E. Smith et al., 2013).

Disconnection Maps Computation For each patient, following the quantification of the diffusion tractogram, we computed the patterns of structural disconnections by taking the two following steps:

1. We computed the subset of the streamlines in the tractogram that featured an overlap with the tumoral lesion (respectively, with T and, after, with $T+O$ masks).

2. In the dMRI space (i.e., the native space of the tractogram), we computed how many altered streamlines (the subset in step 1) were passing through each voxel of the brain. We labelled direct structural disconnection (dStrD) maps these voxel-wise frequency maps.

We used in-house MATLAB (ver. 2020b, The Mathworks, Natick, MA) scripts to perform the creation of the dStrD maps. As further volumetric analyses of dStrD maps required their binarization, the definition of a threshold to define significant disconnection was necessary. We defined such threshold with the following procedure:

1. Similarly to the dStrD map quantification, we computed for each subject in the dMRI space a voxel-wise streamline density map, this time considering the entirety of the tractogram.

2. We brought the individual streamline density maps to the MNI152 space via the previously estimated diffeomorphic transformations.

3. In the common MNI152 space, we computed the population average of the individual maps, omitting the lesioned ROI on a patient-by patient basis.

4. To balance the presence of a higher number of patients with left tumours, we symmetrised the frequency template by flipping (left-right) the obtained map, summing the flipped and non-flipped maps and dividing by two.

5. Using the same transform as in 2, we projected back the population-averaged streamline density map to the T1w space of each subject. We referred this resulting map as AvgDensity.

6. Finally, we considered the structural disconnection value of voxel with co-ordinates (x,y,z) as significant if the following criterion was met:

$$dStrD(x, y, z)/AvgDensity(x, y, z) > 10\% \qquad (4.1)$$

Additional investigations were performed also using more stringent and permissive thresholds.

Hence for each patient we obtained a mask of significantly disconnected voxels.

Indirect Disconnection Maps Computation

Indirect structural disconnection (iStrD) maps were quantified with the BCB Toolkit v. 4.2 (Foulon et al., 2018; Schotten et al., 2020). In choosing which healthy controls tractography atlas to use within the toolbox, we opted for the extended diffusion dataset provided by the toolkit authors, for which the structural connectome of 180 healthy controls from the Human Connectome Project 7T dataset was quantified (full tractography specification in (Thiebaut de Schotten, Urbanski, et al., 2017)). In summary, using the BCB Toolkit, for each patient, the lesion masks (both T and $T+O$) in the MNI152 space were registered to each control naïve space using affine and diffeomorphic transformations and subsequently used as seed for the tractography in TrackVis (http://trackvis.org). Tractographies from the lesions were transformed in visitation maps, binarized and brought to the MNI152. Finally, the percentage overlap map was computed by summing at each point in the MNI152 space the normalized visitation map of each healthy subject. Hence, in the resulting disconnection map (i.e., iStrD), the value in each voxel considers the tracts' interindividual variability and indicate a probability of disconnection from 0 to 100% for the given lesion. As no ad-hoc studies are available regarding the recommended use of iStrD maps in tumours, we set the probabilistic threshold to 0.5 as in the software defaults settings. Additional investigations were performed also using more stringent and permissive thresholds (i.e., 0.7 and 0.3 respectively).

4.2.4 Metrics of comparison

Having obtained a total of four different structural disconnection (StrD) maps (i.e., two for each methodology, different in terms of the employed input mask: T and $T+O$), we wanted to compare them both *intra-methodology* (i.e., same

approach, T versus $T+O$ maps) and *inter-methodology* (i.e., same lesion mask, direct versus indirect maps).

The framework we employed for their comparison had three simple metrics, useful to quantify different similarity features:

- **The difference in volume (ΔVol)**: This metric allowed us to quantify the difference in the extension of alteration which is detected by two disconnection maps.

- **The Dice Similarity index (*Dice*)**: The Sørensen-Dice similarity index is a well-known metric of comparison between digital images and is defined by the following formula:

$$Dice = \frac{2(A \cap B)}{|A| + |B|} \tag{4.2}$$

  where A, B are the two binary matrices for which the similarity needs to be tested. The Dice index quantifies how similar the shape of structural alterations is between two different approaches.

- **The correlation at the intersection (*Corr*)**: We computed the Pearson correlation in a region of interest defined by the intersection of the two matrices in exam. Unlike the Dice index which evaluates only the similarity between shapes, the correlation analysis considers where the hotspots of alteration are in the two StrD maps, and measures their spatial agreement.

  While the ΔVol and *Dice* metrics were calculated using the binarized disconnection maps, the Corr index was computed using the thresholded StrD maps. Additionally, ΔVol and *Dice* were computed both considering the entire disconnection maps and subdividing them into their ipsilateral and contralateral components (bilateral tumours were excluded from this last analysis).

To summarise the obtained indices, we computed the median value and the 25th / 75th percentiles across all subjects for each metric of comparison.

4.2.5 Statistical analysis

To test for statistically significant differences in ΔVol, both considering whole brain results and ipsi-/contralateral hemisphere separately, a Wilcoxon rank sum test (significance level $\alpha = 0.05$) was employed.

To assess whether there was a linear relationship between the comparison metrics and the extension of the input mask, we performed a correlation analysis (Spearman Correlation, significance level $\alpha = 0.05$) between the three indices (i.e. ΔVol, $Dice$ and $Corr$) and the volume of the input mask, separately for T and $T + O$ masks. To test the sensitivity of the comparison metrics to the set of thresholds used for the dStrD/iStrD maps, we defined their normalized range of variation (nRV) as:

$$nRV(k) = 100 * \frac{|max(k(t_{iStrD}, t_{dStrD})) - min(k(t_{iStrD}, t_{dStrD}))|}{max(k(t_{iStrD}, t_{dStrD}))} \qquad (4.3)$$

where $k(t_{iStrD}, t_{dStrD}))$ is the median value across the dataset of the comparison metric between two StrD maps, given the indirect (t_{iStrD}) and direct (t_{dStrD}) thresholds. The investigated thresholds values were $t_{dStrD} = [5\%, 10\%, 15\%, 20\%, 25\%]$ and $t_{iStrD} = [0.3, 0.5, 0.7]$.

To assess whether there was a relationship between the comparison metrics and the extension of the input mask, we performed a correlation analysis (Spearman Correlation, significance level 0.05) between ΔVol, $Dice$ and $Corr$ and the volume of the input mask, separately T and $T + O$ masks. Scatterplots of such analyses were generated to visually inspect the investigated relationships. Additionally the Simple Moving Average (SMA, 7 points, centerer window) was computed to support the interpretation of possible trends.

4.3 Results

Patients' main demographic and clinical information are summarized in Table 4.1.

Overall, according to 2021 World Health Organization classification of tumours of the central nervous system (Louis, Perry, Wesseling, et al., 2021), 33 patients had a glioblastoma, 1 had an astrocytoma, 3 had a glioneuronal and neuronal tumours, 1 had an oligodendroglioma, 1 had a primary diffuse large B-cell lymphoma, 2 had other types of brain tumour (1 intracranial mesenchymal tumour and 1 non-otherwise specified tumour) and 3 had an unclassifiable brain tumour, as they deceased shortly before the surgery or did not underwent neurosurgery. The extent of the $T + O$ mask ranged between 5.7 and 191.6 cm^3 (mean value 65.1 cm^3, std 50.4cm^3), whereas the extent of the T mask between 0.4 and 155.9 cm^3 (mean value 46.5, std 39.1 cm^3). Figure 4.2 shows the frequency maps

Age(y)		59.9 ± 14.6
Gender		
	female(n)	20
	male(n)	24
Tumour Histology		
	Astrocytoma (n)	1
	Glioblastoma (n)	33
	Glioneuronal and neuronal tumours (n)	3
	Astrocytoma (n)	1
	Oligodendroglioma (n)	1
	Primary diffuse large B-cell lymphoma (n)	1
	Other (n)	2
	n.a. (n)	3
Tumour Grade		
	Low (n)	5
	High (n)	36
	n.a. (n)	3
IDH-1 Mutation Status		
	Wild Type (n)	29
	Mutated (n)	5
	n.a. (n)	10
Tumour Site		
	Left (n)	22
	Right (n)	17
	Bilateral (n)	5

Table 4.1: Patient's main demographic and clinical information for the cohort of subjects included in this study. n.a.= not available.

of the lesions in the patient population. The two reported maps refer to the T (first two rows) and to the $T+O$ masks (second two rows). The distribution is sparse with tumours involving predominantly the right frontal and temporal lobes, with a low spatial overlap (maximum value 17.8% of patients for the T mask, and 22.2% of patients for the $T+O$ mask).

Figure 4.3 shows an example of disconnection maps for two representative subjects in our dataset. In panel A we can clearly see that the dStrD map is able to detect the displacement of axonal fibres in the brain due to the tumoral mass (most apparent in the axial and coronal views). This effect is not detectable by the indirect approach, which inevitably leads to key differences between methodologies ($\Delta Vol(iStrD_{T+O}, dStrDT+O) = -28.05cm^3$; $\Delta Vol(iStrD_T, dStrD_T) = -4.8cm^3$; $Dice(iStrD_{T+O}, dStrD_{T+O}) = 0.51$; $Dice(iStrD_T, dStrD_T) = 0.51$; $Corr(iStrD_{T+O}, dStrD_{T+O}$
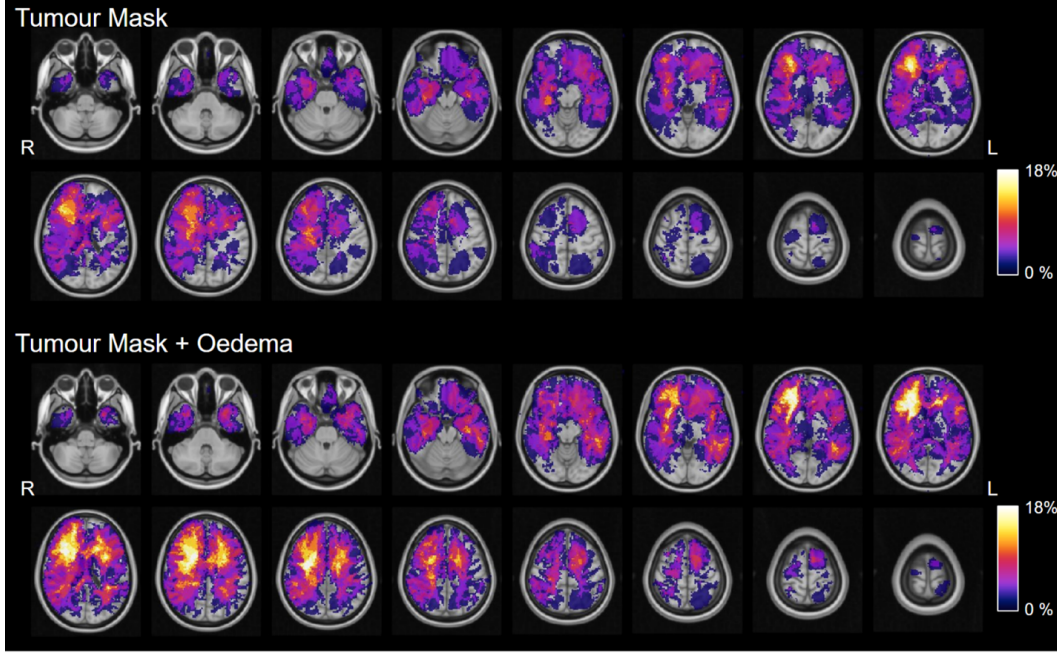
Figure 4.2: Frequency maps of tumoral lesions in our cohort of patients. In the two upper rows, the lesion was composed by the tumoral core (both enhancing and non-enhancing, and necrotic regions). In the two lower rows, the tumoral lesion mask was composed by the tumour core and the oedematous tissue.

$) = 0.45$; $Corr(iStrD_T, dStrD_T) = 0.43$). While the displacement of fibres is less visually appreciable in panel B, differences between approaches are still present ($\Delta Vol(iStrD_{T+O}, dStrD_{T+O}) = -21.1cm^3$; $\Delta Vol(iStrD_T, dStrD_T) = -4.1cm^3$; $Dice(iStrD_{T+O}, dStrD_{T+O}) = 0.59$; $Dice(iStrD_T, dStrD_T) = 0.51$; $Corr(iStrD_{T+O}, dStrD_{T+O}) = 0.41$; $Corr(iStrD_T, dStrD_T) = 0.33$). Looking at the StrD maps intra-methodology, i.e., comparing between T and $T+O$ maps, the difference is less self-evident and, apart from a few areas where $T+O$ maps show more extensive structural disconnections, we find analogous behaviours and morphological features. While ΔVol remains high, suggesting the presence of volumetric differences between the maps, this is well reflected by the $Dice$ and $Corr$ metrics being sensibly higher, both in A. ($\Delta Vol(dStrD_{T+O}, dStrD_T) = 25cm^3$; $\Delta Vol(iStrD_{T+O}, iStrD_T) = 15.17cm^3$; $Dice(dStrD_{T+O}, dStrD_T) = 0.74$; $Dice(iStrD_{T+O}, iStrD_T) = 0.84$; $Corr(dStrD_{T+O}, dStrD_T) = 0.79$; $Corr(iStrD_{T+O}, iStrD_T) = 0.89$) and in B. ($\Delta Vol(dStrD_{T+O}, dStrD_T) = 39.36cm^3$; $\Delta Vol(iStrD_{T+O}, iStrD_T) = 22.40cm^3$; $Dice(dStrD_{T+O}, dStrD_T) = 0.75$; $Dice(iStrD_{T+O}, iStrD_T) = 0.85$; $Corr(dStrD_{T+O}, dStrD_T) = 0.92$; $Corr(iStrD_{T+O}, iStrD_T) = 0.86$).

Generalizing Figure 4.3 results, Table 4.2 shows the metrics employed for the
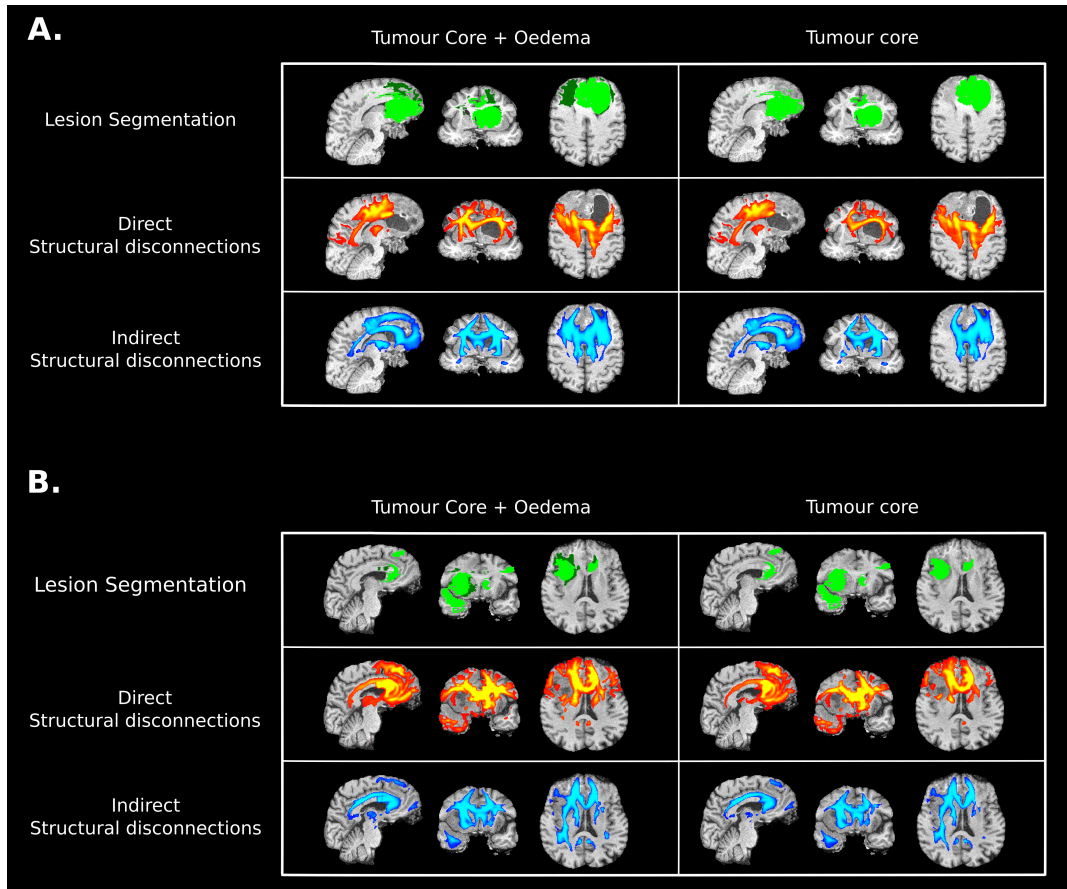
Figure 4.3: Lesion segmentation (dark green = oedema, green=tumour core), iStrD (blue/light-blue) and dStrD (red/yellow) maps overlayed on the T1w image for two representative subjects from our cohorts of patients. In the StrD maps, the lighter the colour is, the higher the probability/severity of WM disconnection. iStrD = indirect structural disconnection, dStrD = direct structural disconnection.

comparison in the entire dataset and reports their median and their $25_{th}/75_{th}$ percentiles. Comparing intra-method results, as expected, we obtained a positive ΔVol which means that the volume of disconnection increased when $T+O$ is used as input mask (mainly in the whole brain analysis and in the ipsilateral hemisphere). In addition, we obtained a good agreement between the compared maps highlighted both by $Dice$ and by $Corr$ indices, suggesting that in both cases analogous spatial patterns of disconnection were detected. On the other hand, the inter-method comparison revealed that: 1) the detected volume of disconnection is significantly lower at the whole-brain and ipsilateral level for the indirect method when the $T+O$ mask is used (p-value respectively of 0.005 at whole brain, 0.0008 at ipsilateral level); 2) overall there is a decrease in the agreement of the

		COMPARISON OF INTRA-METHOD DISCONNECTION MAPS		COMPARISON OF INTER-METHOD DISCONNECTION MAPS	
		INDIRECT_{T+O} INDIRECT_T	DIRECT_{T+O} DIRECT_T	INDIRECT_{T+O} DIRECT_{T+O}	INDIRECT_T DIRECT_T
EXTENSION index	ΔVOL (cm³)	9.17 [0.08 29.4]	27.4 [0.11 61.3]	-25.1 [-46.2 -12.3]	-0.97 [-21.4 8.1]
EXTENSION index	ΔVOL IPSILATERAL (cm³)	5.55 [0.07 19.6]	20.2 [0.05 50.3]	-21.2 [-33.3 -10.3]	-0.43 [-16 6.3]
EXTENSION index	ΔVOL CONTRALATERAL (cm³)	2.31 [0 7.63]	2.16 [0 9.83]	-1.76 [-11.1 0.62]	-0.18 [-4.64 1.58]
SPATIAL index	DICE	0.9 [0.62 1]	0.83 [0.39 1]	0.57 [0.52 0.59]	0.46 [0.37 0.57]
SPATIAL index	DICE IPSILATERAL	0.9 [0.70 1]	0.85 [0.46 1]	0.57 [0.51 0.6]	0.46 [0.35 0.59]
SPATIAL index	DICE CONTRALATERAL	0.86 [0.42 1]	0.88 [0.17 1]	0.53 [0.35 0.61]	0.44 [0 0.59]
STRUCTURE index	CORRELATION in the intersection	0.91 [0.74 1]	0.87 [0.72 1]	0.45 [0.39 0.50]	0.39 [0.32 0.48]

Table 4.2: median values (with 25th and 75th percentiles in squared brackets) for the similarity metrics computed across the patient cohort. Each column represents a comparison between two specific StrD maps (e.g., the first column is the intra-methodology comparison between the StrD maps generated with the T and $T+O$ lesion masks). For further specificity, we additionally divided the analysis of the *Dice* and ΔVol indices in the hemispheres ipsilateral and contralateral to the presence of the tumour. iStrD = indirect structural disconnection, dStrD = direct structural disconnection, T = tumour, T+O = tumour + oedema.

disconnection location (whole brain, ipsilateral and contralateral) with a median *Dice* value of 0.57; 3) there is a poor agreement of the disconnection pattern with a median *Corr* value of 0.45 and 0.39 respectively for the T and $T+O$ input masks.

Figure 4.4 shows the sensitivity of the median of the computed metrics across the dataset to a set of possible thresholds. Considering inter-methodology comparisons (green-stars and red triangles in the figure), we found the ΔVol index to be the most variable across the tested thresholds ($nRV_{T+O}(\Delta Vol) = 280.34\%$, $nRV_T(\Delta Vol) = 210.34\%$). Morphology similarities were more consistent ($nRV_{T+O}(Dice) = 35.58\%$, $nRV_T(Dice) = 29.53\%$), as well as the agreement of hotspot locations ($nRV_{T+O}(Corr) = 26.58\%$, $nRV_T(Corr) = 31.32\%$). Shifting to intra-methodology comparisons (blue circles and purple squares in
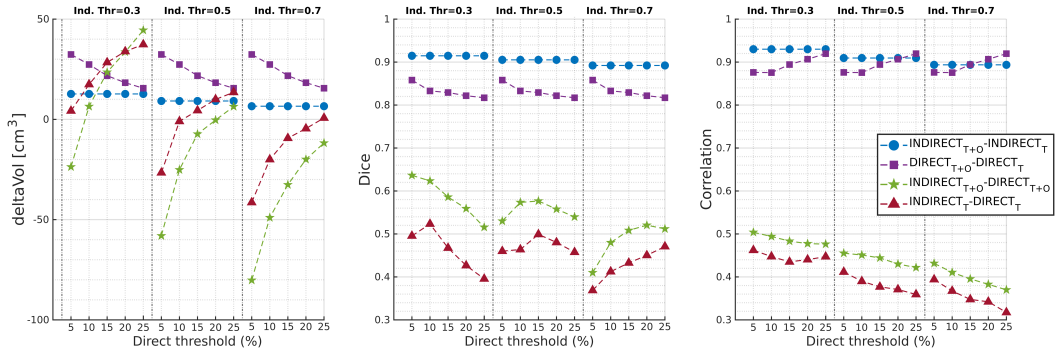
Figure 4.4: Sensitivity to iStrD/dStrD thresholds for the similarity metrics in inter- and intra-methodology comparisons. Individual points of the same shape and colour (e.g., green stars, representing the inter-methodology comparison of T+O maps) are the median values across the dataset for the given index, computed with a different pair of dStrD/iStrD thresholds. iStrD = indirect structural disconnection, dStrD = direct structural disconnection, T = tumour, T+O = tumour + oedema.

the figure), as expected, we found a more stable situation. Again, volumetric measures were the most variable across thresholds ($nRV_{T+O}(\Delta Vol) = 52\%$, $nRV_T(\Delta Vol) = 48.24\%$), and an even higher consistency was found considering the Dice ($nRV_{T+O}(Dice) = 4.79\%$, $nRV_T(Dice) = 2.45\%$), and Corr indices ($nRV_{T+O}(Corr) = 4.79\%$, $nRV_T(Corr) = 3.91\%$).

Lastly, Figure 4.5 shows the scatterplot between the extension of the cancerous lesion (both considering only the tumour core and including the oedema) and the similarity metrics. Statistically significant relationships were found for the Dice coefficient ($r_T = 0.42$, $p_T = 0.004$, $r_{T+O} = 0.55$ $p_{T+O} = 9.5e - 05$) and for ΔVol ($r_T = 0.33 p_T = 0.03$). Nevertheless, the simple moving average showed that all three relationships were highly non-linear and heavily influenced by a limited number of small tumours. Indeed, when lesions were larger than 50 cm^3, the linear trend disappeared due to heavy saturation, leading to no major evidence that the size of the lesion plays a fundamental role in the similarity of direct and indirect structural disconnection maps.

4.4 Discussion and Conclusions

Throughout the recent years, several warnings have been raised against the use of indirect approaches to investigate the disruption of structural connectivity in neoplastic pathologies, as physio-pathological phenomena such as tissue displacement (Clark et al., 2003) or transneuronal degeneration (Fornito et al., 2015)
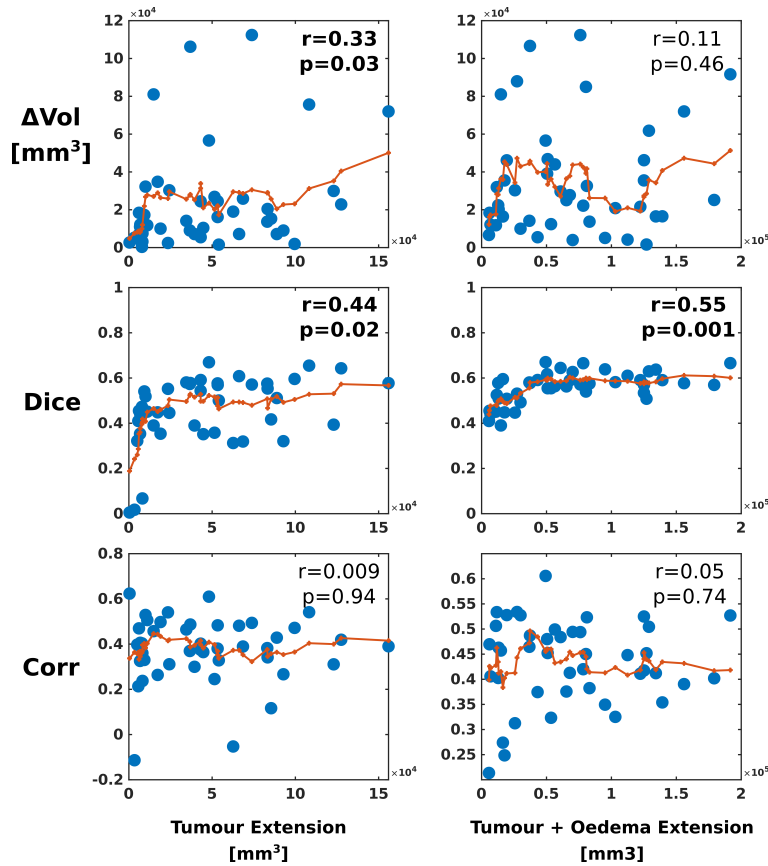
Figure 4.5: Scatterplots of tumour/lesion size and the similarity measures. The simple moving average is superimposed in red to highlight the trend of the relationships.

cannot be considered by atlas-based methodologies. On the other hand, diffusion tractography techniques may enable us to quantify these effects in a subject-wise manner. The framework of analysis we introduced in this article allowed us to systematically compare patterns of WM disconnections and quantitatively point out the difference between methodologies. Thus, we here investigated the difference between direct and indirect approaches to quantify patterns of WM disconnections in subjects suffering from brain tumours. The quantitative comparison of the investigated structural disconnection maps included the evaluation of the difference of their overall volume, the Dice index to evaluate their shape similarities, and finally a correlation analysis aimed to investigate if hotspots of disconnections were identified accordingly. We performed these analyses both by defining the cancerous lesion as the tumour core, and by including the oedematous tissue in the lesion segmentation. In this way, we could additionally analyse the impact of the oedema in the computation of StrD maps within the same

methodology. We found that in terms of volumetric extension of the disconnections, the inclusion of the oedema in the tumoral lesion had a higher impact on direct methodologies w.r.t. indirect ones, as disconnection volume increased more extensively in the former case. This increase occurred particularly in the hemisphere ipsilateral to the tumour, where fibres are most likely to intersect the tumoral lesion. Contralateral fibres, on the other hand, are less likely to intersect the tumoral lesion and the detection of their alterations did not appear to be influenced as much by the oedema. In general, the inclusion of the oedema appeared to drastically alter the extension of ipsilateral patterns of disconnections but did not severely impact the detection of contralateral alteration. For what concerns the spatial similarity between the investigated maps, the Dice coefficient revealed good intra-methodology agreement, with both direct/indirect maps featuring high values when testing the difference in terms of inclusion of the oedema in the tumoral lesion. When comparing direct and indirect methodologies however, the Dice coefficient showed lower values indicating a substantial mismatch between the structural disconnection patterns. Such differences remained consistent even when we considered ipsilateral and contralateral hemispheres separately. Dice values for inter- and intra- methodology maps were well reflected by the *Corr* index, which revealed whether the localization of hotspots of alterations was concordant between structural disconnection maps. As expected, intra-methodology correlations were strong, with hotspots of alterations having the same spatial location. When we investigated inter-methodology relationships, however, such correspondence was lost, regardless if the oedema was included or excluded in the analysis. Overall, these differences lead us to think that the impact of the inclusion of the oedema in the tumoral lesion has a minor impact than varying between direct/indirect approaches. However, the effect of such choice is still non-negligible and produces sensible changes in the structural disconnection patterns that can be observed. We initially hypothesized that the size of the tumour would play a pivotal role in the similarity between the patterns of disconnections. However, no significant linear relationship was found between the studied metrics and the tumoral lesion extension. The sensitivity analysis to the thresholds for indirect and direct disconnection maps revealed that volumetric indices are moderately dependent on such choice, potentially altering the interpretation of its results.

We are aware there are some limitations to our work. First and foremost, the structural disconnection maps must be thresholded to make any inference regarding the volume and shape of the detected disconnections. This choice is

non-trivial, and while there are some literature indications (although not specifically in tumour cases) for indirect methodologies (Thiebaut de Schotten, Flavio Dell'Acqua, et al., 2015), thresholding tractograms is an open question in the field of dMRI (C.-H. Yeh et al., 2021). Volumetric measures of disconnection were significantly impacted by threshold choice, whereas the *Dice* and *Corr* indices were less affected. These observations lead us to raise a warning on the use of volumetric measures when relating structural disconnection features to other quantities of clinical interest. As a second limitation, there are differences in place between the streamline reconstruction of the tract-based atlas of the BCB toolkit and of the patients belonging to our dataset. While using the same tractography algorithm in both methodologies would indeed eliminate the variability in results due to the different tracking, the purpose of this study was to use the indirect disconnection tools "as is", and to compare such results with state-of-the-art tracking techniques. Moreover, "voxellizing" the streamlines to the disconnection maps arguably reduces the variability due to diffusion orientation sampling and streamline shapes. Thus, we believe this discretization step highlights in the final StrD maps those differences between the two approaches which are mainly due to dominant physio-pathological effects rather than fibre reconstruction intricacies. As a last note, few studies have shown that the presence of a tumoral lesion may cause Wallerian degeneration to take place in the surrounding area and at distance from its location (Saksena et al., 2013; Lahrmann et al., 2005; Sawlani et al., 1997). This physio-pathological process represents the inflammatory response of the nervous system to an axonal injury and may significantly impair the permeability of axons in those regions (Pierpaoli et al., 2001), limiting the possibility for tractography algorithms to robustly reconstruct the associated streamlines. Depending on the severity of the degeneration, such WM regions may not be visible to direct approaches, which would consequently fail to detect sites of ongoing pathological alteration. In conclusion, with our work we presented evidence that direct and indirect approaches offer two different pictures of structural disconnections in patients affected by brain tumours. Given these differences, we advise that whenever mass displacement effects appear to be present, direct methodologies should be preferred as they are better suited to account for these morphological and pathological variations. Nevertheless, assessing structural disconnection maps' predictive value of biological/cognitive progression of glioma patients is vital to addressing the clinical relevance of these techniques. Thus, further studies are needed to answer these unmet demands.

Chapter 5

Structurally altered white matter connections underlie regional grey matter metabolism changes in brain tumour patients

5.1 Introduction

Diffusion MRI, with its intrinsic link to microstructural features of brain tissues, has been proven over the years to hold diagnostic and prognostic value in brain tumours, characterizing their heterogeneity (C. Li, S. Wang, Yan, Piper, et al., 2019), evaluating aggressiveness (C. Li, S. Wang, Yan, Torheim, et al., 2019) and differentiating between different grades (Maekawa et al., 2020). The value of dMRI is however not limited to investigating the tumoral focal lesion, but extends to detecting overall systemic abnormalites.

Structural brain networks can be effectively represented by structural connectivity matrices. These mathematical entities contain the amount of connectivity between each pair of nodes of a given brain parcellation. Quantifying region-region connectivity usually involves analyzing the streamlines which connect them, and extracting measures such as their number, their length or average FA/MD along their path.

Indeed, dMRI-based structural connectomes have become a widespread tool for the investigation of white matter connections of the human brain (C.-H. Yeh et al., 2021). It has in fact widely been shown that graph analysis related to structural networks is able characterize different pathologies (Crossley et al., 2014). As

such, there has been a recent interest in the state-of the art literature to capture possible changes in the structural organization of the human brain in presence of a complex disease such as brain tumours.

Evidence of benefits in predicting patient survival has already been shown with the integration of diffusion connectomics information to basic clinical information (L. Liu et al., 2016). Gliomas positioned in a specific lobe and hemisphere appear to produce characteristic changes in terms of network efficiency and role of brain regions in the overall topology of the structural network (D'Souza, Hirt, et al., 2021). The same group additionally showed that normal appearing tissue in proximity of the lesion may feature microstructure alterations (D'Souza, Ormond, et al., 2019), highlighting widespread tissue abnormalities beyond the MR-evident tumoral lesion. Moreover, Liu and colleagues found that gliomas disrupt the rich-club organization of the brain, suggesting the structural resilience of the network is globally affected in presence of the tumoral mass (Y. Liu et al., 2020).

While these works focus on characterizing the alterations of global properties in the structural connectome, to our knowledge, no attempt has been made to characterize the pathophysiological state of the subject-specific nodes of the network, and how the presence of a tumoral lesion may alter their metabolic function when the associated structural links are compromised. To this end, in this work we propose an approach to detect altered WM connections based on the statistical analysis of SC matrices derived with dMRI tractography. To define compromised structural connections, we built a pseudo-healthy reference distribution for each entry of the SC matrix on the dataset at disposal and quantified the deviation of each subject from normative values. Each node of the network was then associated with a degree of alteration based on the number of its afferent compromised connections. Finally, we related this degree of alteration measures with metabolism variations quantified by regional [18F]-FDG PET Standardized uptake value ratios (SUVR).

5.2 Materials and Methods

5.2.1 MRI acquisition

The dataset and MRI acquisition details were identical to those written in Chapter 3. Due to computational complexity, the steps of tractography algorithm selection explained in Section 5.2.4 and Section 5.2.5 were executed on a subset consisting of 11 subjects from the entire dataset of 44 patients. Once the tractography

Name	Model	Orientation sampling	#streamlines	cut-off
iFOD2	SD	Probabilistic	10M	peak(FOD)=0.1
SD Stream	SD	Deterministic	10M	peak(FOD)=0.1
Tensor det	DTI	Deterministic	10M	FA=0.1
Tensor prob	DTI	Probabilistic	10M	FA=0.1

Table 5.1: List of the four tractography algorithms utilized to build the structural connectome. SD = Spherical deconvolution, FOD = fiber orientation distribution, FA = fractional anisotropy, DTI = diffusion tensor imaging.

algorithm was selected following those steps, from Section 5.2.6 onwards the entire dataset was used.

5.2.2 Tumour segmentation and structural preprocessing

Structural Processing and tumour segmentation details were described in Chapter 2 and 3.

5.2.3 dMRI processing and tractography computation

A first visual inspection was performed on the dMRI images, and those volumes containing significantly visible interslice instabilities (Bastiani et al., 2019) were eliminated from subsequent analysis. The subsequent steps of pre-processing were carried out within the MRtrix software (J-Donald Tournier, R. Smith, et al., 2019), and featured random-matrix based denoising via the *dwidenoise* (Veraart, Dmitry S Novikov, et al., 2016) and a joint correction for B0-inhomogeneties, subject motion and eddy currents via *dwifslpreproc* (Andersson, Skare, et al., 2003; Andersson and Sotiropoulos, 2016).

Tractography specifications are as follows. At first, multi-shell multi-tissue spherical deconvolution was performed to recover voxel-wise orientation distribution functions for WM, GM and CSF (Jeurissen et al. 2014). The structural connectome was then reconstructed with 4 different algorithms available in MRtrix, chosen to cover every combination of deterministic/probabilistic and DTI-based/SD-based tractography options. Further details of the reconstruction are reported in Table 5.1. For the two cases employing SD as the underlying diffusion model, the tractogram was generated with 100M streamlines and subsequently reduced to 10M through the SIFT framework (R. E. Smith et al., 2013).

The Schaefer Atlas featuring a 17-networks, 100-regions cortical parcellation of the brain (Schaefer et al., 2018) was employed to define the individual SC matrices, based on the number of streamlines metric, for each of the quantified

tractograms.

5.2.4 Tractography algorithm selection criteria

The physiological plausibility of axonal fibers tracked by diffusion-MRI (dMRI) currently is a central problem for the clinical application of tractography algorithms (Jeurissen, Descoteaux, et al., 2019). We here adopted an atlas-based approach for objectively comparing different tractography strategies in terms of how accurately white matter tracts are reconstructed.

Starting from the tractograms of the four algorithms, with the tools provided by the open-source *whitematteranalysis* package from the dMRISlicer software, we performed the implemented spectral clustering procedure (O'Donnell et al., 2007) to automatically reconstruct 73 deep white matter tracts (the complete list of segmented tracts can be found in (F. Zhang, Y. Wu, et al., 2018)). The clustering was performed independently for each of the alternatives of Table 5.1. While the reconstruction and physiological validation of the anatomical pathways with the present software was initially designed for healthy subjects, it was shown to generalize well in patients with brain tumours in a recent study (O'Donnell et al., 2017). The Atlas we use for the comparison of the different algorithms is available in the aforementioned software, and is detailed by Zhang and colleagues (F. Zhang, Y. Wu, et al., 2018). Such decision was dictated by the high amount of subjects the atlas is composed of (i.e. 100 subjects, from the Human Connectome Project publicly available dataset, `https://www.humanconnectome.org`), and by the presence of a subsequent manual annotation of anatomical segments by expert neuroanatomists. Moreover, this streamline-based atlas was created with a two-tensor unscented Kalman filter tractography (Malcolm et al., 2010), an option which is not object of our comparisons, thus eliminating any same-algorithm-tracking bias. For each tractogram, we quantified how the streamlines are subdivided into each defined bundle and compared this distribution to the one of the anatomically curated atlas. Mathematically, for any given tract, let $n_t(alg)$ be the number of streamlines which the clustering procedure assigned to the anatomical tract t from the original tractogram quantified with algorithm alg. We then defined the normalized number of streamlines of the anatomical tract as:

$$p_t(alg) = \frac{n_t(alg)}{\sum_{t \in T} n_t(alg)} \tag{5.1}$$

Where T is the set of all the 73 clustered tracts. Such a normalization is neces-
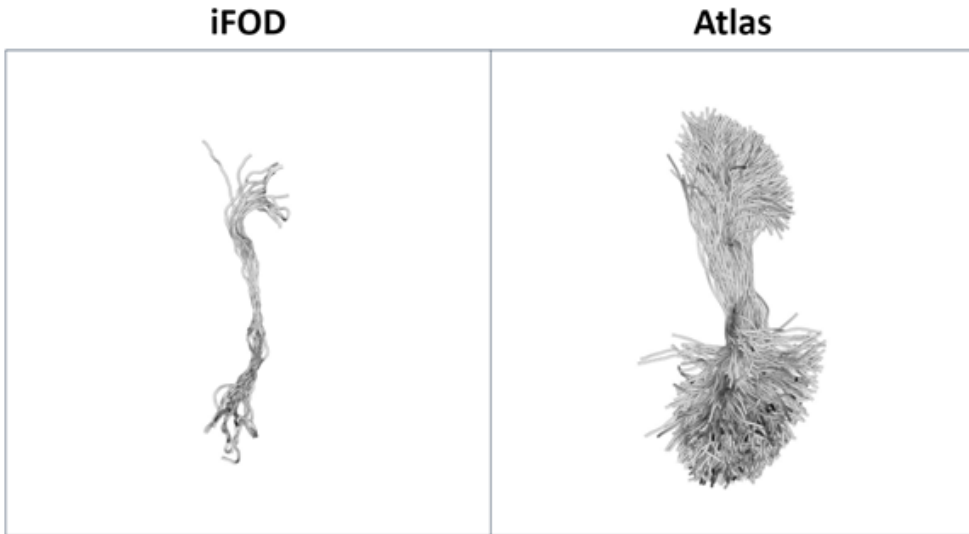
Figure 5.1: Example of $r_t(iFOD2) << 1$ for a representative patient of the dataset. On the left, the left external capsule as quantified by the iFOD2 algorithm; On the right, the left external capsule as represented in the utilized anatomically constrained atlas.

sary even in the case of input tractograms having an equal number of streamlines, as the outlier rejection procedure present in the software (F. Zhang, Savadjiev, et al., 2018; O'Donnell et al., 2017), which is based on evaluating the similarity distance of each fiber from the centroid of the assigned cluster, may behave differently in dependence of the tracking algorithm used. We then define the normalized ratio of streamlines of the anatomical tract as:

$$r_t(alg) = \frac{p_t(alg)}{p_t(atlas)} \tag{5.2}$$

The r_t measures evaluates how a given tract t is under/overrepresented in terms of number of streamlines with respect to the anatomically curated atlas of choice (e.g. $r_{EC} << 1$ highlights how the given tractogram employs a much lower portion of its total number of streamlines to represent the external capsule (EC) with respect to the anatomically curated atlas. See Figure 5.1). By quantifying r_t in our dataset, we wish to understand which of the algorithms in Table 5.1 comes closer to the atlas representation in terms of the anatomical distribution of streamlines. Figure 5.2 provides a graphical representation of the r_t computation.
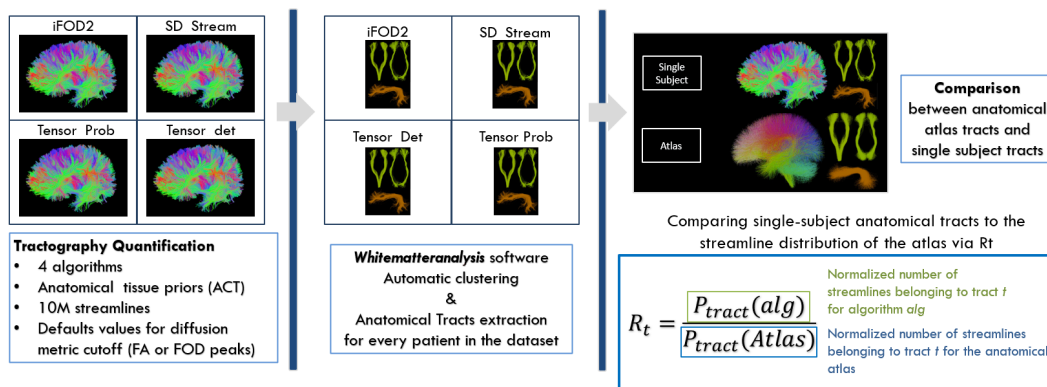
Figure 5.2: Graphical representation of the steps which, starting from the tractograms, lead to the r_t computation. ACT = anatomically constrained tractography, FA = fractional anisotropy, FOD = fiber orientation distribution.

5.2.5 Cut-off value for tract termination decision

The streamline termination criterion may have a noticeable effect on the reconstruction of the tractogram. Once the tractography algorithm was chosen by evaluating the r_t measure described above, we were subsequently interested in verifying that the cut-off value for stopping the tracking would not severely impact the obtained connectome. More specifically, apart from software defaults, we tested 5 progressively more permissive thresholds (i.e., FA or FOD amplitude values equal to 0.09, 0.08, 0.07, 0.06, 0.05) and verified the sensitivity of SC matrices to their variation. The quantitative framework employed was based on two techniques:

- **The Krzanowsky test**: Given a set of matrices, the Krzanowsky test (Krzanowski, 1993) tests the hypothesis that the two population SC matrices obtained respectively with a cut-off value of 0.1 and of 0.05 (the extreme values of the cut-off range) share similar eigenvectors and eigenvalues. The test has been run with 1000 permutations and a significance level of $\alpha = 0.05$.

- **The principal component analysis (PCA)**: The PCA analysis allows to test whether the single-subject set of SC matrices, reconstructed with different cut-off values, share a similar structure. In practice, we computed the first principal component for each subject and analyzed its explained variance (EV).

The difference between two SC matrices (or lack thereof) quantified with the two extreme values of the tested cut-off interval (i.e., 0.1 and 0.05) can be

Figure 5.3: On the left, a structural connectivity (SC) matrix quantified with a 10M iFOD2-based tractogram and a streamline cutoff value of $peak(FOD) = 0.05$). On the right, the same SC matrix, but whose tractogram had a streamline cutoff value of $peak(FOD) = 0.1$.

appreciated in Figure 5.3.

5.2.6 Defining structurally altered links of SC matrices

After having determined the algorithm and cut-off value with which to proceed, structurally altered links were identified using the following statistical procedure:

- For each subject, we firstly identified all pseudo-healthy entries of its SC matrix. The criteria for such a selection were two: 1) the Schaefer regions constituting the endpoints of the link needed to feature an overlapping with the tumoural lesion for less than 5% of the total volume of the parcel, and 2) streamlines connecting such endpoints were required not to cross the tumoral lesion at any position. Following these exclusion criteria, Figure 5.4 shows the number of subjects for each SC entry which satisfy the pseudo-healthy conditions.

- Using the above defined pseudo-healthy data, we reconstructed the pseudo-healthy distribution for all entries of the SC matrix. As the majority of these distributions had significant non-gaussian features, they were non-parametrically characterized by their median and Mean Absolute Deviation (MAD).

- SC entries either featuring singular distributions (i.e. having their median and/or MAD identically equal to zero) or being streamline-poor (having less

Figure 5.4: Matrix showing the link-wise number of subjects which are labelled as 'pseudo-healthy' after the exclusion process described in the text.

than 10 streamlines on average) were discarded from subsequent analyses. This selection was performed to exclude from further analyses SC entries which were due to noise and false positive connections.

- For all subject, each individual SC entry was then compared with its reference pseudo-healthy distribution. The link was defined as structurally altered if the following condition was true:

$$SC_i(j,k) < SC_{med}(j,k) - 3MAD_{j,k} \qquad (5.3)$$

where (j,k) defines the specific entry of the SC matrix, SC_i is the subject-specific SC matrix, SC_{med} is the median pseudo-healthy SC matrix and $MAD_{j,k}$ denotes the MAD of the pseudo-healthy distribution for the specific entry.

We called the 3MAD matrix the subject-wise binary matrix containing the structurally altered entries defined by (5.3). The process just described is graphically depicted in Figure 5.5.

5.2.7   PET acquisition, pre-processing and quantification

PET scans were acquired simultaneously to MRI images on the Siemens Biograph mMR (Siemens Medical Solutions USA, Inc.) PET/MRI scanner equipped with

Median SC Matrix
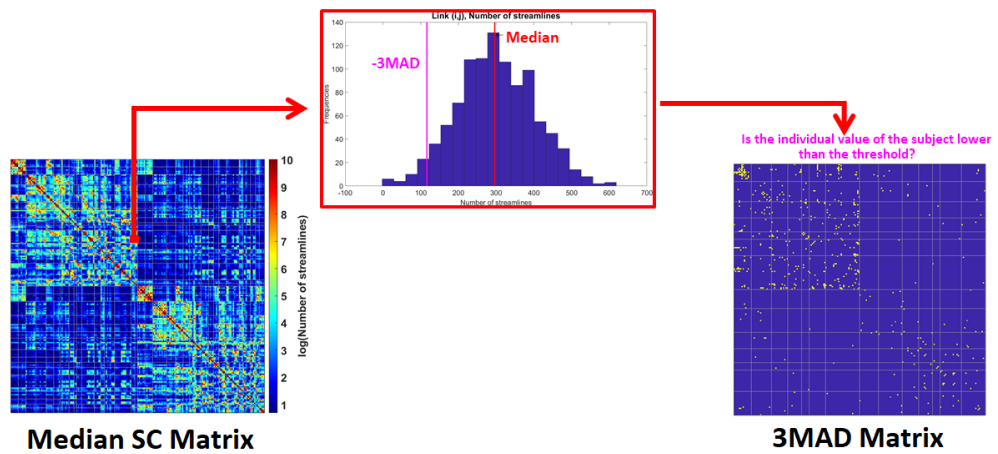
3MAD Matrix

Figure 5.5: Visualisation of the statistical methodology used to derive subject-specific 3MAD matrices. Each individual entry of the structural connectivity (SC) matrix is compared to its pseudo-healthy reference from the dataset at hand. If the streamline count is inferior to the chosen threshold, the corresponding location in the 3MAD matrix is highlighted.

a 16-channels head-neck coil described above. Concerning PET imaging protocol, after the tracer administration, a 60-minutes dynamic PET list mode acquisition was performed. An average dose of 206.5 MBq (range: 145-303MBq, according to the body mass index) of [18F]2-fluoro-2-deoxy-D-glucose ([18F]FDG) was intravenously administered to each patient. The scanner was calibrated with recommended quality assurance (QA) regimes implemented and daily QA pass before clinical use to ensure accuracy and consistency of scanning was maintained. Exploiting the last 20 minutes of acquisition, for each patient the PET static image was reconstructed offline using the Siemens e7-tool for Biograph mMR. The image reconstruction pipeline included correction for scatter, dead time, attenuation (due to head and radio-frequency coil), tracer decay and normalization. Image reconstruction was performed with Poisson ordered subset expectation maximization (3 iterations and 21 subsets). No spatial smoothing was performed after reconstruction. The patient's head attenuation map was estimated from the individual T1w MPRAGE image as in the work of Izquierdo-Garcia and colleagues (Izquierdo-Garcia et al., 2014). At the time of beginning of the study, this method was one of the best performing methods for MR-based attenuation correction (Ladefoged et al., 2017). The Standard Uptake Volume Ratio (SUVR) was employed to semi-quantify the local brain metabolism. As cerebellum is an area where the incidence of glioma is very low (4.5% of all gliomas according to Miller and colleagues (Miller et al., 2021)) and a crossed cerebellar diaschisis is

not infrequent in glioma patients (Wiestler et al., 2016), we used the cerebellum grey matter ipsilateral to the tumour as reference region. Such reference was identified in two steps:

1. Firstly, for each patient the cerebellum was segmented using the Hammersmith brain atlas (Hammers et al., 2003) which was non-linearly coregistered into the individual PET naïve space passing through the patient's T1w MPRAGE image employing ANTs (Avants et al., 2011).

2. Secondly, the cerebellum grey matter which was ipsilateral to the tumour was extracted masking the cerebellum Hammersmith segmentation with a patient's grey matter segmentation obtained with the Segmentation routine included in the Statistical Parametric Mapping (SPM) 12 tool (SPM12, v. 7219).

5.2.8 Computing the alteration for each network node

Once the subject-wise 3MAD matrix was created, showing which link for each subject was potentially impaired in our cohort of subjects, we proceeded to define a measure of overall alteration of each node. In analogy to the graph analysis concept of node degree (Bassett et al., 2017), for each node j, we defined a measure of its alteration as:

$$Degree(j) = \sum_{i=1}^{K} 3MAD(i,j) \tag{5.4}$$

Equation 5.4 associates each node of the SC network to a measure of severity of damage to its structural connections. As will be explained in subsequent sections below, this metric has been investigated in relationship with the regional SUVR derived from PET measures.

5.2.9 Measuring the impact of the tumoral lesion size and location on the detected alterations

Scatterplots of the tumoral region size vs the number of altered connection were produced to inspect the dependence between these two quantities. Spearman's correlation was computed to quantitatively support visual findings, using a $\alpha = 0.05$ statistical significance threshold. After dividing the subjects based on the hemispheric location of the tumour(i.e, right,left and bilateral tumours), for each of these subpopulations three boxplots reporting the number of altered

links detected in each hemisphere were computed. The patient-wise number of altered links contained in each hemisphere was normalized to the total number of SC links in that hemisphere.

5.2.10 Topological distinction of the nodes of the structural network

The nodes of the network were characterized both in terms of their topological role and in terms of their relationship with the presence of the pathology. More specifically, we characterized the following node subdivisions:

- **Hub / Non Hub**: We identified the hubs of the structural connectivity networks following the indications of Oldham and colleagues (Oldham et al., 2019). Briefly, in the cited work a network node is identified as a hub if both its degree and betweeness centrality are superior to a threshold identified as the mean plus the standard deviation of the distribution of such indexes across all nodes. In our case, we evaluated these thresholds based on the pseudo-healthy median matrix described above. Furthermore, as the degree and betweeness centrality distributions were significantly non-gaussian, in our computation we substituted the mean and standard deviation with their non-parametric versions (i.e., the median and the mad)

- **Normal Appearing / Oedema / Tumour**: With respect to the presence of the tumoral lesion in each patient, nodes were additionally classified in base of the nature of the tissue overlapping its region. More specifically, nodes were identified as *normal appearing* if their spatial intersection with the tumoral lesion was inferior 5% of their total volume. Should this condition not be verified, a node was classified as either *Oedema* or *Tumour* based on which of the two pathological tissues was most prevalent in the volume which defined the node.

5.2.11 Multimodal association of structural and metabolic measures

As the degree of alteration defined above is a categorical variable, the association between this measure regional [18F]-FDG SUVR was quantified by means of Spearman correlation. A $\alpha = 0.05$ threshold was chosen for statistical significance. Scatterplots defining the structure-metabolism relationship were produced to visually aid the interpretation of correlation results.

Figure 5.6: Median r_t computed across 11 subjects for each anatomical tract and algorithm in Table 5.1, across the 11 patients of the dataset at disposal. Each line here represents an algorithm.

5.3 Results

5.3.1 Tractography algorithm selection and cut-off value sensitivity

Figure 5.6 shows the median r_t for all 73 tracts computed across the 11 subjects. Each line here represents a specific algorithm. Several trends can be noticed in terms of streamlines distribution between different anatomical bundles, and that they are usually followed by all the four proposed tracking alternatives. Most notably, all of them tend to employ a higher number of streamlines with respect to the anatomically curated atlas to form the striato-parietal (SP) tract. Several other anatomical tracts in the left portion of the graph, however, remain highly underrepresented: the most notable examples here are the EC (again, shown as example in Figure 5.1) and the extreme capsule (EmC).

Figure 5.7 and Figure 5.8 show, respectively, the median r_t and its MAD computed across the 73 tracts for the 11 subjects and the four investigated algorithms. The agreement of a tractogram's streamline distribution to the one of the anatomically curated atlas can be represented by a median r_t close to 1 and MAD as low as possible. From both figures it can be seen that both properties are scored consistently for the iFOD2 algorithm across all subjects, with the other three fiber tracking options being generally worse.

Having chosen the iFOD2 algorithm to proceed with the analysis, we tested

Figure 5.7: Median r_t computed across the 73 anatomical tracts for each patient (X axis) and algorithm in Table 5.1 (Y axis)

whether changing the streamline cut-off value to more permissive thresholds would significantly affect the resulting SC matrices.

Table 5.2 reports the EV of the first principal component (PC1) of the PCA computed on the SC matrices with varying cut-offs. The EV was equal on average to $99.3 \pm 0.33\%$. It follows that, in all patients, the EV of the second (PC2) and following principal components was lower than 1%, as shown in Figure 5.9. These findings suggest an extremely strong common structure to be present between matrices computed by simply varying the termination criteria. In fact, apart from the common structure described PC1, the other PCs contribute trivially to defining the heterogeneity of the subject-wise sets of matrices. The PCA results were confirmed at the group level by the Krzanowski test, as no statistically significant difference was found between eigenvalues/eigenvectors of the set of SC matrices computed with $peak(FOD) = 0.1$ and $peak(FOD) = 0.05$ as streamline termination criteria ($p = 0.87$). Given the minimal sensitivity of SC matrices to the tested cut-off values, for the subsequent analysis, we decided to keep the default MRtrix3 value of 0.1. This choice was evaluated in terms of overall replicability and possibility to compare the findings of this study with the literature, as its the most commonly used setting.
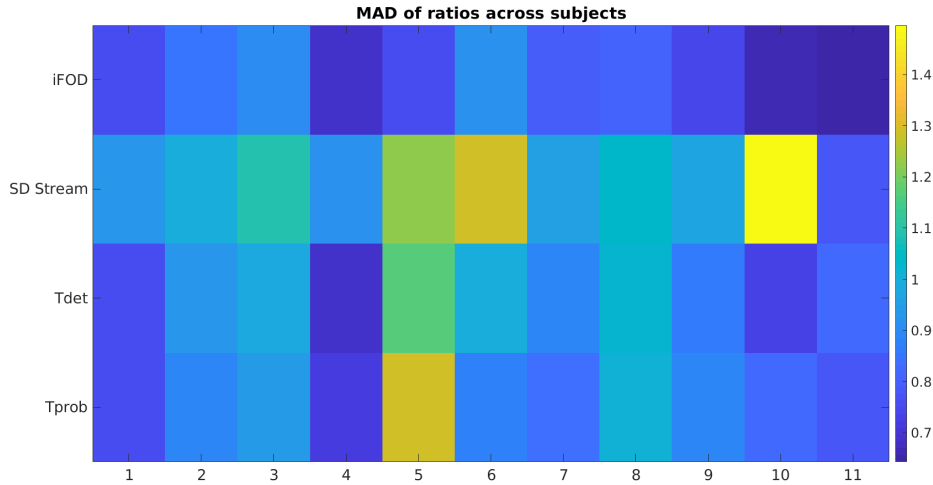
Figure 5.8: Mean absolute deviation of r_t, computed across the 73 anatomical tracts for each patient (X axis) and algorithm in Table 5.1 (Y axis). MAD = mean absolute deviation.

5.3.2 Structurally altered connections and tumour location/size

Figure 5.10 shows the correlation between the extension of both the tumoral lesion/core and the number of altered structural links that are quantified with our approach. Pearson's correlations are strong and statistically significant in both cases ($r_{lesion} = 0.78$, $p_{lesion} = 10^{-10}$, $r_{core} = 0.51$ $p_{core} = 0.003$). Interestingly, when including the oedematous tissue in the analysis, the correlation and its significance are much stronger, highlighting its central role in the definition of structurally altered links.

Moving to the SC impact of tumours in different locations, Figure 5.11 shows respectively the number of altered links found in each hemisphere for left, right and bilateral tumours. As expected, each tumour appears to disrupt the structural connectivity in the same hemisphere it is located, along with interhemispheric connections. While lower in number, contralateral alterations were still detected in cases of right and left tumours, suggesting that the focal tumoral lesion additionally causes widespread abnormalities at distance in the brain.

Figure 5.12 shows the analogous of Figure 5.11 for interhemispheric connections. As expected, bilateral tumours impact these links the most, but a significant interhemispheric connection alterations are found also for left and right tumours.
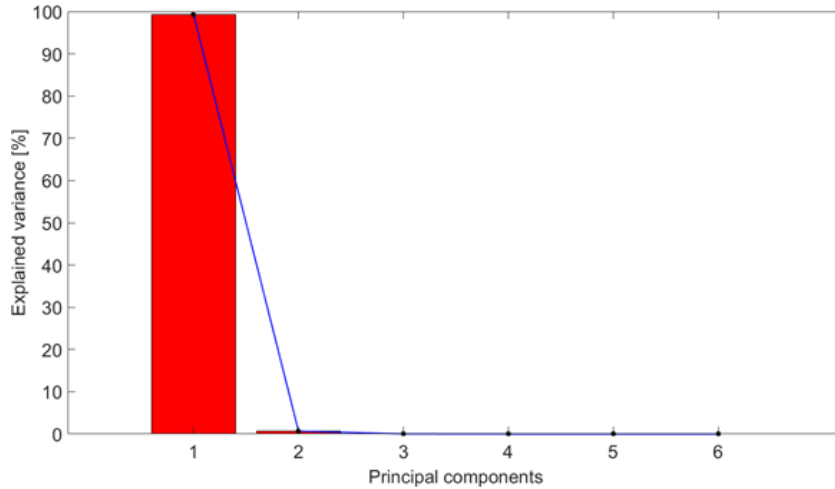
Figure 5.9: Explained variance for each principal component of the principal component analysis (PCA) for a representative subject. The PCA analysis was run on the set of cutoff-varying structural connectivity matrices for every subject.

5.3.3 Association of metabolic and structural measures

Firstly, Figure 5.13A shows the relationship between the SUVR of a region and the degree of alteration of its structural links, making the distinction in Hubs ($r_{hub} = -0.24$ $p_{hub} = 1.96e - 08$) and non-Hubs ($r_{hub} = -0.221$ $p_{hub} = 1.96e - 42$) of the network. Figure 5.13B and Figure 5.13C show boxplots respectively expressing the amount of structurally altered links and SUVR for regions belonging to the two categories. Both these quantities differ between hubs and non-hubs nodes ($p_{alter} = 2.9e - 20$ and $p_{SUVR} = 0.027$, respectively). Hubs with non-zero degree of alteration were more impacted than peripheral nodes in terms of the metabolism, featuring overall lower SUVR values.

Next, we proceeded to investigate the structure-metabolism relationship between healthy and pathological nodes. As such, Figure 5.14A shows the scatterplot between the SUVR of a region and the degree of alteration of its structural links, for regions belonging to the normal appearing tissue ($r_{norm} = -0.165$, $p_norm = 8.6e - 28$), the oedematous region ($r_{oed} = 0.12$, $p_{oed} = 0.15$) and the tumoral region ($r_{tum} = 0.105, p_{tum} = 0.069$). The only statistically significant relationship was found for normal appearing grey matter. In these regions, the trend shows that the higher the number of faulty links with the rest of the brain, the lower its SUVR is. Figure 5.14B and 5.14C show boxplots respectively expressing the amount of structurally altered links and SUVR for regions belonging to the three different tissues. Regions with high tumour/oedema invasion show impairment on more connections than normal appearing cortical regions, and

Subject	EV of PC1
#01	99.27
#02	99.30
#03	98.85
#04	99.98
#05	99.43
#06	99.03
#07	98.96
#08	99.39
#09	99.14
#10	98.78
#11	99.07

Table 5.2: Bar plot of the explained variance for all the components of the PCA analysis on the SC matrices of a representative subject.

lower SUVR than normal appearing tissues.

Focusing further investigation on the normal appearing nodes, Figure 5.15 shows the structural alterations VS metabolism scatterplots for the entire dataset (reported above) and specifically glioblastoma (gbm) patients ($r_{gbm} = -0.118$ and $p_{gbm} = 6.17e-11$). As gbms are between the most infiltrative subtypes of gliomas, we would have expected a stronger anti-correlation with respect to the entirety of the dataset, but we could not confirm such an hypothesis.

Lastly, to reduce the heterogeneity in the results, we extended the correlation analysis between structure and metabolism by looking separately to each Schaefer brain region. To ensure that statistical testing featured reasonable results, the analysis was restricted to nodes which were normal-appearing in at least 15 subjects in our dataset. Figure 5.16 shows the scatterplots of the regions for which a statistically significant (FDR-corrected) correlation was found (Table 5.2 shows the region ID, network of belonging and correlation values). When accounting for the regional heterogeneity of SUVR values, a much stronger association was found between structural alterations and metabolic changes in several normal appearing regions of the brain.

5.4 Discussion and conclusions

Overall, In this work several results were presented, concerning three different main points:

- the optimal selection of both the tractography algorithm and the streamline
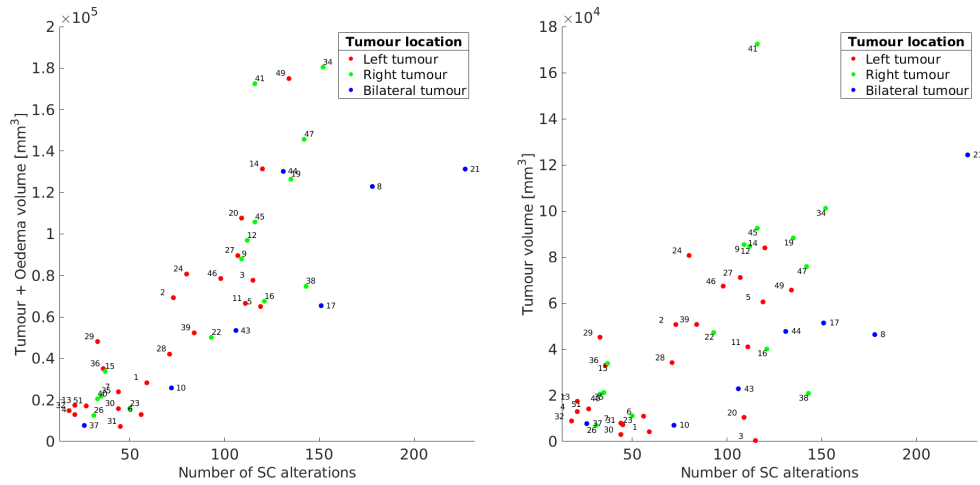
Figure 5.10: On the left, the scatterplot between the tumoral lesion size (i.e., tumour core + oedema) and the number of the quantified altered connections. On the right, the scatterplot between the tumoral core size (i.e., only the tumour core) and the number of the quantified altered connections. Different colors denote the tumour location for the specific patient.

termination cut-off value for the computation of the SC matrices.

- the development of a statistical procedure to define structural links which are altered due to the presence of the tumour in each subject.

- the multimodal association between the degree of alteration of SC connections afferent to a node and regional metabolic changes measured by 18F-FDG PET.

As done in the results section, the different outcomes of this work will be discussed separately in different subchapters.

5.4.1 Tractography algorithm selection and cut-off value sensitivity

The physiological validation of reconstructed tractograms has always been a central problem in the field of diffusion MRI. It is widely known that tractography algorithms provide an approximate reconstruction of white matter pathways in a 'connecting the dots' fashion. Local diffusion orientation, representing the direction along which axonal fibers propagate, are interpolated together to extract a surrogate measure of the connection between different regions of the brain. Such reconstruction methods, while detecting the majority of true axonal bundles, are extremely susceptible to computing false positive streamlines (i.e, streamlines
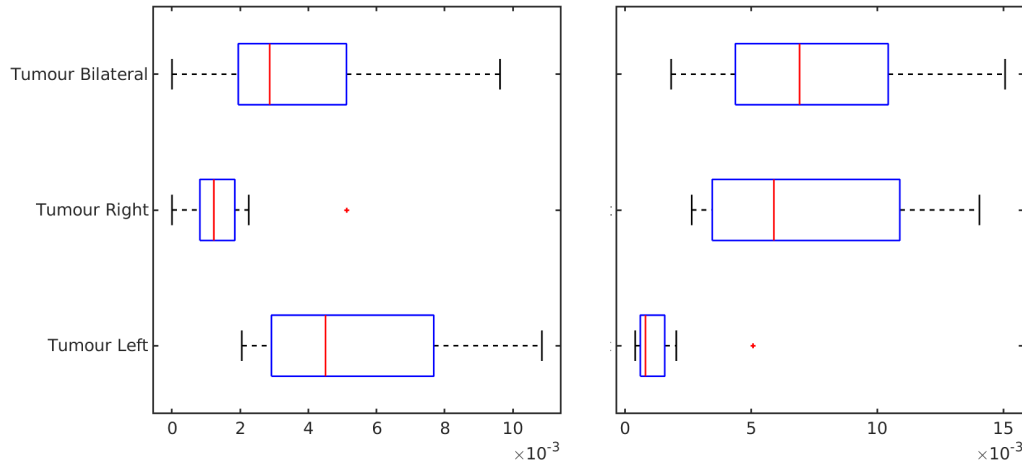
Figure 5.11: On the left, boxplots of the normalized number of structurally altered links in the left hemisphere computed respectively for the subpopulation of subjects with a tumour in the left, right and both hemisphere. On the right, the same analysis was conducted for the altered links in the right hemisphere.

Region ID	Network classification	Spearman's R
79	Default A	-0.51
86	Default B	-0.47
108	Visual Peripheral	-0.739
153	Saliency/Ventral Attention	-0.544
158	Limbic B	-0.594
172	Control Components B	-0.569
178	Control Components B	-0.639
182	Default A	-0.553
197	Temporal-Parietal	-0.632

Table 5.3: Regions of the Schaefer's Atlas for which a statistically significant relationship was found between the degree of alteration and regional metabolism

which represents fibers which do not really exist in the brain) (Maier-Hein et al., 2017). While tracing axons with virtual and physical phantoms (Côté et al., 2013) and other techniques (Grisot et al., 2021; Knösche et al., 2015) can help in discerning which connections are more accurate than others, these approaches cannot be applied subjectively to every patient, and rely on validation on external data. We here presented an application of the open-source software package *whitematteranalysis* to test for the physiological plausibility of a given tractogram by comparing it with an anatomically-curated atlas of streamlines. While the proposed r_t is prone to bias and pitfalls of tractography measures, it gives a first depiction on how the total number of streamlines is partitioned amongst physiological bundles. From our anaysis the iFOD2 algorithm appears
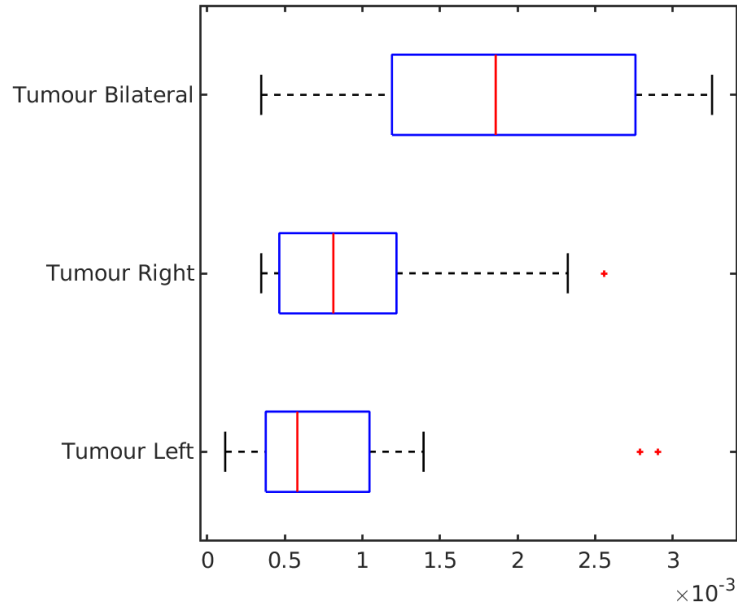
Figure 5.12: The boxplot of the normalized number of structurally altered links in each hemisphere for the subpopulation of subjects with a bilateral tumour.

to produce a structural connectome which, between the alternatives, is the most similar on average to the anatomically curated atlas in use. This algorithm additionally appears to be the most consistent across the tested subjects, featuring the lowest mean MAD of the studied options. In terms of the criterion for terminating streamlines, the Krzanowski test and the PCA analysis revealed, respectively inter- and intra-subjects, that no significant variation was found amongst SC matrices computed by only modifying the cutoff value. Indeed, the null hypothesis (H0, no variation between groups) of the test was accepted and the first principal components of the set on intra-subject SC matrices featured at least 98% of EV in all subjects. Thus, these results support the hypothesis that only minor modifications occur in the overall structural connectivity estimation by using more permissive thresholds. As the in the current literature using the Mrtrix3 software this parameter is set to default values, we opted for the same choice in order to ensure the replicability and comparability of our results.

5.4.2 The statistical definition of altered SC links and its sensitivity to tumour size and location

As it is reasonable to expect, a strong correlation was found between the size of the tumoral lesion and the amount of structurally altered links detected in a
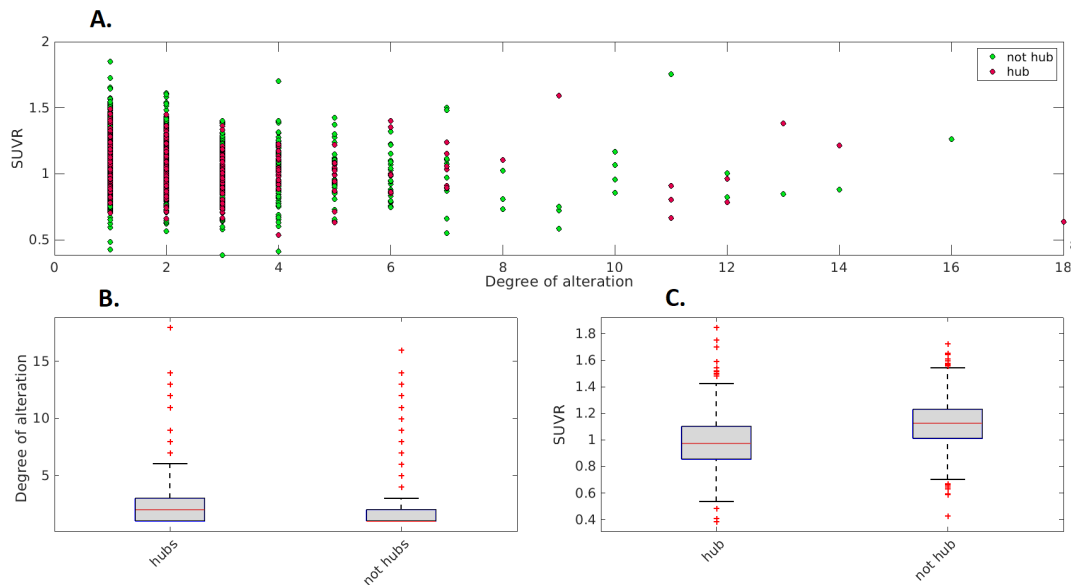
Figure 5.13: In A, the scatterplot between SUVR values for all regions of every patient and the degree of structural alteration of its connections. Nodes were divided in hub regions (red) and non-hub (green). In B, boxplots showing the degree of alteration for hubs and non hubs. In C, boxplots showing the regional SUVR for hubs and non hubs.

patient. This findings supports the hypothesis that the developed technique is sensitive to the extension of the pathology and is able to capture the microstructural abnormalities it causes. Of particular interest is the fact that the correlation and p-value is significantly weaker when excluding the oedema from the analysis. The heterogeneity of the oedematous tissue, both in terms of its extension and composition, is object of many studies investigating the deficits and prognosis caused by tumours (Dehcordi et al., 2013; C.-X. Wu et al., 2015; X. Qin et al., 2021), and we here have shown its importance to describe structural damage. Thus, the findings in our study support the inclusion of the oedema in all tumour-related analyses, as it considerably strengthens the association between the measure of structural alterations we defined and the presence of the cancerous lesion. While the majority of altered SC links are found in the ipsilateral hemisphere to the tumoral lesion and cross-hemispheric alterations, a non-negligibile amount of altered links is also found in the contralateral portion of the brain for every subject. Indeed, as we also were able to detect, widespread alterations in normal appearing WM and GM were recently shown in several studies with glioma patients (D'Souza, Ormond, et al., 2019; Yuan et al., 2020; X. Wang et al., 2020), suggesting that neuroplasticity and pathological phenomena may induce modifications in the brain also at distance from the tumoral lesion. Overall, the
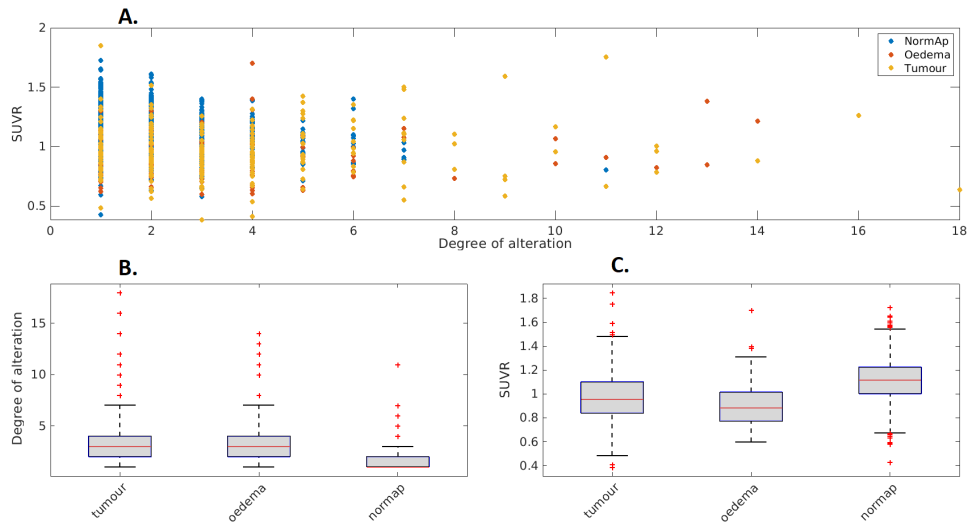
Figure 5.14: In A, the scatterplot between Standardized uptake value ratios (SUVR) values for all regions of every patient and the degree of structural alteration of its connections. The color code distinguishes between the three different tissues. In B, boxplots showing the number of structurally altered links for regions respectively occupied by normal appearing tissue, oedema and the tumour core. In C, boxplots showing the SUVR for regions respectively occupied by normal appearing tissues, the oedema and the tumour core.

statistical procedure proposed in this work is one of the first attempts in literature to define the structural damage brain tumours cause in subject-specific connectomes. Of course, relying on the comparison between individual SC entries and its "dataset-defined" pseudo-healthy distribution, the definition of the latter is dependent on the number of subjects for which that specific connection is pseudo-healthy. Having at disposal larger datasets would lead to having better defined reference distributions and thus, more accurate detection of their left tails (i.e., the altered connections). Another key point of our metholodology is the assumption that the number of streamline connecting two region is a quantitative measure of the structural connection between the two. This is indeed a critical point, as in basic tractography analyses, there is little to no relationship between the streamlines and the original intensities of the dMRI signal (Jbabdi et al., 2011). This issue was in this work mitigated by processing the obtained tractogram with the SIFT framework (R. E. Smith et al., 2013; R. E. Smith et al., 2015). Briefly, with SIFT the original 100M streamlines tractography was filtered to a subset of 10M. This was done by relating each streamline to the original diffusion signal via the utilization of a proper cost function and subsequently pruning those connections whose contribution was non-significant. To reach our
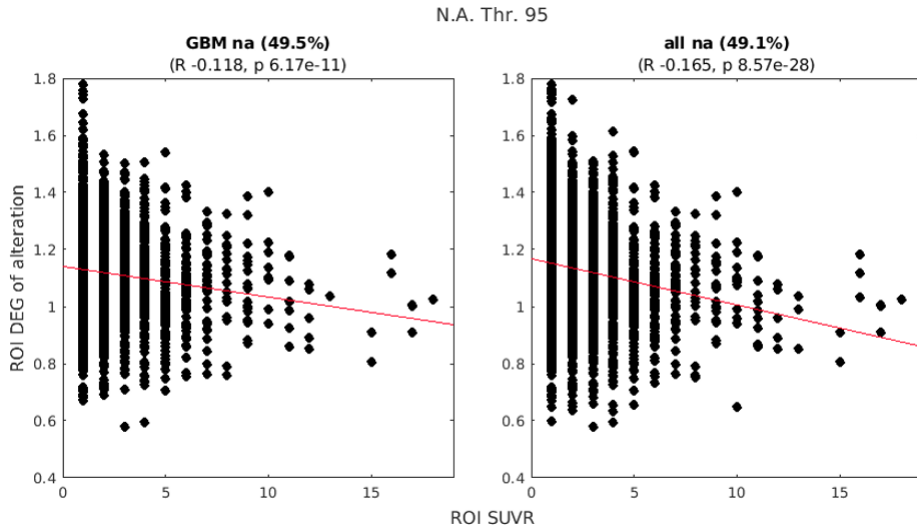
Figure 5.15: On the left, scatterplot of Standardized Uptake Value Ratios (SUVR) vs degree of structural alterations between normal appearing nodes of the SC matrices from glioblastoma subjects. On the right, the same scatterplot for normal appearing nodes from all subjects. GBM = Glioblastoma, na = normal appearing, DEG = degree.

objective, this step of the employed diffusion analysis pipeline was crucial, enabling more quantitative inference to be made from analyses of SC matrices based on the number of streamlines metric.

5.4.3 Multimodal association of structural and metabolic measures

A first analysis concerning the distinction between Hubs and Non-hubs nodes of the structural network was carried to understand how structural alterations were linked to metabolic variations in these two populations of regions. The trends in the scatterplots were confirmed by the correlation analysis, associating an inverse relationship between structural alterations and metabolic function. In general, we found that hubs were slightly more affected in terms of structural alterations than non-hubs, and that their SUVR was lower. Future studies may investigate this relationship further having at disposal a dataset with healthy adults. Indeed, characterizing the metabolic state of healthy hubs and non-hubs may allow for the computation of baseline metabolism changes in presence of alterations, instead of the absolute values presented here. Unfortunately, no such scans were at disposal at the time of the study, so we could not perform this additional analysis. Moving to more tissue-specific analyses, the only nodes for which a statistically
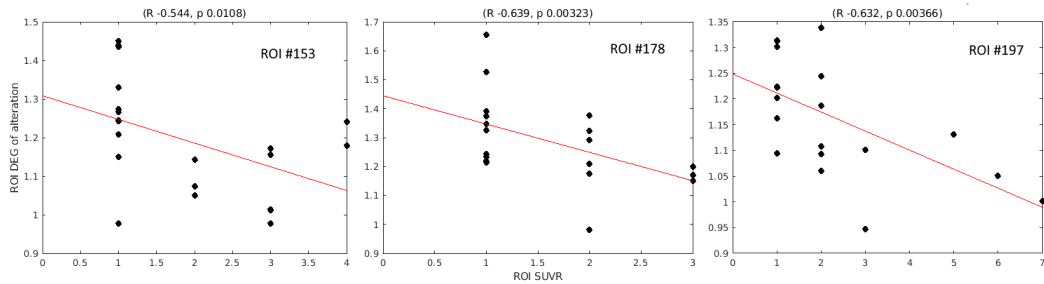
Figure 5.16: Illustratory Scatterplot depicting the relationship between regional standardize uptake value ratios (SUVR) values and degree of structural alteration in 3 of the 9 regions for which statistical significant correlation is achieved ($p < 0.05$, FDR corrected). DEG = degree

significant anti-correlation was found between the degree of alteration and the SUVR were those belonging to normal appearing GM. Indeed, when looking at the glucose uptake in oedematous and tumoral regions, the physiology of the underlying white matter network is disrupted, and the dependence between energy consumption and the state of axonal connections is questionable. Moreover, SUVR values are significantly different between and inside brain tumours subpopulations (Padma et al., 2003), reflecting an heterogeneity which appears not to be explainable in terms of alterations to the structural connectivity network alone. Restricting the multimodal association between metabolism and structure to the normal appearing GM nodes, we hypothesized that differentiating patients suffering from glioblastomas and the rest of the tumours would yield a stronger anti-correlation. These brain tumours are well known for being extremely infiltrative (Louis, Perry, Reifenberger, et al., 2016; Louis, Perry, Wesseling, et al., 2021), expanding beyond the MR-evident mass through normal white matter tracts. While we expected this aggressiveness to impair network nodes more severely, our results did not expose a weaker structure-metabolism correlation in this subpopulation of tumours. This weakened relationship may be due in part to glioblastoma having heterogeneous [18F]-FDG uptake based on mutations occurring in particular genes. Indeed, it has been shown by several studies that IDH1-mutated glioblastomas feature lower glucose consumption than IDH1 wild-type ones (F.-M. Liu et al., 2021) and are prognostically linked to better overall survival of patients (D. Kim et al., 2018). Both these variants are significantly present in our dataset, possibly causing heterogeneity in the results we obtain. Lastly, the node-specific analysis, which gave the strongest results of this study, was performed to account for the inter-region variability of FDG-PET measures. Indeed, this evaluation showed that some normal appearing GM regions were

strongly affected when several of their afferent axonal connections were impaired by the presence of a tumour. Recent findings suggested that brain tumors have broad repercussion on functional networks (Fox et al., 2018; Hacker et al., 2019). However, while PET has been extensively used to diagnose, differentiate and grade brain tumours, in current literature there has been strikingly low interest in studying metabolism-related changes outside of the tumoral/peritumoral area. The interplay between functioning neurons and the malignant tissue appears to be central in determining the progression of gliomas (Gillespie et al., 2018), and we here enforce the hypothesis that functional network changes (Harris et al., 2014) are accompanied by joint structural and metabolic abnormalities. The default mode network (DMN) appears to be at the centre of functional connectivity changes in brain tumour patients (Jütten et al., 2020; Hacker et al., 2019; Ghumman et al., 2016; Esposito et al., 2012), which is in line with our findings. Indeed, several of the regions for which we find a strong relationship between structural and metabolic alterations belong to this network. Our findings thus support the multimodal centrality of the role of this network in determining the cognitive progression of brain tumour patients. Our work additionally highlights the importance of abnormalities occurring in contralateral and interhemispheric structural connections, which may explain the corresponding functional alterations found by some glioblastoma studies (De Baene et al., 2019; Nenning et al., 2020).

5.4.4 Overall conclusions

In this work, we developed a statistical approach to evaluate altered structural connections based on the evaluation SC matrices in a cohort of brain tumour patients. After careful evaluation of which tractography algorithm to use for the computation of SC matrices, we have shown that this methodology may be sensitive to WM alterations happening both in proximity of the tumour location and at distance, in the hemisphere contralateral to it. We eventually correlated the degree of connection alteration of a node with its metabolism using 18F-FDG PET measures, showing that several cortical regions are metabolically impacted by the loss of physiological white matter links due to the pathology. As discussed throughout this chapter, the methodology we employ is mainly dependent on the ability of diffusion-MRI tractography to provide quantitative measures of connectivity between different regions of the brain. This topic is of pivotal importance in the field, and has always been object of heated debate (C.-H. Yeh et al., 2021; Jeurissen, Descoteaux, et al., 2019; Dmitry S Novikov, Kiselev, et al., 2018). Nev-

ertheless, We want to reinforce the fact that the processing and analysis pipeline featured here was targeted to minimize this issue. The structure-metabolism relationship we described supports the argument that tractography is a powerful tool that, when complemented by other imaging modalities, can offer new and precious insights into the physiopathology of brain tumours.

Chapter 6

Conclusions

This last chapter marks the closing section of this thesis.

Among the vast field of neuroimaging, Diffusion MRI stands out as one of the most promising tools to investigate the structure of the human brain. Indeed, given its intrinsic link with the diffusion of water molecules, dMRI provides the most specific access to tissues biological features, which are far below the nominal resolution of current MRI scanners. dMRI thus yields enormous promise to make the difference in the diagnosis and monitoring of several pathologies, including brain tumours, which were the main study focus of this thesis.

At the time of writing the diffusion MRI state of the art is bloated by the presence of multiple models, a plethora of tractography algorithms and abudant preprocessing methodologies concurrently minimizing sources of noise. While this is a problem which is starting to be tackled, general consensus for diffusion data analysis is still practically absent in the international MRI community. As such, without a shared direction, the translation of research result to the clinic has seen slow advancement since DTI was first introduced.

When I started this PHD programme, the question which I asked myself was: "This wide range of models, algorithms and analysis metholodgies which are available, how can I use them to extract meaningful information from the brain of patients suffering from tumours?". Thus, my work during these three years was not devoted to developing a new diffusion-based technique to throw in the chaos of the literature, but rather to explore new ideas to exploit what already was there to be used (indeed, as an engineer would do). This line of reasoning acts as a common thread to the three studies presented in this thesis, which dealt with different dMRI techniques applied to brain tumours. In fact, from the particular to the general, this three-years-spanning work dealt with voxel-wise estimation of diffusion properties, the assessment of local tractography modifications and

network-level structural connectivity analysis. For the sake of summarizing this thesis, a brief recap to the result obtained in this work follows.

- In Chapter 2, two microstructure models, NODDI and the SMT, were evaluated in terms of their goodness of fit and parameter estimation precision in the tumoral lesion. The concept of generalized sensitivity functions to analyze the optimality of the employed dMRI protocol in the various tissues was also introduced. While their biological meaning is still unknown in the tumor region, we showed that these techniques provide stable and reliable estimates inside it, making them suitable to use at least as signal representation in the search of new biomarkers to describe the pathophysiology of brain tumours.

- In Chapter 3, the use of tractography algorithms to quantify white matter disconnections in brain tumour patients was explored for the first time. Inside the chapter, a comparison between indirect (i.e., atlas based) and direct (i.e. tractography-based) approaches was performed, empirically showing there can be pronounced differences between them. The strengths and pitfalls of both methods were discussed, paying particular attention to highlight which pathological effects can or cannot be tracked by the two alternatives.

- In Chapter 4, a statistical procedure was developed to detect tumour-altered entries of individual structural connectivity matrices. Prior to its application, a careful selection of the tractography algorithm was in this chapter proposed. This choice was quantitatively evaluated both in terms of similitude to an anatomically curated atlas and sensitivity to streamline termination criteria. Finally, for the first time in the literature, metabolic alterations of normal appearing nodes of the structural network of patients were associated with the measure of structural alteration proposed in this work. This last multimodal analysis revealed that particular brain regions are metabolically affected when its structural connections feature pathological alterations.

Indeed the work featured within this thesis stands on its own in terms of the contribution to the research of brain tumours involving dMRI. As a conclusive thought however, I believe its greatest strength is more as a foundation to further research, rather than as a conclusive product. We are still far from having the perfect microstructure model, or a flawless tractography algorithm which only

and specifically tracks truly existing axonal bundles in normal and pathological tissues. Nevertheless, as discussed throughout the thesis, the analysis methodologies developed and employed here can only benefit from improvements in these fields, and thus can acquire more and more relevance in terms of clinical applicability as the science of diffusion MRI advances.

Bibliography

Aerts, Hugo JWL, Emmanuel Rios Velazquez, Ralph TH Leijenaar, et al. (2014). "Decoding tumour phenotype by noninvasive imaging using a quantitative radiomics approach". In: *Nature communications* 5.1, pp. 1–9.

Alexander, Daniel C (2008). "A general framework for experiment design in diffusion MRI and its application in measuring direct tissue-microstructure features". In: *Magnetic Resonance in Medicine: An Official Journal of the International Society for Magnetic Resonance in Medicine* 60.2, pp. 439–448.

Alexander, Daniel C, Tim B Dyrby, Markus Nilsson, et al. (2019). "Imaging brain microstructure with diffusion MRI: practicality and applications". In: *NMR in Biomedicine* 32.4, e3841.

Andersson, Jesper LR, Stefan Skare, and John Ashburner (2003). "How to correct susceptibility distortions in spin-echo echo-planar images: application to diffusion tensor imaging". In: *Neuroimage* 20.2, pp. 870–888.

Andersson, Jesper LR and Stamatios N Sotiropoulos (2016). "An integrated approach to correction for off-resonance effects and subject movement in diffusion MR imaging". In: *Neuroimage* 125, pp. 1063–1078.

Ashburner, John and Karl J Friston (2005). "Unified segmentation". In: *Neuroimage* 26.3, pp. 839–851.

Avants, Brian B, Nicholas J Tustison, Gang Song, et al. (2011). "A reproducible evaluation of ANTs similarity metric performance in brain image registration". In: *Neuroimage* 54.3, pp. 2033–2044.

Avram, Alexandru (2011). "Diffusion Tensor Imaging of Myelin Water identification". PhD thesis.

Aydogan, Dogu Baran, Russell Jacobs, Stephanie Dulawa, et al. (2018). "When tractography meets tracer injections: a systematic study of trends and variation sources of diffusion-based connectivity". In: *Brain Structure and Function* 223.6, pp. 2841–2858.

Basser, Peter J, James Mattiello, and Denis LeBihan (1994). "MR diffusion tensor spectroscopy and imaging". In: *Biophysical journal* 66.1, pp. 259–267.

Basser, Peter J, Sinisa Pajevic, Carlo Pierpaoli, et al. (2000). "In vivo fiber tractography using DT-MRI data". In: *Magnetic resonance in medicine* 44.4, pp. 625–632.

Bassett, Danielle S and Olaf Sporns (2017). "Network neuroscience". In: *Nature neuroscience* 20.3, pp. 353–364.

Bastiani, Matteo, Michiel Cottaar, Sean P Fitzgibbon, et al. (2019). "Automated quality control for within and between studies diffusion MRI data using a non-parametric framework for movement and distortion correction". In: *Neuroimage* 184, pp. 801–812.

Bloch, Felix (1946). "Nuclear induction". In: *Physical review* 70.7-8, p. 460.

Brown, Robert (1828). "XXVII. A brief account of microscopical observations made in the months of June, July and August 1827, on the particles contained in the pollen of plants; and on the general existence of active molecules in organic and inorganic bodies". In: *The philosophical magazine* 4.21, pp. 161–173.

Butcher, John Charles (1996). "A history of Runge-Kutta methods". In: *Applied numerical mathematics* 20.3, pp. 247–260.

Calamante, Fernando (2019). "The seven deadly sins of measuring brain structural connectivity using diffusion MRI streamlines fibre-tracking". In: *Diagnostics* 9.3, p. 115.

Callaghan, PT, KW Jolley, and J Lelievre (1979). "Diffusion of water in the endosperm tissue of wheat grains as studied by pulsed field gradient nuclear magnetic resonance". In: *Biophysical journal* 28.1, pp. 133–141.

Castellano, Antonella, Sara Cirillo, Lorenzo Bello, et al. (2017). "Functional MRI for surgery of gliomas". In: *Current treatment options in neurology* 19.10, pp. 1–23.

Caverzasi, Eduardo, Nico Papinutto, Antonella Castellano, et al. (2016). "Neurite orientation dispersion and density imaging color maps to characterize brain diffusion in neurologic disorders". In: *Journal of Neuroimaging* 26.5, pp. 494–498.

Chen, Ricky, Matthew Smith-Cohn, Adam L Cohen, et al. (2017). "Glioma sub-classifications and their clinical significance". In: *Neurotherapeutics* 14.2, pp. 284–297.

Clark, Chris A, Thomas R Barrick, Mary M Murphy, et al. (2003). "White matter fiber tracking in patients with space-occupying lesions of the brain: a new technique for neurosurgical planning?" In: *Neuroimage* 20.3, pp. 1601–1608.

Conturo, Thomas E, Nicolas F Lori, Thomas S Cull, et al. (1999). "Tracking neuronal fiber pathways in the living human brain". In: *Proceedings of the National Academy of Sciences* 96.18, pp. 10422–10427.

Côté, Marc-Alexandre, Gabriel Girard, Arnaud Boré, et al. (2013). "Tractometer: towards validation of tractography pipelines". In: *Medical image analysis* 17.7, pp. 844–857.

Crossley, Nicolas A, Andrea Mechelli, Jessica Scott, et al. (2014). "The hubs of the human connectome are generally implicated in the anatomy of brain disorders". In: *Brain* 137.8, pp. 2382–2395.

D'Souza, Shawn, Lisa Hirt, David R Ormond, et al. (2021). "Retrospective analysis of hemispheric structural network change as a function of location and size of glioma". In: *Brain communications* 3.1, fcaa216.

D'Souza, Shawn, D Ryan Ormond, Jamie Costabile, et al. (2019). "Fiber-tract localized diffusion coefficients highlight patterns of white matter disruption induced by proximity to glioma". In: *PLoS One* 14.11, e0225323.

Daducci, Alessandro, Erick J Canales-Rodrıguez, Hui Zhang, et al. (2015). "Accelerated microstructure imaging via convex optimization (AMICO) from diffusion MRI data". In: *NeuroImage* 105, pp. 32–44.

De Baene, Wouter, Geert-Jan M Rutten, and Margriet M Sitskoorn (2019). "Cognitive functioning in glioma patients is related to functional connectivity measures of the non-tumoural hemisphere". In: *European Journal of Neuroscience* 50.12, pp. 3921–3933.

Dehcordi, S Raysi, M Mariano, M Mazza, et al. (2013). "Cognitive deficits in patients with low and high grade gliomas". In: *J Neurosurg Sci* 57.3, pp. 259–266.

Dell'Acqua, F and JD Tournier (2017). "Reconstructing fiber orientations with diffusion MRI". In: *NMR Biomed.*

Dhermain, Frederic G, Peter Hau, Heinrich Lanfermann, et al. (2010). "Advanced MRI and PET imaging for assessment of treatment response in patients with gliomas". In: *The Lancet Neurology* 9.9, pp. 906–920.

Di Vita, Antonella, Liana Palermo, Maddalena Boccia, et al. (2019). "Topological map of the body in post-stroke patients: Lesional and hodological aspects." In: *Neuropsychology* 33.4, p. 499.

Doshi, Jimit, Guray Erus, Yangming Ou, et al. (2013). "Multi-atlas skull-stripping". In: *Academic radiology* 20.12, pp. 1566–1576.

Duffau, Hugues (2019). "Surgery for Malignant Brain Gliomas: Fluorescence-Guided Resection or Functional-Based Resection?" In: *Frontiers in surgery* 6, p. 21.

Efron, Bradley and Robert J Tibshirani (1994). *An introduction to the bootstrap*. CRC press.

Einstein, Albert (1905). "Über die von der molekularkinetischen Theorie der Wärme geforderte Bewegung von in ruhenden Flüssigkeiten suspendierten Teilchen". In: *Annalen der physik* 4.

Emsell, Louise, Wim Van Hecke, and Jacques-Donald Tournier (2016). "Introduction to diffusion tensor imaging". In: *Diffusion Tensor Imaging*. Springer, pp. 7–19.

Esposito, Roberto, Peter A Mattei, Chiara Briganti, et al. (2012). "Modifications of default-mode network connectivity in patients with cerebral glioma". In: *PLoS One* 7.7, e40231.

Ferlay, Jacques, Isabelle Soerjomataram, Rajesh Dikshit, et al. (2015). "Cancer incidence and mortality worldwide: sources, methods and major patterns in GLOBOCAN 2012". In: *International journal of cancer* 136.5, E359–E386.

Fick, Adolf (1855). "Ueber diffusion". In: *Annalen der Physik* 170.1, pp. 59–86.

Fieremans, E, A Benitez, JH Jensen, et al. (2013). "Novel white matter tract integrity metrics sensitive to Alzheimer disease progression". In: *American Journal of Neuroradiology* 34.11, pp. 2105–2112.

Fornito, Alex, Andrew Zalesky, and Michael Breakspear (2015). "The connectomics of brain disorders". In: *Nature Reviews Neuroscience* 16.3, pp. 159–172.

Foulon, Chris, Leonardo Cerliani, Serge Kinkingnehun, et al. (2018). "Advanced lesion symptom mapping analyses and implementation as BCBtoolkit". In: *Gigascience* 7.3, giy004.

Fox, Michelle E and Tricia Z King (2018). "Functional connectivity in adult brain tumor patients: a systematic review". In: *Brain connectivity* 8.7, pp. 381–397.

Frank, Paul M and M Eslami (1980). "Introduction to system sensitivity theory". In: *IEEE Transactions on Systems, Man, and Cybernetics* 10.6, pp. 337–338.

Ghumman, Sukhmanjit, D Fortin, M Noel-Lamy, et al. (2016). "Exploratory study of the effect of brain tumors on the default mode network". In: *Journal of Neuro-oncology* 128.3, pp. 437–444.

Gillespie, Shawn and Michelle Monje (2018). "An active role for neurons in glioma progression: making sense of Scherer's structures". In: *Neuro-oncology* 20.10, pp. 1292–1299.

Griffis, Joseph C, Nicholas V Metcalf, Maurizio Corbetta, et al. (2019). "Structural disconnections explain brain network dysfunction after stroke". In: *Cell reports* 28.10, pp. 2527–2540.

Grisot, Giorgia, Suzanne N Haber, and Anastasia Yendiki (2021). "Diffusion MRI and anatomic tracing in the same brain reveal common failure modes of tractography". In: *NeuroImage*, p. 118300.

Gudbjartsson, Hákon and Samuel Patz (1995). "The Rician distribution of noisy MRI data". In: *Magnetic resonance in medicine* 34.6, pp. 910–914.

Hacker, Carl D, Jarod L Roland, Albert H Kim, et al. (2019). "Resting-state network mapping in neurosurgical practice: a review". In: *Neurosurgical focus* 47.6, E15.

Hahn, Erwin L (1950). "Spin echoes". In: *Physical review* 80.4, p. 580.

Hammers, Alexander, Richard Allom, Matthias J Koepp, et al. (2003). "Three-dimensional maximum probability atlas of the human brain, with particular reference to the temporal lobe". In: *Human brain mapping* 19.4, pp. 224–247.

Harris, Robert J, Susan Y Bookheimer, Timothy F Cloughesy, et al. (2014). "Altered functional connectivity of the default mode network in diffuse gliomas measured with pseudo-resting state fMRI". In: *Journal of neuro-oncology* 116.2, pp. 373–379.

Izquierdo-Garcia, David, Adam E Hansen, Stefan Förster, et al. (2014). "An SPM8-based approach for attenuation correction combining segmentation and nonrigid template formation: application to simultaneous PET/MR brain imaging". In: *Journal of Nuclear Medicine* 55.11, pp. 1825–1830.

Jbabdi, Saad and Heidi Johansen-Berg (2011). "Tractography: where do we go from here?" In: *Brain connectivity* 1.3, pp. 169–183.

Jelescu, Ileana O and Matthew D Budde (2017). "Design and validation of diffusion MRI models of white matter". In: *Frontiers in physics* 5, p. 61.

Jelescu, Ileana O, Jelle Veraart, Els Fieremans, et al. (2016). "Degeneracy in model parameter estimation for multi-compartmental diffusion in neuronal tissue". In: *NMR in Biomedicine* 29.1, pp. 33–47.

Jensen, Jens H, Joseph A Helpern, Anita Ramani, et al. (2005). "Diffusional kurtosis imaging: the quantification of non-gaussian water diffusion by means of magnetic resonance imaging". In: *Magnetic Resonance in Medicine: An Official Journal of the International Society for Magnetic Resonance in Medicine* 53.6, pp. 1432–1440.

Jeurissen, Ben, Maxime Descoteaux, Susumu Mori, et al. (2019). "Diffusion MRI fiber tractography of the brain". In: *NMR in Biomedicine* 32.4, e3785.

Jeurissen, Ben, Alexander Leemans, Derek K Jones, et al. (2011). "Probabilistic fiber tracking using the residual bootstrap with constrained spherical deconvolution". In: *Human brain mapping* 32.3, pp. 461–479.

Jeurissen, Ben, Jacques-Donald Tournier, Thijs Dhollander, et al. (2014). "Multi-tissue constrained spherical deconvolution for improved analysis of multi-shell diffusion MRI data". In: *NeuroImage* 103, pp. 411–426.

Jütten, Kerstin, Verena Mainz, Daniel Delev, et al. (2020). "Asymmetric tumor-related alterations of network-specific intrinsic functional connectivity in glioma patients". In: *Human Brain Mapping* 41.16, pp. 4549–4561.

Kaden, Enrico, Nathaniel D Kelm, Robert P Carson, et al. (2016). "Multi-compartment microscopic diffusion imaging". In: *NeuroImage* 139, pp. 346–359.

Kaden, Enrico, Frithjof Kruggel, and Daniel C Alexander (2016). "Quantitative mapping of the per-axon diffusion coefficients in brain white matter". In: *Magnetic resonance in medicine* 75.4, pp. 1752–1763.

Kadota, Yoshihito, Toshinori Hirai, Minako Azuma, et al. (2020). "Differentiation between glioblastoma and solitary brain metastasis using neurite orientation dispersion and density imaging". In: *Journal of Neuroradiology* 47.3, pp. 197–202.

Kim, Dongwoo, Soyoung Kim, Se Hoon Kim, et al. (2018). "Prediction of overall survival based on Isocitrate dehydrogenase 1 mutation and 18F-FDG uptake on PET/CT in patients with cerebral gliomas". In: *Clinical nuclear medicine* 43.5, pp. 311–316.

Knösche, Thomas R, Alfred Anwander, Matthew Liptrot, et al. (2015). "Validation of tractography: comparison with manganese tracing". In: *Human brain mapping* 36.10, pp. 4116–4134.

Kroenke, Christopher D, Joseph JH Ackerman, and Dmitriy A Yablonskiy (2004). "On the nature of the NAA diffusion attenuated MR signal in the central nervous system". In: *Magnetic Resonance in Medicine: An Official Journal of the International Society for Magnetic Resonance in Medicine* 52.5, pp. 1052–1059.

Krzanowski, WJ (1993). "Permutational tests for correlation matrices". In: *Statistics and Computing* 3.1, pp. 37–44.

Ladefoged, Claes N, Ian Law, Udunna Anazodo, et al. (2017). "A multi-centre evaluation of eleven clinically feasible brain PET/MRI attenuation correction techniques using a large cohort of patients". In: *Neuroimage* 147, pp. 346–359.

Lahrmann, Heinz, Barbara Horvath-Mechtler, Peter Hitzenberger, et al. (2005). "Pyramidal tract degeneration in astrocytoma". In: *Journal of neuro-oncology* 72.3, p. 271.

Le Bihan, Denis and E Breton (1985). "Imagerie de diffusion in vivo par résonance magnétique nucléaire". In: *Comptes rendus de l'Académie des sciences. Série 2, Mécanique, Physique, Chimie, Sciences de l'univers, Sciences de la Terre* 301.15, pp. 1109–1112.

Le Bihan, Denis, Eric Breton, Denis Lallemand, et al. (1986). "MR imaging of intravoxel incoherent motions: application to diffusion and perfusion in neurologic disorders." In: *Radiology* 161.2, pp. 401–407.

Li, Chao, Shuo Wang, Jiun-Lin Yan, Rory J Piper, et al. (2019). "Intratumoral heterogeneity of glioblastoma infiltration revealed by joint histogram analysis of diffusion tensor imaging". In: *Neurosurgery* 85.4, pp. 524–534.

Li, Chao, Shuo Wang, Jiun-Lin Yan, Turid Torheim, et al. (2019). "Characterizing tumor invasiveness of glioblastoma using multiparametric magnetic resonance imaging". In: *Journal of neurosurgery* 132.5, pp. 1465–1472.

Li, Shi-Hui, Ri-Feng Jiang, Ju Zhang, et al. (2019). "Application of neurite orientation dispersion and density imaging in assessing glioma grades and cellular proliferation". In: *World neurosurgery* 131, e247–e254.

Liu, Feng-Min, Yu-fei Gao, Yanyan Kong, et al. (2021). "The diagnostic value of lower glucose consumption for IDH1 mutated gliomas on FDG-PET". In: *BMC cancer* 21.1, pp. 1–9.

Liu, Luyan, Han Zhang, Islem Rekik, et al. (2016). "Outcome prediction for patient with high-grade gliomas from brain functional and structural networks". In: *International Conference on Medical Image Computing and Computer-Assisted Intervention*. Springer, pp. 26–34.

Liu, Yong, Kun Yang, Xinhua Hu, et al. (2020). "Altered rich-club organization and regional topology are associated with cognitive decline in patients with frontal and temporal gliomas". In: *Frontiers in human neuroscience* 14, p. 23.

Louis, David N, Arie Perry, Guido Reifenberger, et al. (2016). "The 2016 World Health Organization classification of tumors of the central nervous system: a summary". In: *Acta neuropathologica* 131.6, pp. 803–820.

Louis, David N, Arie Perry, Pieter Wesseling, et al. (2021). "The 2021 WHO classification of tumors of the central nervous system: a summary". In: *Neuro-oncology* 23.8, pp. 1231–1251.

Maekawa, Tomoko, Masaaki Hori, Katsutoshi Murata, et al. (2020). "Differentiation of high-grade and low-grade intra-axial brain tumors by time-dependent diffusion MRI". In: *Magnetic Resonance Imaging* 72, pp. 34–41.

Maier-Hein, Klaus H, Peter F Neher, Jean-Christophe Houde, et al. (2017). "The challenge of mapping the human connectome based on diffusion tractography". In: *Nature communications* 8.1, pp. 1–13.

Malcolm, James G, Martha E Shenton, and Yogesh Rathi (2010). "Filtered multi-tensor tractography". In: *IEEE transactions on medical imaging* 29.9, pp. 1664–1675.

Masjoodi, S, H Hashemi, MA Oghabian, et al. (2018). "Differentiation of edematous, tumoral and normal areas of brain using diffusion tensor and neurite orientation dispersion and density imaging". In: *Journal of biomedical physics & engineering* 8.3, p. 251.

Maximov, Ivan I, Aram S Tonoyan, and Igor N Pronin (2017). "Differentiation of glioma malignancy grade using diffusion MRI". In: *Physica Medica* 40, pp. 24–32.

Miller, Kimberly D, Quinn T Ostrom, Carol Kruchko, et al. (2021). "Brain and other central nervous system tumor statistics, 2021". In: *CA: a cancer journal for clinicians* 71.5, pp. 381–406.

Mori, Susumu, Barbara J Crain, Vadappuram P Chacko, et al. (1999). "Three-dimensional tracking of axonal projections in the brain by magnetic resonance imaging". In: *Annals of Neurology: Official Journal of the American Neurological Association and the Child Neurology Society* 45.2, pp. 265–269.

Mori, Susumu and J-Donald Tournier (2013). *Introduction to diffusion tensor imaging: And higher order models*. Academic Press.

Nenning, Karl-Heinz, Julia Furtner, Barbara Kiesel, et al. (2020). "Distributed changes of the functional connectome in patients with glioblastoma". In: *Scientific reports* 10.1, pp. 1–11.

Nilsson, Markus, Elisabet Englund, Filip Szczepankiewicz, et al. (2018). "Imaging brain tumour microstructure". In: *Neuroimage* 182, pp. 232–250.

Novikov, Dmitry S, Els Fieremans, Sune N Jespersen, et al. (2019). "Quantifying brain microstructure with diffusion MRI: Theory and parameter estimation". In: *NMR in Biomedicine* 32.4, e3998.

Novikov, Dmitry S, Valerij G Kiselev, and Sune N Jespersen (2018). "On modeling". In: *Magnetic resonance in medicine* 79.6, pp. 3172–3193.

O'Donnell, Lauren J and Carl-Fredrik Westin (2007). "Automatic tractography segmentation using a high-dimensional white matter atlas". In: *IEEE transactions on medical imaging* 26.11, pp. 1562–1575.

O'Donnell, Lauren J, Yannick Suter, Laura Rigolo, et al. (2017). "Automated white matter fiber tract identification in patients with brain tumors". In: *NeuroImage: Clinical* 13, pp. 138–153.

Oldham, Stuart and Alex Fornito (2019). "The development of brain network hubs". In: *Developmental cognitive neuroscience* 36, p. 100607.

Ostrom, Quinn T, Luc Bauchet, Faith G Davis, et al. (2014). "The epidemiology of glioma in adults: a "state of the science" review". In: *Neuro-oncology* 16.7, pp. 896–913.

Padma, MV, S Said, M Jacobs, et al. (2003). "Prediction of pathology and survival by FDG PET in gliomas". In: *Journal of neuro-oncology* 64.3, pp. 227–237.

Panagiotaki, Eleftheria, Rachel W Chan, Nikolaos Dikaios, et al. (2015). "Microstructural characterization of normal and malignant human prostate tissue with vascular, extracellular, and restricted diffusion for cytometry in tumours magnetic resonance imaging". In: *Investigative radiology* 50.4, pp. 218–227.

Panagiotaki, Eletheria, Simon Walker-Samuel, Bernard Siow, et al. (2014). "Noninvasive quantification of solid tumor microstructure using VERDICT MRI". In: *Cancer research* 74.7, pp. 1902–1912.

Pierpaoli, Carlo, Alan Barnett, Sinisa Pajevic, et al. (2001). "Water diffusion changes in Wallerian degeneration and their dependence on white matter architecture". In: *Neuroimage* 13.6, pp. 1174–1185.

Qin, Xingping, Rui Liu, Farhana Akter, et al. (2021). "Peri-tumoral brain edema associated with glioblastoma correlates with tumor recurrence". In: *Journal of Cancer* 12.7, p. 2073.

Ravi, Daniele, Nooshin Ghavami, Daniel C Alexander, et al. (2019). "Current applications and future promises of machine learning in diffusion mri". In: *International Conference on Medical Image Computing and Computer-Assisted Intervention*. Springer, pp. 105–121.

Roberts, Thomas A, Harpreet Hyare, Giulia Agliardi, et al. (2020). "Noninvasive diffusion magnetic resonance imaging of brain tumour cell size for the early detection of therapeutic response". In: *Scientific reports* 10.1, pp. 1–13.

Roberts, Tom, Harpreet Hyare, Ben Hipwell, et al. (2018). "Quantification of tumour microstructure in low and high-grade brain tumours using VERDICT MRI: an initial feasibility study". In: *Neuro-oncology* 20.suppl_1, pp. i16–i16.

Rolls, Edmund T, Chu-Chung Huang, Ching-Po Lin, et al. (2020). "Automated anatomical labelling atlas 3". In: *Neuroimage* 206, p. 116189.

Saksena, Sona, Rajan Jain, Lonni Schultz, et al. (2013). "The corpus callosum Wallerian degeneration in the unilateral brain tumors: evaluation with diffusion tensor imaging (DTI)". In: *Journal of clinical and diagnostic research: JCDR* 7.2, p. 320.

Salvalaggio, Alessandro, Michele De Filippo De Grazia, Marco Zorzi, et al. (2020). "Post-stroke deficit prediction from lesion and indirect structural and functional disconnection". In: *Brain* 143.7, pp. 2173–2188.

Savadjiev, Peter, Jennifer SW Campbell, Maxime Descoteaux, et al. (2008). "Labeling of ambiguous subvoxel fibre bundle configurations in high angular resolution diffusion MRI". In: *NeuroImage* 41.1, pp. 58–68.

Sawlani, Vijay, Rakesh K Gupta, Manoj K Singh, et al. (1997). "MRI demonstration of Wallerian degeneration in various intracranial lesions and its clinical implications". In: *Journal of the neurological sciences* 146.2, pp. 103–108.

Schaefer, Alexander, Ru Kong, Evan M Gordon, et al. (2018). "Local-global parcellation of the human cerebral cortex from intrinsic functional connectivity MRI". In: *Cerebral cortex* 28.9, pp. 3095–3114.

Schmitt, Franz, Michael K Stehling, and Robert Turner (2012). *Echo-planar imaging: theory, technique and application.* Springer Science & Business Media.

Schotten, Michel Thiebaut de, Chris Foulon, and Parashkev Nachev (2020). "Brain disconnections link structural connectivity with function and behaviour". In: *Nature communications* 11.1, pp. 1–8.

Smith, Robert E, Jacques-Donald Tournier, Fernando Calamante, et al. (2012). "Anatomically-constrained tractography: improved diffusion MRI streamlines tractography through effective use of anatomical information". In: *Neuroimage* 62.3, pp. 1924–1938.

— (2013). "SIFT: Spherical-deconvolution informed filtering of tractograms". In: *Neuroimage* 67, pp. 298–312.

— (2015). "SIFT2: Enabling dense quantitative assessment of brain white matter connectivity using streamlines tractography". In: *Neuroimage* 119, pp. 338–351.

Sporns, Olaf (2011). "The human connectome: a complex network". In: *Annals of the new York Academy of Sciences* 1224.1, pp. 109–125.

Stanisz, Greg J, Graham A Wright, R Mark Henkelman, et al. (1997). "An analytical model of restricted diffusion in bovine optic nerve". In: *Magnetic Resonance in Medicine* 37.1, pp. 103–111.

Stejskal, Edward O and John E Tanner (1965). "Spin diffusion measurements: spin echoes in the presence of a time-dependent field gradient". In: *The journal of chemical physics* 42.1, pp. 288–292.

Steven, Andrew J, Jiachen Zhuo, and Elias R Melhem (2014). "Diffusion kurtosis imaging: an emerging technique for evaluating the microstructural environment of the brain". In: *American journal of roentgenology* 202.1, W26–W33.

Szczepankiewicz, Filip, Samo Lasič, Danielle van Westen, et al. (2015). "Quantification of microscopic diffusion anisotropy disentangles effects of orientation dispersion from microstructure: applications in healthy volunteers and in brain tumors". In: *Neuroimage* 104, pp. 241–252.

Szczepankiewicz, Filip, Jens Sjölund, Freddy Ståhlberg, et al. (2019). "Tensor-valued diffusion encoding for diffusional variance decomposition (DIVIDE): Technical feasibility in clinical MRI systems". In: *PLoS One* 14.3, e0214238.

Tariq, Maira, Torben Schneider, Daniel C Alexander, et al. (2016). "Bingham–NODDI: Mapping anisotropic orientation dispersion of neurites using diffusion MRI". In: *Neuroimage* 133, pp. 207–223.

Thiebaut de Schotten, Michel, Flavio Dell'Acqua, P Ratiu, et al. (2015). "From Phineas Gage and Monsieur Leborgne to HM: revisiting disconnection syndromes". In: *Cerebral Cortex* 25.12, pp. 4812–4827.

Thiebaut de Schotten, Michel, Marika Urbanski, Benedicte Batrancourt, et al. (2017). "Rostro-caudal architecture of the frontal lobes in humans". In: *Cerebral Cortex* 27.8, pp. 4033–4047.

Thomaseth, Karl and Claudio Cobelli (1999). "Generalized sensitivity functions in physiological system identification". In: *Annals of biomedical engineering* 27.5, pp. 607–616.

Timmeren, Janita E van, Davide Cester, Stephanie Tanadini-Lang, et al. (2020). "Radiomics in medical imaging—"How-to" guide and critical reflection". In: *Insights into Imaging* 11.1, pp. 1–16.

Torrey, Henry C (1956). "Bloch equations with diffusion terms". In: *Physical review* 104.3, p. 563.

Tournier, J Donald, Fernando Calamante, Alan Connelly, et al. (2010). "Improved probabilistic streamlines tractography by 2nd order integration over fibre orientation distributions". In: *Proceedings of the international society for magnetic resonance in medicine*. Vol. 1670. John Wiley & Sons, Inc. New Jersey, USA.

Tournier, J-Donald, Fernando Calamante, and Alan Connelly (2007). "Robust determination of the fibre orientation distribution in diffusion MRI: non-

negativity constrained super-resolved spherical deconvolution". In: *Neuroimage* 35.4, pp. 1459–1472.

Tournier, J-Donald, Fernando Calamante, and Alan Connelly (2012). "MRtrix: diffusion tractography in crossing fiber regions". In: *International journal of imaging systems and technology* 22.1, pp. 53–66.

Tournier, J-Donald, Fernando Calamante, David G Gadian, et al. (2004). "Direct estimation of the fiber orientation density function from diffusion-weighted MRI data using spherical deconvolution". In: *Neuroimage* 23.3, pp. 1176–1185.

Tournier, J-Donald, Robert Smith, David Raffelt, et al. (2019). "MRtrix3: A fast, flexible and open software framework for medical image processing and visualisation". In: *Neuroimage* 202, p. 116137.

Tournier, Jacques-Donald, Susumu Mori, and Alexander Leemans (2011). "Diffusion tensor imaging and beyond". In: *Magnetic resonance in medicine* 65.6, p. 1532.

Turner, Robert, Denis Le Bihan, and A Scott Chesnicks (1991). "Echo-planar imaging of diffusion and perfusion". In: *Magnetic resonance in medicine* 19.2, pp. 247–253.

Tustison, Nicholas J, Brian B Avants, Philip A Cook, et al. (2010). "N4ITK: improved N3 bias correction". In: *IEEE transactions on medical imaging* 29.6, pp. 1310–1320.

Van Everdingen, KJ, J Van der Grond, LJ Kappelle, et al. (1998). "Diffusion-weighted magnetic resonance imaging in acute stroke". In: *Stroke* 29.9, pp. 1783–1790.

Veraart, Jelle, Dmitry S Novikov, Daan Christiaens, et al. (2016). "Denoising of diffusion MRI using random matrix theory". In: *Neuroimage* 142, pp. 394–406.

Veraart, Jelle, Jan Sijbers, Stefan Sunaert, et al. (2013). "Weighted linear least squares estimation of diffusion MRI parameters: strengths, limitations, and pitfalls". In: *Neuroimage* 81, pp. 335–346.

Wang, Xiangdong, Chunyao Zhou, Lei Wang, et al. (2020). "Motor cortex gliomas induces microstructural changes of large fiber tracts revealed by TBSS". In: *Scientific Reports* 10.1, pp. 1–8.

Wen, Qiuting, Douglas AC Kelley, Suchandrima Banerjee, et al. (2015). "Clinically feasible NODDI characterization of glioma using multiband EPI at 7 T". In: *NeuroImage: Clinical* 9, pp. 291–299.

Wiestler, Benedikt, Anne Kluge, Mathias Lukas, et al. (2016). "Multiparametric MRI-based differentiation of WHO grade II/III glioma and WHO grade IV glioblastoma". In: *Scientific reports* 6.1, pp. 1–6.

Wu, Chen-Xing, Guo-Shi Lin, Zhi-Xiong Lin, et al. (2015). "Peritumoral edema on magnetic resonance imaging predicts a poor clinical outcome in malignant glioma". In: *Oncology letters* 10.5, pp. 2769–2776.

Yeh, Chun-Hung, Derek K Jones, Xiaoyun Liang, et al. (2021). "Mapping structural connectivity using diffusion MRI: Challenges and opportunities". In: *Journal of Magnetic Resonance Imaging* 53.6, pp. 1666–1682.

Yeh, Fang-Cheng, Andrei Irimia, Dhiego Chaves de Almeida Bastos, et al. (2021). "Tractography methods and findings in brain tumors and traumatic brain injury". In: *NeuroImage* 245, p. 118651.

Yuan, Taoyang, Zhentao Zuo, Jianyou Ying, et al. (2020). "Structural and functional alterations in the contralesional medial temporal lobe in glioma patients". In: *Frontiers in neuroscience* 14, p. 10.

Zaccagna, Fulvio, Frank Riemer, Andrew N Priest, et al. (2019). "Non-invasive assessment of glioma microstructure using VERDICT MRI: correlation with histology". In: *European radiology* 29.10, pp. 5559–5566.

Zhang, Fan, Peter Savadjiev, Weidong Cai, et al. (2018). "Whole brain white matter connectivity analysis using machine learning: an application to autism". In: *NeuroImage* 172, pp. 826–837.

Zhang, Fan, Ye Wu, Isaiah Norton, et al. (2018). "An anatomically curated fiber clustering white matter atlas for consistent white matter tract parcellation across the lifespan". In: *NeuroImage* 179, pp. 429–447.

Zhang, Hui, Torben Schneider, Claudia A Wheeler-Kingshott, et al. (2012). "NODDI: practical in vivo neurite orientation dispersion and density imaging of the human brain". In: *Neuroimage* 61.4, pp. 1000–1016.